Amplification of high-fidelity laser pulses

Habilitationsschrift

vorgelegt von Dr. Vincent Bagnoud

Tag der Einreichung: 24. März 2016

TECHNISCHE
UNIVERSITÄT
DARMSTADT

Fachbereich Physik

Gutachter:

1. Prof. Dr. **Markus Roth**, Technische Universitt Darmstadt, Darmstadt
2. Prof. Dr. **Matt Zepf**, Helmholtz-Institut Jena, Jena
3. Prof. **Jean Claude Kieffer**, Institut National de la Recherche Scientifique, Varennes (Kanada)

Contents

Chapter 1

Introduction and state of the art

1.1 Scope and contents

This manuscript summarizes my contribution to the field of high-energy high-intensity laser physics that I have started studying in 1996 first in France at LOA in Palaiseau, at CELIA and later at CESTA in Bordeaux. I have then continued working on laser physics as a scientist at the university of Rochester, USA in the framework of the OMEGA-EP project [1] before moving to GSI in Darmstadt Germany, where I have been working for the past ten years on the development, operation and improvement of the PHELIX machine [2]. Along these years, it became more and more evident to me that a better understanding of the requirements of experiments and their underlying physics background is the key to generating the most appropriate machines, capable of fulfilling the goals of modern physics studies with lasers. The most important parameter that drives this field of physics research is the on-target laser intensity, defined as the ratio of the laser pulse energy to the product of pulse duration and beam surface area. It is also the parameter that illustrates at best all the qualities of lasers, being able to generate simultaneously high-energy pulses, small diffraction-limited spots and pulses of femtosecond pulse duration.

In the first part of the manuscript, a heuristic review of the field is presented, starting from a selection of significant applications and results to the description of current existing facilities. This is followed by the introduction to high-fidelity laser amplification, which is a central issue at modern high-intensity laser facilities and the topic of the two following chapters. In a second part, I report on the work that I have done on the temporal contrast of laser pulses, reviewing the underlying requirements for high temporal contrast, the sources of temporal contrast degradation and the solution that I and others have developed. Here, my main contribution has been the implementation of the fast OPA scheme proposed by a former colleague of the university of Rochester at the PHELIX laser. This work was the enabling technological improvement that opened a wide range of study possibilities on thin targets at PHELIX. Beyond the results obtained by the fast OPA, I formulate a proposal for a new type of pulse stretcher that should also help steepen the pulse front of the laser pulse in CPA lasers systems. At the end of this part, I have added a selection of personal publications that I consider of particular relevance to the temporal contrast issue. The last part of the manuscript summarizes the work I have done on beam quality improvement, beam control and thermal load handling in laser amplifiers. This aspect has been a guiding thread in my work and keeps coming back as the requirements on lasers are always pushed further and more control tools are being developed. An essential result is the development of millijoule-level titanium-doped

sapphire amplifiers under high thermal load and the development work I did on OPCPA as a high-average output power amplifier in Rochester, as shown in the articles that I have added to that chapter.

1.2 Terawatt to petawatt laser facilities in the world

The introduction of the chirped pulse amplification (CPA) technique [3] in the mid 80's has enabled a widespread development of high-intensity lasers in laboratories around the world. Until then, high-intensity lasers were large machines that were the prerogative of large national laboratories. But CPA made it possible to generate high-peak-power pulses on a moderate footprint along the line of the acronym "T^3" or "*T cube*" standing for table-top terawatt laser. This technique, together with the discovery of the potential of titanium-doped sapphire [4] to support the generation and amplification of ultrashort femtosecond pulses of a few tens of femtoseconds, helped to reduce the physical size, the complexity and costs of terawatt lasers dramatically.

This development turned out to be a paradigm change also because the terawatt power level represents a threshold that enables reaching relativistic laser-matter interaction conditions. This type of interaction is usually described by the normalized vector potential a_0, defined as the ratio of the classical speed of an electron oscillating in an electric field of amplitude E_0 and angular frequency ω to the speed of light c:

$$a_0 = \frac{eE_o}{m_e \omega c} \tag{1.1}$$

where e and m_e are the charge and mass of the electron respectively. Experimentally, this parameter is maximized at the focus of any driving laser beam and it can be advantageous to express it as a function of experimental quantities like the laser peak-power P and F#, the F-number of the focusing system. In the case of a Gaussian beam, eq. 1.1 yields:

$$a_0 = \frac{1}{F\#}\frac{e}{m_e c}\sqrt{\frac{P}{4\epsilon_0 c^3 \pi}} \tag{1.2a}$$

$$= \frac{1}{F\#}\sqrt{\frac{P}{0.88 \times 10^{10}}} \tag{1.2b}$$

where ε_0 is the vacuum permittivity and P is given in watts. For a "top hat" beam, a factor of $\sqrt{2}$ has to be applied to the equation above and the factor 0.88 gives 1.75. This equation indicates that a_0 only depends of the laser power and the strength of the focusing, independently of the central wavelength of the laser. Note that theory papers tend to emphasize the wavelength dependency of the vector potential on $(I\lambda^2)$, deducing then that long wavelength infrared lasers are of particular interest for relativistic studies. But this neglects diffraction effects, which in turn cancels the wavelength dependence when the laser is used at the focus. For a terawatt laser with a moderately strong focusing system (F# = 10), the motion of the electron becomes relativistic, i. e. $a_0 > 1$, opening the way to a completely different interaction regime. In terms of laser on-focus intensity, this is reached for intensities of about $10^{18}\,\mathrm{W/cm^2}$ at a wavelength of 1 µm.

Terawatt and petawatt lasers usually exploit the CPA technique, in which the pulse is first temporally stretched before amplification such as to decrease its peak power by up to 3 orders of

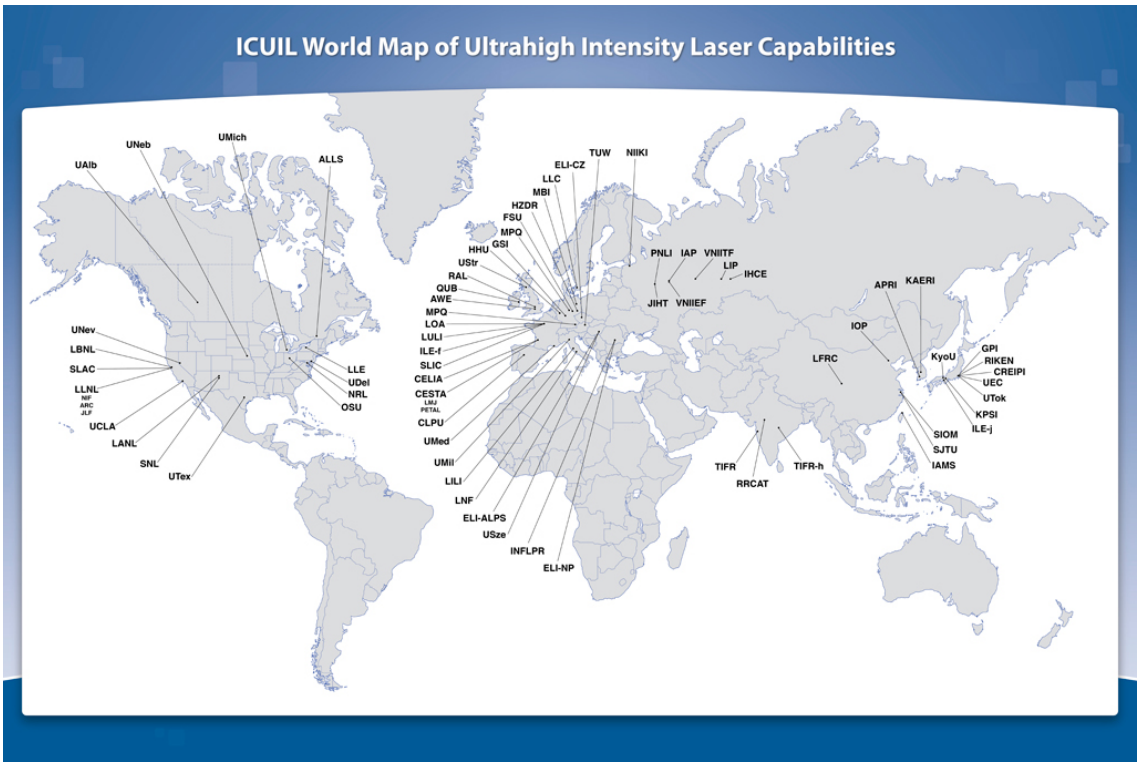

Figure 1.1: World map of the high-intensity laser facilities (according to Prof. C. P. J. Barty (2011)[2])

magnitude. This step strongly reduces the amount of detrimental nonlinear intensity-driven effects, and finally the pulses are compressed back to their initial duration at the end of the laser amplifier in a pulse compressor. After the first ground ideas on CPA were published at the end of the 80's, the peak power reached by CPA lasers boomed with the first compact terawatt systems reaching 10 TW around 1990 [5], followed by 100 TW systems in 1998 [6] and the first petawatt laser [7] in 1999. The latter laser system exploited the existing Nova amplifier at LLNL in California to build the most powerful laser of that time. For systems based on titanium-doped sapphire, the first petawatt laser came a few years after that in 2003 [8], giving the starting point to the series of petawatt-class laser realizations that has been seen in the first decade of the century.

Nowadays, because terawatt lasers are so interesting for basic science, there are more than 100 laboratories in the world exploiting the capabilities of multi-terawatt lasers. A map of the ultra-high intensity laser capabilities in the world, depicted in fig. 1.1, shows that such lasers are mostly present in North America, Europe and the Far East. Here it should be noted that the southern hemisphere does not host any high-intensity laser yet. Among the high-intensity lasers, 19 claim to have petawatt-class capability in 2015 [9], but with none exceeding 2 PW, showing that CPA is now a mature technology that reached a more or less steady state. Petawatt peak powers are either obtained with neodymium-doped glass or titanium-doped sapphire amplifiers, both approaches producing complementary systems: the former enable kilojoule level laser pulses in the sub-picosecond range (~ 500 J in ~ 500 fs), while the latter deliver tens of joules in few tens of femtoseconds (~ 30 J in ~ 30 fs).

[2]The latest map can be found at http://www.icuil.org

The rapid development of high-intensity lasers has been sustained by the discovery of various applications. Although quite compact, petawatt lasers still represent a significant investment for research institutions, and their construction is often directed at specific applications. Among the significant achievements of high-intensity lasers that motivate the construction of these facilities, the prospect to accelerate charged particles like electrons [10] and light ions is a very attractive one, as illustrated in fig. 1.2 a and b. The laser-driven acceleration of high-quality electron beams that has been experimentally demonstrated by several groups simultaneously [11–13] around the turn of the century is a major application of high-intensity lasers. Under optimal conditions of laser intensity, laser pulse duration and plasma density, the relativistic interaction of an ultra-intense laser beam with an underdense plasma generates a plasma bubbles in the wake of the laser [14]. These bubbles are electron voids surrounded by a thin layer of high electron density that forms their wall. The bubble shape is stable in the moving frame of the laser and persists over a long distance. Its origin lies in the transverse oscillating movement of the electrons shovelled away from the area of high laser intensity by the ponderomotive force and later attracted back to the laser axis by the electrostatic force. Inside the bubble, electric fields larger than 100 GV/m [15], about 3 orders of magnitude higher than in conventional accelerator structures, are able to accelerate electrons. Nowadays, many groups in the world are actively exploring the potential capabilities of such a laser-based accelerator with major contributions being made by the BELLA center in California [16, 17]. This group exploits in particular the first commercial petawatt laser [18] ever built. Several other groups are also reporting electron energies about or above 1 GeV from centimetre-scale laser-driven accelerator structures [19–21].

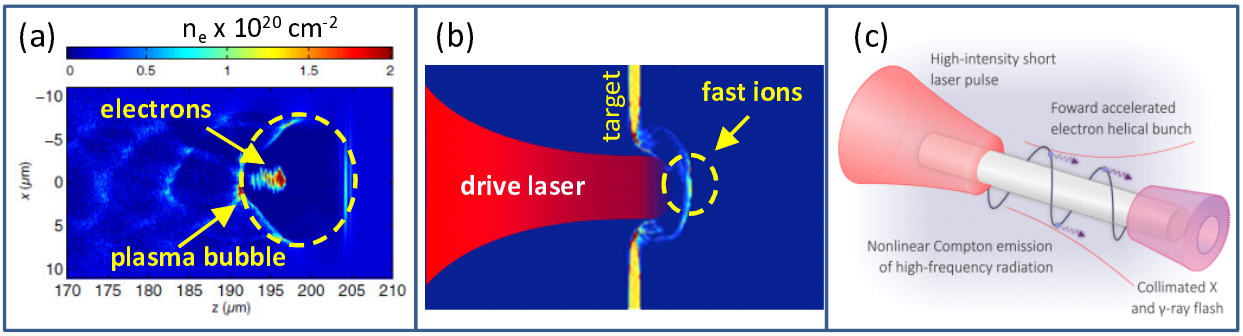

Figure 1.2: Three-dimensional particle-in-cell simulations illustrating significant applications of high-intensity lasers (adapted from the literature): (a) Electron density distribution (n_e) in laser-driven electron acceleration in the bubble regime [22], (b) Particle density in the light-sail interaction regime (simulation Dr. A. Robinson) some short instants after the laser irradiation, (c) Schematics for an optimized hard X-ray burst generation using nanowire targets and ultrahigh-intensity laser pulses [23].[4]

Another successful application of high-intensity lasers has been the generation of ion beams with kinetic energies in the 10 to 100 MeV range. The generation of thermal keV ions from laser-generated plasmas has been known since the first plasma physics experiments with lasers [24]. The breakthrough, however, was obtained at LLNL by Snavely et al. [25] with ion velocities much higher than what thermal expansion models predict for interaction conditions in reach of laser pulses at the petawatt level. Based on these first observations, a wide range of potential applications were rapidly proposed from oncology [26] to inertial confinement fusion research [27] and more basic plasma research [28] or more recently the generation of neutron beams [29]. There are now several

[4] Permission to re-use and adapt the shown figures has been granted by the respective authors

interaction mechanisms that are known to lead to laser-driven ion acceleration, all of them involving a stepwise interaction of the laser pulse with electrons, which in turn accelerate ions. A robust technique capable of transferring up to 15 % of the laser energy into ion kinetic energy [30] is called target normal sheath acceleration (TNSA) [31]. TNSA delivers high-energy high-quality ion beams with ultra-small emittance well below 0.01 mm×mrad [32, 33] and it is characterized by an exponentially decreasing kinetic energy spectrum. Such a particle beam is created when an intense laser pulse is focused onto thin targets with thickness in the 10-to-100 micrometre range in a stepwise charge separation, ionization and acceleration process (see fig. 1.3). However, unlike theoretical predictions, TNSA still fails to deliver proton energies above an actual cut-off energy limit of 60 to 85 MeV [34, 35], when reliable sources of protons up to 250 MeV would be necessary to sustain applications in life science [36].

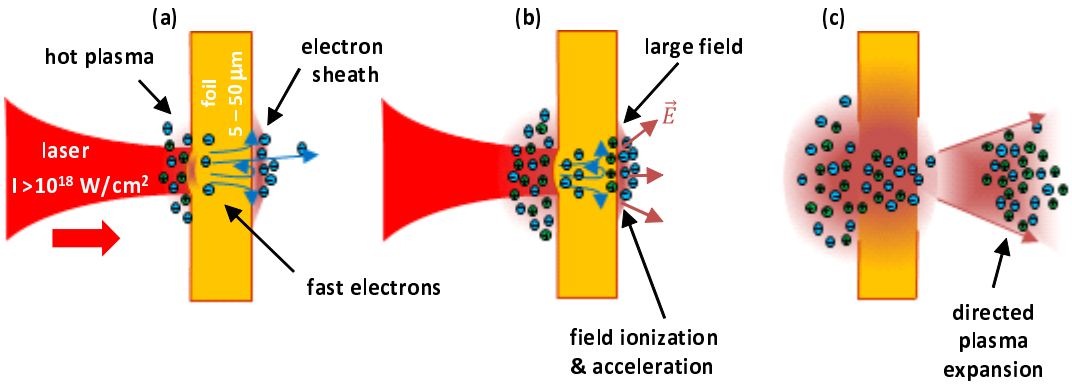

Figure 1.3: Schematics of the stepwise interaction leading to TNSA. (a) The laser deposits its energy at the surface of the foil and heats electrons that are expelled from this area. (b) The electrons accumulate at the rear of the foil. The resulting electrostatic potential is strong enough to field ionize light ions and they are accelerated by the electrostatic field. (c) The light ions exit the foil area at high velocities as a neutral beam draining with them cold electrons.

For ultra-thin nanometre-thick targets and particular laser pulse properties like ultra-high intensity and an abrupt onset of the laser intensity, the low mass target remains opaque until the peak of the pulse is reached, creating favourable conditions for radiation pressure acceleration (RPA) as theoretically described by Robinson et al. [37]. In the RPA scheme, electrons remain relatively cold until the maximum of the pulse intensity is reached and they are collectively ploughed forward, draining the bulk of the target with them thanks to the created electrostatic potential. Theoretical predictions show a more favourable picture, as far as the energy spectrum of RPA beams is concerned, because the kinetic energy of the particle scales with the laser intensity [38] rather than its square root and their energy spectrum should be peaked around a mean value. Fig. 1.2.b shows the numerically predicted spatial distribution of particles near the end of the interaction time in RPA-favourable conditions, exhibiting a directed beam of particles leaving the target with a narrow mean velocity. In numerical simulations, this mechanism yields high particle energies but the requirements on the laser are such that the energies observed in RPA experiments could not exceed those reported with TNSA yet. In addition, experiment results indicate that petawatt lasers are only able to create hybrid conditions between TNSA and RPA. A third mechanism is taking place when the laser intensity is such that the target becomes relativistically transparent [39] during the interaction. Relativistic transparency happens when the mass of the electrons is increased thanks to relativistic effects, which in turn increases the critical electron density of the plasma n_c.

When n_c increases such that $n_c > n_e$, the plasma becomes undercritical and transparent. During this transition phase, an additional momentum transfer happens to the accelerating particles. This mechanism called "break-out after burner" (BOA) which has been initially studied at LANL [40] requires somehow less stringent pulse quality conditions and could be easier to realize experimentally. Simulations show that BOA should be very efficient, being able to reach higher energies for a wide range of ions including heavy ions. But in all cases, the interaction processes driving ion-acceleration happen stepwise, so the required intensity is higher than for the direct acceleration of electrons; and therefore all successful experimental studies have been performed with petawatt-class lasers.

Another application of high-intensity lasers is the generation of X-rays. The production of X-ray sources is a century-old field but it is always an active one because of the many societal applications and the need for cheaper and more efficient sources. High-intensity lasers have been first applied to the generation of pulsed K-α sources [41]. The K-α emission is poorly coherent being in general fully isotropic but the sub-picosecond duration of the X-ray burst makes it very attractive for time resolved studies. Radiographic applications have motivated alone the construction of some of the largest short-pulse lasers worlwide [1]. More recently, the generation of X-rays from the collective motion of electrons has opened new possibilities (see the X-ray section in [42]). Here, electrons accelerated by ultra-intense lasers can acquire a transverse oscillation motion component that is stabilized by the bubble geometry. These oscillations are betatron oscillations; they happen at a small scale that favours the emission of X-ray synchrotron radiation in the plasma wake of the laser and therefore generate a directed X-ray beam [43], that comes for free with the laser-accelerated electrons. Another possible refinement is to send the laser-accelerated electrons to a wiggler and therefore generate coherent X-ray free-electron laser radiation. The requirement on the electron beam quality is, however, very high and the experimental demonstration of a laser-driven free-electron laser lies still a few years ahead of us. In such a case, the X-ray emission would be directed in the laser propagation direction, ultrashort and somehow tunable, greatly extending the radiographic possibilities first studied with k-α sources. At higher intensities, the radiation friction force cannot be neglected any more and electrons emit large quantities of X-rays from their motion alone. When considering the interaction of the laser with specifically-engineered solid targets like thin wires as depicted in fig 1.2.c, strongly directed gamma bursts can also be generated when circularly polarized light pulses of an intensity of about $10^{22}\,\mathrm{W/cm^2}$ are used. The conditions for the experimental study of these effects are about to be met with the next generation of laser facilities and should be rich of new applications in the upcoming years.

Looking into the future, there are nowadays several large-scale infrastructure projects aspiring to push the limit of high-intensity lasers at the 10 PW level and above. The distributed infrastructure ELI [44] is the most advanced one but one can also mention projects in the USA [45], Russia [46] or Japan [47] that aim at performances above the 10 PW level. When one considers the normalized motion amplitude (eq. 1.1) in the view of heavier particles, one realizes that the petawatt level is the level required to bring protons to relativistic speeds enabling new interaction processes to take place. In analogy to the laser-electron interaction requirements, one expects powers at the 10 PW level to have a high discovery potential. In addition, QED effects like vacuum non-linearity [48] will be in reach of these new experimental facilities. For real-world applications where power efficiency and average power are of particular importance, e. g. laser-based particle accelerators, complementary technologies based on laser-diode pumping and/or large fibre bundles [49] are being actively pursued, gathering all the know-how developed in photonics to deliver laser pulses of high quality in a wall-plug efficient and economically competitive way.

1.3 High-fidelity laser pulses and laser beams

The subject of this manuscript is the amplification of laser pulses to the terawatt and petawatt peak-power regimes. Short pulses are in general generated in mode-locked laser cavities [50] that exhibit near text-book quality in both spatial and temporal domains. In the spatial domain, high-purity spatial modes are obtained nearly for free out of standard laser cavities, e. g. TEM_{00}, while in the temporal domain, extremely well-behaved hyperbolic secant squared pulse profiles following the mathematical solution of soliton-like oscillations are nearly systematically obtained. The temporal features of laser pulses include also the possible control of the carrier-envelope phase for few-cycle femtosecond pulses [51] and a high temporal fidelity over many orders magnitude in intensity [52,53]. The energy of individual pulses generated by mode-locked oscillators is, however, extremely small, typically in the nanojoule range, and amplification with extremely high gains are necessary for applications in the relativistic intensity regime.

1.3.1 Energy and average power

The amplification of short laser pulses is the sine qua non condition to reach relativistic intensities. Gigantic amplification factors up to 10^{12} are usually applied to the oscillator output and this logically raises the question of the fidelity of the amplification as in any amplifier with such a high gain. In high-intensity lasers, the foremost parameters are pulse energy, pulse duration and beam quality that altogether define the intensity that can be reached. A fourth parameter whose importance has been growing within the last decade is the temporal contrast of short laser pulses or pulse fidelity on a high-dynamic range.

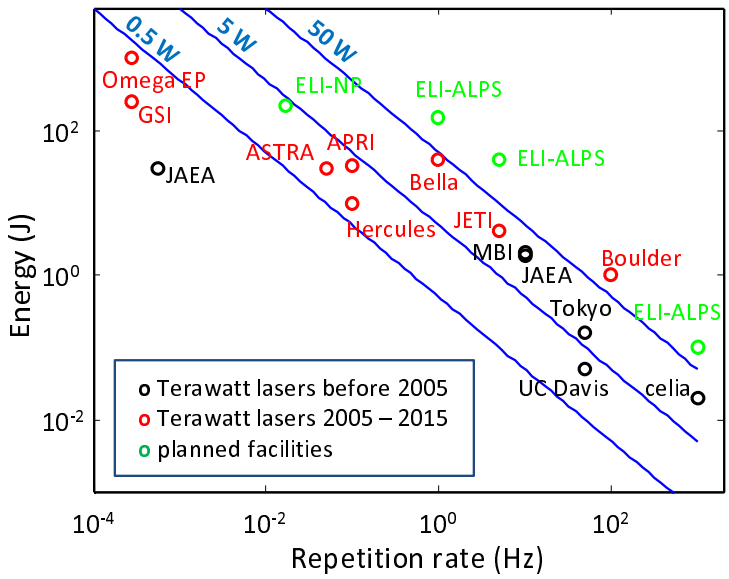

Figure 1.4: Laser energy as a function of the laser repetition rate: the blue lines represent the average power while the dots are selected terawatt systems that are representative of the field.

The energy of the laser pulse can only be appreciated in view of the repetition rate of the laser system. Fig. 1.4 illustrates this point by plotting the performance of a few representative lasers on a logarithmic scale. The blue lines indicate areas of equal average power showing that most

laser systems developed to date produce between 0.5 and 50 watts of average power. The systems have been differentiated based on their commissioning date. One can clearly see that the early systems favoured higher repetition rates, while the last decade has seen systems of higher peak powers and energies but in the hertz and sub-hertz regimes. All the above-mentioned systems exploit titanium-doped sapphire and deliver an average power around the few watts mark. The high-energy systems based on neodymium-doped glass deliver lower average powers because of the poor thermal properties of glass. The upcoming new facilities developed along the billion-Euro project ELI all announce performance at least one order of magnitude in energy and average power above what is the current state-of-the-art. For future developments, the following areas are being explored:

- A higher efficiency and higher average power could be obtained with Ytterbium-doped directly-diode-pumped lasers that perform better because of the low quantum defect of ytterbium and the thermal efficiency of laser diode pumping. The first important system was demonstrated at the Colorado State University in Boulder with an unprecedented average power of 100 W (1 J, 100 Hz) but long pulses of 5 ps [54]. Other systems exploiting ytterbium-doped calcium fluoride that can support sub-200-fs pulses are being developed in Germany at the Helmholtz Institute Jena and the Helmholtz Centre Dresden-Rossendorf for instance.

- A higher average power for existing systems can be reached with improved cooling techniques. This focuses on the heat removal from the laser slabs used for high-energy lasers above a few joules. This has been pioneered by LLNL with the Mercury project [55] for nanosecond lasers and it is being right now seriously considered by many laboratories worldwide. At the forefront, cryogenic cooling techniques are promising because all materials have much higher thermal conductivities and therefore exhibit lower thermal gradients at low temperature and secondly because cooling gases like helium can then be employed.

- An alternative amplification scheme based on optical parametric chirped pulse amplification (OPCPA) [56] has been successfully used with nanosecond and picosecond kilowatt pump fibre lasers [57]. Fibres are ideal amplifiers as far as their thermal behaviour. At first, cooling is efficient because of the surface to volume ratio, and secondly the fibre is very robust against thermal distortions. While the petawatt peak power is still out of reach of fibre lasers, the coherent addition of individual fibre amplifiers could be a solution. [49, 58]

1.3.2 Temporal aspects

With maximum energy and average power being at the centre of preoccupations in laser amplifier design, pushing those to the limit has strong effects on pulse duration and beam quality. Higher energies will lead to non-linear intensity-induced distortions. This includes the non-linear Kerr effect, quantified as B-integral in the time domain and beam distortions in the spatial domain. The average power will create mostly spatial quality distortions and energy loss via stress-induced depolarization losses. The interplay between energy and the high fidelity of the laser sets then the framework of high-intensity laser development.

The second important aspect of short-pulse lasers is related to the temporal fidelity of the pulse. For a long time, the focus has been on the pulse duration which can be seriously altered during amplification. A widely spread approach valid as long as the electric field is homogeneous across the beam, is to describe the pulse in the spectral domain using the amplitude E and phase φ of the

complex electric field $\tilde{E}$:

$$\tilde{E}(\omega) = E(\omega)e^{i\varphi(\omega)} \tag{1.3}$$

The spectral field amplitude defines the minimum pulse duration or Fourier-transform limit that the laser is able to sustain. Laser oscillators capable of producing pulses down to 5 fs have been known since the initial studies on oscillators based on titanium-doped sapphire [59,60] but amplified terawatt pulses below 20 fs are still uncommon. This increase in pulse duration comes from a reduction of the spectral amplitude width of the pulses along the amplification process.

gain	10^4	10^6	10^8	10^{10}	10^{12}
spectral width (nm)	51	45	41	38	35
pulse duration (fs)	16	19	21	23	26

Table 1.1: Calculated spectral widths and pulse durations in the full width half maximum sense for various gain factors for a 80-nm-wide pulse amplified in titanium-doped sapphire. The emission cross section curve uses a fit to the data from [4] and the gain is not saturated.

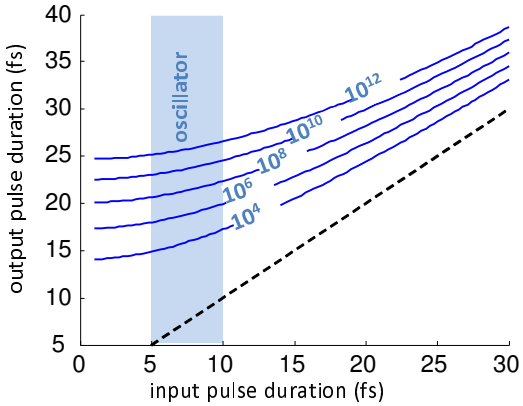

Figure 1.5: Gain narrowing in a titanium-doped sapphire amplifier. Output pulse duration as a function of the input pulse duration. For the pulse durations created by short pulse oscillators (in blue), the output pulse duration strongly depends on the gain of the amplifier.

The table 1.1 and figure 1.5 illustrate this point by plotting calculated gain-bandwidths as function of the gain factor for titanium-doped sapphire when saturation effects are neglected. The gain cross-section was simulated using the spectroscopic data of [4] and an input Gaussian pulse with spectral width equal to 80 nm was used for the table. In addition the figure indicates the typical pulse duration obtained from ultrashort titanium-doped sapphire oscillators (in blue). The calculations show that a reduction of the spectral width (gain-narrowing) must be expected in short pulse amplifiers. In addition, the theoretical minimum output pulse duration of these amplifiers depends more on the gain factor than on the input pulse duration. Apart from gain narrowing, saturation effects and the spectral bandwidth of the reflecting optics (polarizers and mirrors) can also play a role in spectral amplitude distortion.

There are several techniques that have been developed to counteract gain narrowing: some passive and others active. Passive methods based on spectral filtering are cost effective and easy to implement [61]. However, the number of degrees of freedom are limited while the gain narrowing effects may need dynamic correction. For instance, changes in relative humidity in the laser environment are able to change the spectral reflectivity of coatings, or some evolution of the gain and gain saturation along the amplifier imposed by drifts or modulation required by certain experiments can happen. Indeed, these are not easily addressed by passive methods and require more flexibility. The active methods involve the use of a programmable spectral filter together with a retro-action loop. The most interesting implementations include the use of spatial light modulators in the spectral

plane of the stretcher [62] or the use of an acousto-optic programmable filter [63] as being offered commercially since a few years now.

A workaround to gain narrowing is to use ultra broadband pre-amplification so that the total gain to be applied in the main amplifier is reduced to the minimum. A first attempt was made with the NOVA petawatt laser [7] where titanium-doped sapphire was used as a broadband pre-amplifier for the NOVA glass amplifier. More recently, better performing implementations have been done with optical parametric chirped pulse amplifiers (OPCPA) used as the front end of large glass [64, 65] and titanium-doped sapphire systems [66]. Parametric amplification is inherently broadband and scalable as long as a powerful enough pump laser is available for pumping. Here architectures solely based on OPCPA have been even reported for ultrashort petawatt pulse generation [67]. Another method based on non-linear spectral broadening was introduced with the concept of double CPA (see chapter 2 on temporal contrast) when a crossed-polarized wave setup [68] is being used. Here the primary effect that was sought after was a temporal cleaning of the pulse via non-linear polarization rotation. But as a side effect, the strong non-linear Kerr effect introduces a large self-phase modulation on the pulse. This yields a controlled spectral broadening that compensates for the gain narrowing that occurred in the first part of the system. As a result, broadband sub-15-fs pulses at the millijoule level can be generated, strongly reducing the required gain for the main amplifier and the gain narrowing accordingly.

The phase term in eq. 1.3, the so-called spectral phase, has a strong influence on the effective pulse duration of the laser. While the amplitude defines the ultimate pulse duration achievable, also known as the Fourier-transform limit, the phase carries the information on the actual pulse shape including for instance the stretch of the pulse in CPA and also all perturbations related with chromaticity in the amplification. The formalism around the spectral phase has been a central topic of the ninety-nineties when effects of the various components and their possible interaction have been studied in length. The subject is worth a full review that falls out of the scope of this manuscript. One could for instance recommend the review article by A. Weiner [62] that describes the many measurement and control methods that can be applied to short pulse lasers for amplifying high temporal-quality pulses. Following the spectral phase formalism, a Taylor-series development of the phase around the central laser frequency is often made to have a heuristic approach where all first terms in the development can be related to physical effects. The first two terms are propagation effects that enter in the description of the carrier-envelope phase, while the second and third are related to the lowest order stretch terms. Higher order terms have been until now ignored because it was believed that such terms play a minor role on the pulse profile. However, recent developments on temporal contrast, i. e. the pulse fidelity on a high dynamic range, show that this is not the case. This aspect is covered later in the manuscript (see chapter 2.3).

1.3.3 Spatial aspects

The third parameter of interest for high-fidelity amplification is the beam quality throughout and at the output of the laser. This aspect is of very high importance for modern high-energy lasers because the sources of beam quality degradation are manifold. There are two aspects to the problem: firstly the necessity to manipulate the spatial mode of the laser and secondly the requirement for high-fidelity amplification.

With the development of high-energy lasers, the need for spatial efficiency becomes more stringent, that is to maximize the amount of joules per surface area that amplifiers can deliver. This has an implication on the intensity profile of the beam as the standard TEM_{00} mode generated by

beam shape (Gaussian order)	2	10	20
aperture size ($\times$ ω)	4	2.19	2.07
fill factor (%)	12.5	66	82

Table 1.2: Beam aperture and corresponding fill factor for different (round) beam profiles

laser cavities is not efficient enough. Indeed, a Gaussian beam with a full width at $1/e^2$ equal to $2\,\omega$ (beam waist), must propagate through apertures larger than $4\,\omega$ in order to avoid significant diffraction effects. For a 10^{th}-order super-Gaussian beam, this aperture reduces to $2.19\,\omega$ and $2.07\,\omega$ for a 20^{th}-order super-Gaussian one. Here an important parameter to consider is the fill factor of the beam through the aperture as indicated in table 1.2 and defined as the ratio of the energy of a given beam through an aperture to the maximum energy that this aperture can admit when illuminated with a constant fluence. In other words, super-Gaussian or "top hat" laser modes are much more efficient (up to 7 times for a 20^{th}-order super-Gaussian mode).

Unfortunately, super-Gaussian laser beams are not self-similar modes and they rapidly diffract. In particular, a propagating "top hat" beam exhibits a varying on-axis intensity that shows an increase in the intermediate field with a factor as high as 4 times the beam intensity in the near field, which can lead to damage in the amplifier. As a rule of thumb, the distance over which the beam diffraction can be neglected is inversely proportional to $(\text{order})^2$ and, as a consequence, laser amplifiers using "top hat" beams must use image relaying to avoid diffraction effects. In addition, other technical or experimental considerations might require more complicated beam profiles as illustrated in fig. 1.6, showing a selection of laser beam profiles used at three representative high-energy amplifiers. The titanium-doped sapphire petawatt laser systems need to efficiently extract energy from the last amplifier with an extraction efficiency from 40 to 50 %. Here, a top-hat profile is necessary for a good overlap with the pump laser and an optimal use of the amplifying crystal (fig. 1.6.b). In kilojoule short-pulse neodymium-doped glass lasers, another complication comes from the compressor that might use tiled optical gratings [69]. In this scheme, at first, energy density efficiency is reached by the use of square "top hat" beams and secondly, stripes are introduced in the beam to avoid damage at the grating interface during compression (fig. 1.6.a). Multi-100 joule lasers have enough energy to allow pump-probe setups with low temporal jitter by propagating two sub-apertures that are spatially separated close to the experiment (fig. 1.6.c). While all this has no direct influence on the beam quality, this adds a complexity layer to the optical system on which amplifiers are based.

While spatial amplitude shapes are dictated by technical boundary conditions in the amplifier and/or technical requirements of the experiments as illustrated in fig. 1.6, spatial phase modulation is in general unwanted and imposes on the opposite a very strong perturbation to the beam, that is particularly strong in the mid and far fields where the phase-to-amplitude coupling is the strongest. The origins of the spatial phase modulation are manifold and the resulting beam aberration is often divided in three categories depending on the source of the aberration: static, thermal and shot-induced.

Static aberrations are created by non-perfect components or misalignment. It is possible to estimate the growth of the aberrations with the number of components and given the complexity of the amplifier, the tolerable amount of aberration per element can be determined. From this, one

[6] Permission to re-use and adapt the shown figures has been granted by the respective authors

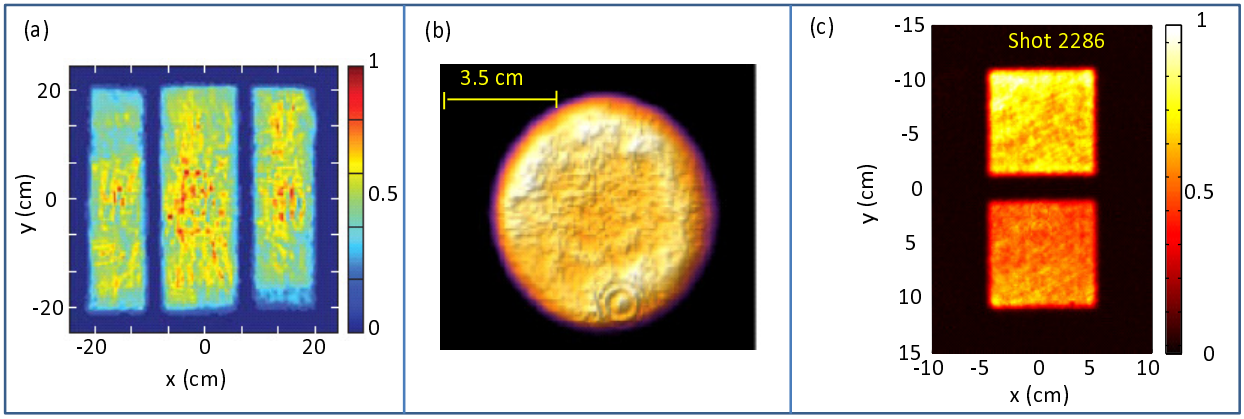

Figure 1.6: A selection of beam profiles used in high-energy short-pulse lasers(a) Near field image of the kilojoule laser beam of Omega EP (adapted from [70]). The beam is made of vertical stripes to match the structure of the short pulse compressor. (b) near field of 45-J 1.5-PW PULSER laser in Korea (from Yu et al. [71]) showing atop hat profile adapted to energy extraction in the main rod amplifier. (c) Two-beam profile used at the PHELIX laser facility for applications.[6]

understands that laser amplifiers are not infinitely scalable as the requirements increase when the number of components and their size grow until the physical limitation of the fabrication technologies is met. With the complexity of high-energy laser amplifiers, it is not possible to simply specify components that deliver a beam of high spatial fidelity after the amplifier. Given that the resulting beam aberration can evolve in time because of re-alignment or exchange of components, it is clear that wavefront corrections using static phase plates are not efficient. Instead, programmable devices like deformable mirrors exploiting the technical developments made in astronomy associated with wavefront measuring devices like the Shack-Hartmann sensor [72] or three-wave lateral shearing interferometry [73] must be employed. In addition to static aberrations, drifts in the wavefront aberration due to the thermal loading or the instantaneous change of temperature in the laser amplifiers at the time of the shot complicate the delivery of high-fidelity beams.

While the principles of adaptive optics are straightforward and intuitive, the following aspects are mandatory for a high spatial-fidelity of the amplification:

- High-performance metrology. The metrology of high-energy short-pulse-duration lasers is of foremost importance for almost all applications. Here the complication comes from the simultaneous need to reduce the beam from the amplifier size to a size compatible with detection equipment like cameras, the need to be achromatic and introduce as little dispersion as possible for high-fidelity temporal measurements, the need to reduce the beam energy from many joules to nanojoules uniformly across the beam aperture and introduce as little distortion like aberrations or non-linear Kerr effect as possible. In the current state of the art, this is a very complicated matter where nowadays one must still make trade-off in performance.

- Closed-loop wavefront control divided in amplifier and beam transport. Wavefront control can be introduced in principle in any portion of the amplifier where the propagation is linear. Ideally, the beam wavefront can be pre-compensated by adpative optics at any place to provide a perfectly corrected wavefront at any given place. Unfortunately, non-linear elements like pinholes or the compressor that creates spatio-temporal coupling impose serious limitations to this strategy. Pinholes in spatial filters used to improve the beam quality by removing high

spatial frequencies limit the amount of wavefront pre-compensation by cutting in the low-order spatial frequencies and introducing an unwanted phase-to amplitude modulation. Pulse compressors require perfect (flat) wavefronts to correctly work and avoid spatio-temporal coupling. That imposes that the strategy in wavefront control should be aiming at correcting for aberration before the compressor. An additional wavefront control system might address the beam transport distortion when the latter is complicated and prone to aberration.

In conclusion, the subject described in the previous pages shows how much development has occurred since the invention of the ruby laser in 1960 by Theodore Maiman. High-power lasers are now widespread research tools that come in various energies, pulse durations and average powers. The high-power lasers based on the CPA technique have opened a new field of research on physics at high energy densities and relativistic intensities that finds plenty of applications. For instance, lasers are actively being used to study wakefield acceleration, a particle acceleration method now seriously considered with conventional drivers by many large institutions like the CERN [74] and SLAC [75] heavily involved in preparing tomorrow's accelerator concepts. However, generating the necessary laser intensities is not an easy task when finely controlled and stable parameters are required. Under that prospect, high-intensity lasers have also made some tremendous progress to deliver well-characterized, stable and versatile interaction conditions, where high-fidelity amplification is a central issue. In the following, a particular insight in two aspects of modern high-intensity lasers is given: temporal contrast and beam shaping. First the requirements for high-fidelity pulse amplification on a high dynamic range are reviewed in details, together with the physical origins of the current limitations and secondly solutions that have been implemented or could be tested are described. Eventually, a series of peer-reviewed articles which I published on the subject are illustrating my contribution to the field. The third chapter is dedicated to the high spatial fidelity in laser amplifiers which needs to be realized for various beam shapes and under the requirement for high average power. This aspect is a recurring theme in laser development and it is natural that I had to work on it at times from my PhD work to more recently with my students. This chapter is illustrated with three articles where beam fidelity is a the centre of preoccupation.

Chapter 2

Temporal contrast in modern high-intensity lasers

The amplification of laser pulses has been very logically a central topic of development ever since the invention of the laser in 1960. It is nowadays possible to reach amplification factors over 10^{12} in high-energy short-pulse lasers, bringing the nanojoule pulses generated by laser oscillators to energies in excess of 1000 J [1]. Such a high amplification factor is inherently bringing the issue of amplification noise to the forefront of preoccupations. In addition the temporal fidelity of the amplification is also critical, since techniques like "chirped pulse amplification" [3] strongly modify the temporal profile of short pulses to successfully amplify them beyond the damage threshold limit of laser materials.

An important concept associated with the temporal pulse fidelity is the temporal contrast that defines the amplification fidelity on a high dynamic range. The temporal contrast is in general defined as a ratio between the pulse intensity or power at an instant before the maximum of the pulse is reached to this maximum. Power and intensity contrasts depends on whether the temporal contrast is considered in the near field (power contrast) or far field (intensity contrast). This differentiation comes from the incoherent nature of the noise responsible for the contrast degradation which has spatial properties different from the coherent laser beam. Devices like the high-dynamic range cross-correlators commercially available make power contrast measurements while experiments done at the focus of the laser will be sensitive to the intensity contrast.

Fig. 2.1 gives a schematic representation of the temporal profile of a short pulse laser illustrating the problematics. The time and intensity axes are given on a logarithmic scale, with $t = 0$ being the time at which the pulse reaches its maximum. As shown, the "real" pulse profile is dramatically different from the ideal Gaussian temporal profile. The vertical axis gives the maximal focused intensity achievable with petawatt-class lasers and the coloured areas depict the type of interaction between the laser pulse and matter. Outside the lowest area, the laser-matter interaction is strongly non-linear. As can be seen, the laser pulse has a complex structure that can be divided in several components:

- A microsecond-long pedestal that stays in general below the ionization threshold of materials. The origin of this pedestal is the amplified spontaneous emission (ASE) created by the last large-aperture amplifiers that are not isolated by active time-gating devices used to isolate the target from the amplifier. Although the amount of energy included in this pedestal can be of

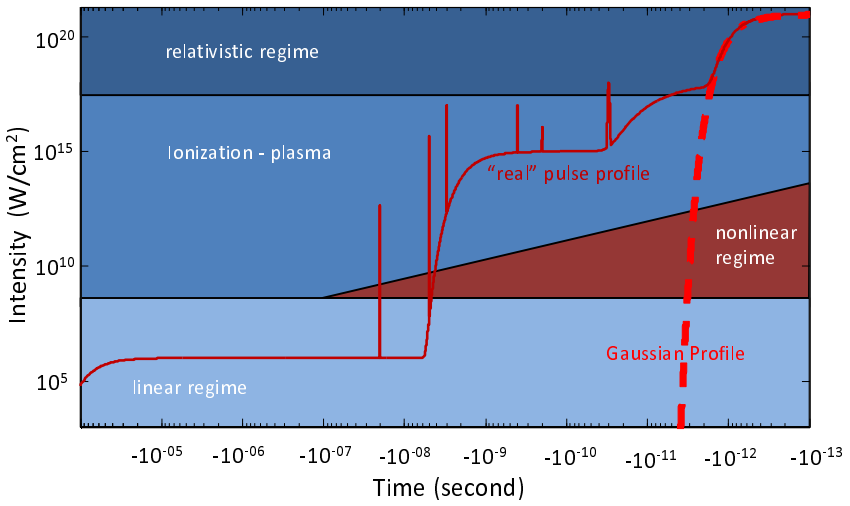

Figure 2.1: schematic representation of the temporal profile of a 1-ps-long (FWHM) laser pulse (solid dark red) compared to an equivalent Gaussian pulse (doted red). The time is represented logarithmically.

the order of micro- to millijoules, its spatial coherence is poor so that the on-target intensity stays below the ionization damage threshold of the target. This pedestal is in general of little importance and rarely considered in the literature, although it can lead to significant pre-heating of the material when the latter is absorbing. When this is the case, an additional active isolation stage should be implemented as close to the target as possible. For that, standard Pockels cells with an aperture as large as 10 cm can be used while larger beams require the more sophisticated plasma electrode Pockels cell design capable of working with large dimensions.

- A second pedestal, lasting one to ten nanoseconds, is created by ASE or nonlinear fluorescence generated early in the amplifier and in general by the very first stage of amplification [76]. This pedestal is in general intense enough to ionize matter yielding a fully developed pre-plasma cloud in front of the target, radically changing the type of interaction. This pedestal is also able to blow off very thin targets (below roughly 10 micrometre) and it has been until recently a major limiting factor for many applications using ultrashort laser pulses. Its effect and remedies are discussed in the following pages.

- Prepulses. Prepulses can happen on long (nanosecond) time-scales because of leakage and beating effects when more than one laser cavity are used. This is particularly true for systems using regenerative amplifiers. Nanosecond prepulses are typically easily detected and kept under control with fast optical switches like Pockels cells. Prepulses occur also on a picosecond time scale. The origin of these pulses lies in optical components with parallel surfaces. Multiple internal reflections yield post-pulses that can be quite powerful, in particular when this happens in a regenerative amplifier. In chirped pulse amplifiers, main and post-pulses are stretched and overlap temporally, creating a localized interference taking the form of a temporal modulation. This modulation can in the presence of B-integral (temporal Kerr effect) create a temporal phase modulation that translates into pulse replica after compression, also in front of the main pulse [77]. This effect is hard to detect because the devices used for the measurement of the temporal contrast cannot efficiently discriminate between

pre- and post-pulses but it is strong enough that one can use it as a direct measurement of the B-integral of a laser amplifier [78].

- Slow picosecond and femtosecond rise time. A slow rise of the temporal profile is observed in CPA systems quite systematically on a time scale related to 10 to 100 times the pulse duration. This slow rise is particularly obvious in the latest laser systems that were commissioned because their nanosecond pedestal is very low and does not hide this effect any more. This effect is one of the most severe limitations in today's systems as its origin is not clearly understood as explained below in the section 2.3.1.

- Low-order spectral phase effects. The effect of low-order phase terms on the pulse quality is well understood [79]. The elements able to create this distortion have been studied in details and can be corrected: many measurement techniques like SPIDER [80], FROG [81] or SRSI [82] and a few programmable controllers are available to precisely handle those [83]. Here, an effect of low-order spectral phase terms results in general in a pulse pedestal in the range of 1 to 10 times the pulse duration and lower peak intensity. A lower peak intensity is problematic for the temporal contrast as it reduces the contrast by reducing the peak intensity while the other components of the pulse remain unaffected.

In this chapter, the requirements for the temporal contrast are analyzed from an experimental point of view. Functional requirements imposed by the current limits of numerical simulation tools have to be considered, too. Then the sources of temporal contrast degradation are presented and finally, remedies and mitigation methods are described.

2.1 Requirements on the temporal contrast of short laser pulses

CPA lasers exhibit characteristic temporal contrast features that have been responsible for experimental complications and uncertainties for a long time. In the literature, the contrast is often brought forward when physical effects are being discussed and observations are interpreted. Because of this large influence on experimental outcomes, the temporal contrast and its implications has been a recurring subject of study of the last two decades, in order to deliver light pulses with good or controlled temporal profile properties. However, the temporal contrast is often influenced by many variable factors which cause it to vary from one system to the other and even evolve in time, requiring constant monitoring. This uncertainty in the experimental conditions could explain for instance why some results are not systematically reproducible, even when the usual experimental parameters like energy, pulse duration or intensity seem similar. In addition, the pulse temporal profile being complicated, it is very difficult to reduce the temporal characteristics of a pulse down to a single number that would be needed for quantitative comparisons.

2.1.1 Ionization threshold

At the ionization threshold, the medium interacting with the laser turns into a plasma, which exhibits particular properties [84] and in particular, follows fluid dynamics. When the ionization happens early enough before the maximum of the laser intensity, hydrodynamical effects can be significant and lead to the formation of a pre-plasma plume. This is caused by ionization and/or heating of the target in the few nanoseconds preceding the maximum of the intensity. The main parts of the pulse profile at stake here are the pulse pedestal and prepulses.

There exist empirical data on damage threshold reported in the literature that can be used to infer the ionization threshold and deduce quantitative requirements on the temporal contrast of laser pulses [85,86]. The mechanism at play in the initiation of laser-induced damage is a step-wise ionization and/or electron oscillation in the electric field and collision process. During the collisions, electrons are freed (avalanche) or transfer momentum to the lattice (heating). Since the density of electrons available at the initiation of the damage depends on the type of material (metal, absorbing or transparent), different damage thresholds can be expected.

For absorbing materials or metals, electrons oscillate in the electric field and when they collide with the lattice, they transfer their momentum to it and heat it. On the opposite, for dielectrics, the photon energy is not high enough to ionize electrons so a non-linear atomic process like multi-photon ionization has to take place. The experimental values found for dielectric materials however never matched the predicted values. For those dielectrics whose band gap is much larger than the photon energy, the current assumption is that localized defects like absorbing particle inclusions or lattice defects create a local collapse of the band gap enabling multi-photon ionization [87]. This effect considerably reduces the effective damage threshold of dielectric materials such that the ionization threshold of all materials (metals and dielectric) spans only from about 1 to 100 J/cm^2 when they are submitted to a 1-ns long laser irradiation. In terms of ionization intensity threshold, this corresponds to 10^9 to $10^{11}\,W/cm^2$. For a laser capable of reaching $10^{21}\,W/cm^2$, this would set the requirement on the nanosecond-long pedestal to 10^{-10} to 10^{-12} depending on the target material.

The initiation of the plasma depends also on the laser pulse duration. For dielectrics, a rule of thumb states that the plasma threshold follows a square root function of the laser pulse duration [85]. This law has been experimentally verified to be valid in the nanosecond range from roughly 10 ps to 10 ns, over 3 orders of magnitude. This is exactly the time span covered by the nanosecond pedestal in chirped pulse amplifiers. In other words, the damage threshold intensity increases by a factor of 10 for dielectrics when the pulse duration decreases from 1 ns to 10 ps. For metals, the ionization mechanism is different and is based solely on heating. Here two different time scales must be distinguished: first the thermalization time scale between electrons and lattice and second, the diffusion thermalization time scale [88]. The first thermalization happens in the range of a few hundreds of femtoseconds and is not relevant for the temporal contrast issue. That means that the laser energy is quickly transferred to the lattice independently of the duration of the energy delivery. For that reason, the laser-induced damage threshold of metals is independent of the pulse duration as long as thermalization diffusion can be neglected. However, when the pulse duration is long enough so that the target is volumetrically heated, the damage threshold follows again a square root function of the pulse duration. This usually happens for pulse durations significantly longer than 1 ns. When one looks at the damage threshold intensity, metals exhibit then an inversely proportional dependency on the pulse duration and therefore their damage threshold intensity reaches nearly $10^{12}\,W/cm^2$ for picosecond pulses.

Most of the laser-induced damage values are reported for large millimetre-size laser spots while experiments involving high-intensity lasers work with micrometre-size interaction volumes. This has two positive effects on the evolution of the plasma threshold: first thermal heat diffusion happens in a three-dimensional volume instead of a quasi one-dimensional geometry. This has as effect an increase of the damage threshold for metals in the nanosecond regime. And second, the statistical chance to hit a weak spot in dielectrics decreases with the laser spot size and laser-induced thresholds closer to the multi-photon ionization thresholds are observed [89].

For a gaseous medium, ionization is much less dominated by collective plasma effects and atomic

physics play a central role. The ionization follows then the multi-photon ionization or tunnel ionization models but in any case this is happening at a much higher intensity than for solid state media, as cascade and avalanche effects are much less dominant. For atomic gases, ionization level at around 10^{13} W/cm^2 is usually observed.

2.1.2 Ablation and pre-plasma expansion

Once the ionization threshold is reached, matter is vaporized and expands as a plasma gas into the vacuum. The amount of matter that is ablated at the ionization threshold is however very small. Taking into account the vaporization energy density of material and a plasma threshold of joules per squared centimetres, one can estimate that, at the ionization threshold, the absorbed energy is able to vaporize a 100-nm-thick layer of the target at best, leaving the rest of target at near solid density. Nevertheless, once the plasma is created, it expands into the vacuum.

There is a simple one-dimensional model that is able to describe this phenomenon, in which the plasma is considered as isothermal, charge neutral and its electrons have a Maxwellian energy distribution [90]. At $t = 0$, the plasma starts to expand into the vacuum and after an instant dt, the density at the interface follows an exponential decay profile around a volume that is limited by the distance covered by the ionic sound wave. The solution is self-similar, that is its shape does not change in time, and can be plotted for the dimensionless spatio-temporal parameter ξ with $\xi = x/(S_0\,dt)$ where dt is the expansion time, x the space coordinate and S_0 the ionic sound velocity:

$$S_0 = \sqrt{\frac{Z_i k_B T_e}{m_i}} \tag{2.1}$$

where Z_i and m_i are the ionization degree and mass of the ion species in the plasma and T_e the electron temperature of the plasma. In such a case, the plasma density n is given by:

$$n(\xi) = n_0 Z_i e^{-(\xi+1)}, \text{ for } \xi > -1 \tag{2.2}$$

where n_0 is the initial plasma ionic density. This simple model illustrated for a fully-ionized hydrogen plasma in fig. 2.2 is valid for the first instants after the plasma has been created. It supposes the plasma temperature remains constant during the expansion and that radiative cooling is negligible. The one-dimensional aspect is also maintained as long as the plasma expansion remains small compared to the focal spot diameter.

Eq. 2.2 is of interest because it links the position of a given plasma density to the time and electron temperature. In particular, one can find an expression of the location of the critical density of the plasma, that is the electron density n_c at which the laser field is not able to propagate in the plasma cloud any more:

$$x_{n_c} = S_0 \left(log\left(\frac{n_0}{n_c}\right) - 1 \right) dt = \sqrt{\frac{Z_i k_B T_e}{m_i}} \left(log\left(\frac{n_0}{n_c}\right) - 1 \right) dt \tag{2.3}$$

where n_0 is the initial plasma electron density. As shown above, the position of the critical density depends on the electron temperature, which depends on the laser intensity. In other words, a higher laser intensity leading to a higher electron temperature and high plasma ionization grade will expand faster into the vacuum.

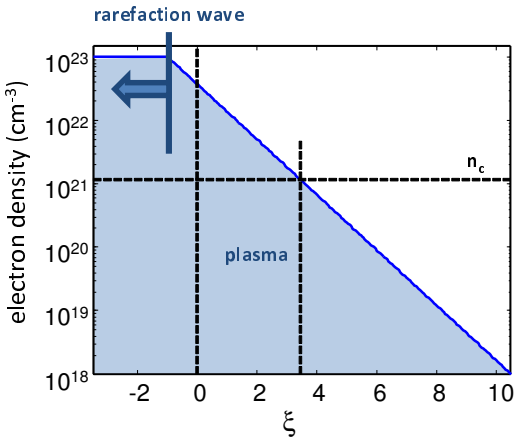

Figure 2.2: Plasma expansion in the vacuum: n_c: critical plasma density for a 1 µm laser wavelength, ξ: dimensionless space parameter with $\xi = x/(S_0 \times dt)$

It is clear that such a pre-plasma expansion happening at an uncontrolled time before the peak intensity is reached can be detrimental to the meaningful interpretation of experimental data. In addition, the precise simulation of this pre-plasma meets the current limits of simulation methods because of the extremely complicated hydrodynamics at play from the ionization threshold to the relativistic regime some picoseconds before the peak. Therefore, it is in general necessary to prevent such an uncontrolled expansion and keep it small. When this is not the case, propagation effects of the laser like self focusing and filamentation happen and change the experimental conditions, and discrepancies with simulations can arise. For planar targets, a flow of the plasma over a distance of a laser wavelength λ is in most cases tolerable and has little impact on propagation and the target areal density. This condition can be written as:

$$\sqrt{\frac{Z_i k_B T_e}{m_i}} \left(log\left(\frac{n_0}{n_c}\right) - 1 \right) dt < \lambda \tag{2.4}$$

When the plasma is hot and the charge-to-mass ratio large, the plasma expands faster while lower intensities can be tolerated for a longer time. To assess the criticality of this condition, the expansion time necessary for the critical density to reach λ for various materials (gold and carbon) was calculated as a function of the laser intensity and compared to a realistic temporal profile in fig. 2.3. For the simulation, a relation between laser intensity and plasma temperature must be applied to eq. 2.4, which was assumed based on empirical plasma temperatures of 70 eV and 550 eV at 10^{12} and 10^{15} W/cm^2 respectively, as found in the literature in [91] and [92], with a scaling law following a power of 1/3 of the intensity. This scaling is valid as long as the plasma is not relativistic, that is below 10^{18} W/cm^2. Above this value, the light pressure cannot be neglected any more and the plasma does not expand in the same way as long as the laser pulse is "on". For comparison, a maximum laser intensity equal to 10^{20} W/cm^2 and a Gaussian 400-fs-long laser pulse together with a "real" laser pulse as measured at PHELIX is shown. The curve for carbon assumes a fully ionized carbon plasma (C^{6+}). The gold plasma on the other hand is a bit more complicated to simulate because gold is not fully ionized at the lower intensities and the mean ionization grade depends on the laser intensity. The mean ionization grade is estimated by assuming that the ionization energy equals the plasma temperature (local thermodynamic equilibrium conditions). The ionization energies of the gold ions have been retrieved from the NIST database [93]. In

addition, the time-dependent ionization threshold for metals and dielectrics are indicated in fig. 2.3 together with the ionization threshold for low density gases.

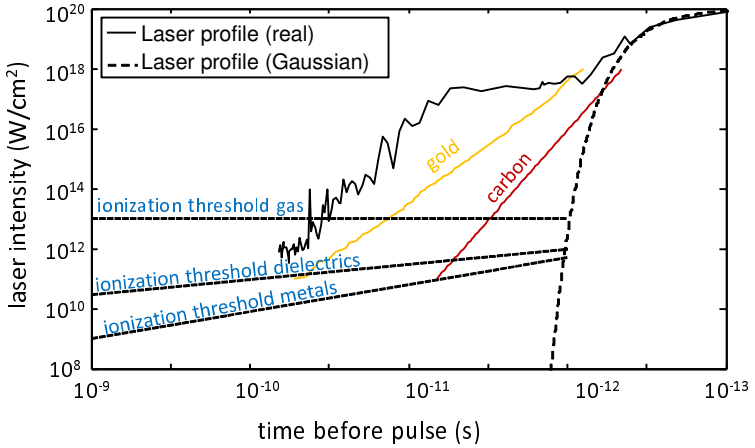

Figure 2.3: Conditions for an unchanged target as a function of the time before the pulse.

For the ideal Gaussian sub-picosecond pulse, the laser intensity rises fast enough compared to the expansion limit such that one can consider that a target illuminated by such a laser pulse remains undisturbed until the relativistic regime is reached. In such a case, the use of numerical prediction tools like PIC codes (see next section) is probably highly relevant because the target remains mostly undisturbed and relatively cold until a few picoseconds before the interaction. On the other hand, the realistic pulse profile as reported for the PHELIX laser for instance shows that the laser intensity rises slowly and probably ionizes the target already 100 picoseconds before the maximum of the pulse. Compared to the tolerable limit given for gold, the temporal intensity is 2 to 3 orders of magnitude too high at a given time before the pulse maximum to ensure the target remains unchanged. Here the simulation of the interaction should take the pre-plasma expansion into account, which is a very complicated task.

Another interpretation of the plot in fig. 2.3 shows that the one-dimensional plasma expansion corresponding to the realistic pulse profile is 5 to 10 times faster than one can tolerate for "clean" interaction conditions. In reality, for this type of profile and expansion, three-dimensional effects cannot be neglected: the plasma flows out of the focal area and the effective areal density of the target changes.

2.1.3 Requirements and validity domains of numerical simulations

One of the most fundamental goals of physics is to be able to predict behaviours and explain phenomena as per the determinism principle. In this view, simulation codes are essential tools that enable running numerical experiments which compared to experiments validate or invalidate the underlying theoretical models.

There are two approaches to simulating laser-plasma interaction: whether the plasma can be considered as a fluid or individual particles have to be followed. Hydrodynamical simulation codes, e. g. HELIOS [94], RALEF [95], consider the plasma as a fluid and are very well adapted to describing laser-plasma interaction when the plasma can be considered in local thermodynamic equilibrium and the coupling of light into matter happens through collisions as per inverse bremstrahlung or

resonance absorption. These types of plasma are usually relatively cold and generated at an intensity of $10^{12}\,\mathrm{W/cm^2}$. However, when the laser intensity is reaching the relativistic regime, the electrons acquire a very large velocity in the laser field which in turn reduces the collision cross section with the cold surrounding plasma and the plasma becomes very quickly inhomogeneous such that the concept of temperature is then difficult to define. Here a simulation of the individual trajectories of the charged particles in the plasma must be performed, which is done by kinetic simulation codes [96], using either individual particles or particle distribution functions (Vlasov).

The difficulty with kinetic simulations is the large number of particle to follow and their multiple electro-magnetic interactions, which makes the simulation extremely computation intensive. An valuable approach is found with particle-in-cell (PIC) codes, the principle of which can be found in various books [97]. These are kinetic simulation codes that calculate the fields on a grid and simulate the plasma by following a representative number of particles. They are particularly suited to describe the laser-plasma interaction in the relativistic regime. Electromagnetic PIC codes like OSIRIS [98], VLPL [99] or EPOCH [100] can be used to solve the Vlasov-Maxwell coupled equations that describe the interaction of charged particles and an electromagnetic field, where the Maxwell equations describe the evolution of the fields and the Vlasov equation the particle density evolution. In addition, the PIC code enables to add short-range individual collisions or other effects not covered by the collective motion equations.

In a PIC simulation, the particles are followed in one or more spatial dimensions of the continuous space while the field is discretized on a grid to make the simulation more computation-time efficient. Fig. 2.4 schematically gives the several calculation steps that take place in a single iteration time step of a PIC simulation that alternate equation of motion and actualization of the driving fields based on the updated charge and currents. PIC codes differ in the computational methods used for running the loop, and flavours of the same code can incorporate different physics effects built in the kinetics step. PIC simulations, especially when made in three dimensions can be quite computer intensive. For instance, a simulation in three dimensions over many tens of femtoseconds able to track the fine effects in electron acceleration will need up to 10^5 CPU hours and may need to run on massively parallel computers with many tens of thousands of cores to deliver simulations within a few days.

There are strong discretization requirements to obtain sensible PIC simulations. In the spatial domain, the grid needs to resolve the Debye length of the plasma given by:

$$\lambda_D = \sqrt{\frac{\epsilon_0 k_B T_e}{e^2 n_e}} \tag{2.5}$$

where $\mathrm{T_e}$ and $\mathrm{n_e}$ are the temperature and density of the electrons respectively. The Debye length or plasma screening length is an important parameter and a proper simulation that needs to take into account electrostatic effects like PIC codes must resolve it. When this is not the case, the plasma is not properly sampled and aliasing effects (numerical heating) change the plasma conditions in an non-physical manner. In the time domain, the time steps must be adapted to the spatial grid size following the Courant condition such that $\delta \mathrm{t} < \mathrm{c}\,\mathrm{dx}$. That means simulation steps in general much below 1 femtosecond. In particular plasmas requiring a small grid size are particularly difficult to simulate with PIC codes because the simulations become very CPU intensive. This case is exactly that of cold and dense plasmas, which describe the conditions created by prepulses or at the threshold of the ionization during the rising slope of the pulse.

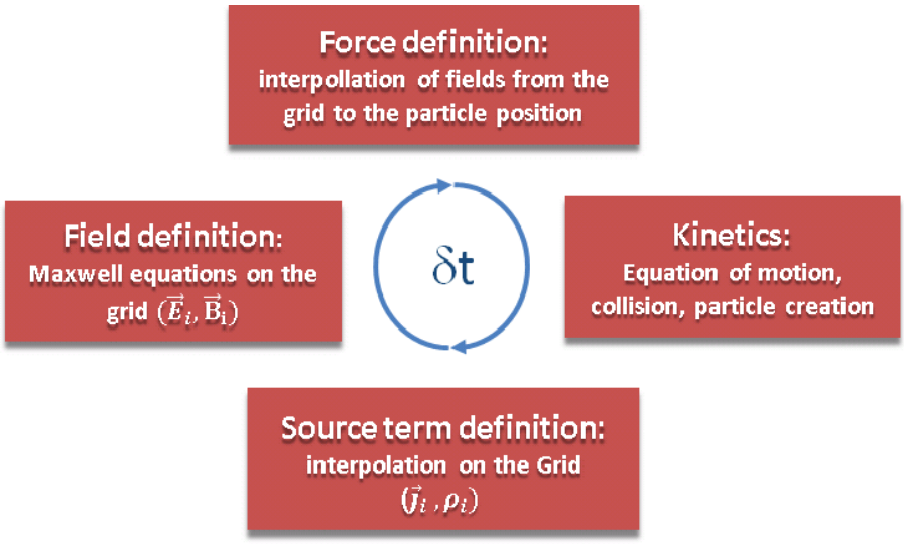

Figure 2.4: Principle of the PIC code: to gain computational power this simulation technique describes the fields on a grid and follows macro-particles describing the plasma.

In consequence, PIC codes, that are reliably describing the relativistic laser plasma interaction, are not able to efficiently simulate the cold plasma for temperatures at or below 1 keV that are met during the rising slope of the laser intensity between 10^{14} and 10^{18} W/cm^2. For the simulation, a strong hypothesis on the target conditions (shape, density, temperature) at the initial time of the calculation must be done, because PIC codes are not able to render the effect of the laser on the target at the beginning of the interaction. These start conditions cannot be correctly predicted by hydrodynamical simulation either, although one should note that an effort to overcome this has been made with the introduction of hybrid PIC codes [101] that threat hot non-thermal particles in a warm hydrodynamic plasma and emulate the two-temperature electron temperature behaviour observed in interaction experiments.

As a conclusion, given the difficulty to simulate the interaction of laser with matter from the ionization threshold to the relativistic regime, it is essential to ensure that the targets stay unchanged until the relativistic regime is reached; and therefore this requires light pulses of outstanding temporal quality.

2.2 Amplification noise

Amplification noise is responsible for the pulse pedestal structure as schematically depicted in fig. 2.1. The level of the pedestal depends on the type of amplifier and optical elements used to maintain noise at a low level. ASE noise starts temporally as soon as the amplifier is pumped, typically some microseconds before the maximum of the pulse. Temporal gating might be used here to reduce the noise to a tolerable level. On the nanosecond scale, temporal gating is not possible without cutting into the stretched laser pulse itself so the full effect of the ASE is felt some nanoseconds before the peak intensity is reached. This is depicted by the second step on the pedestal in fig. 2.1 that typically exceeds the ionization threshold of materials. This nanosecond ASE level has been repeatedly reported to lie between 60 and 80 dB below the maximum intensity of the pulse.

There are two equivalent approaches used to predict the level of ASE in a laser amplifier. One of them is based on slice-wise photometric estimates of the level of ASE generated by the fluorescence in the laser medium and amplified along the beam path [102]. Here, the local spontaneous emission per time and unit volume is estimated based on the excited ion density in the amplifier and excited state lifetime of the lasing transition on one hand, and emission solid angle and gain bandwidth of the amplifier together with amplification effects along the beam path, on the second hand. Finally the contribution along the whole amplifier is summed up to give the ASE power density.

In a second more general approach though, one can consider laser amplifiers as generic linear quantum amplifiers that will also amplify noise photons [103]. The noise photons are present in the vacuum and amount to half a photon per mode in space and time. For gains G much larger than one, the amplifier increases the signal-to-noise ratio by a factor of two such that the noise seen from the output of the amplifier looks like coming from one background photon per mode undergoing an amplification factor G. If we consider that one is able to select the exact spatial mode filled by the fully spatially-coherent laser beam, the problem restricts itself to the one-dimensional problem of temporal noise. In the time domain, the duration of a temporal mode is related to the coherence length of the electric field or in other words to the inverse of the amplifier spectral bandwidth. This argument holds in general true as the bandwidth of a laser amplifier is the main constraint to the pulse spectrum.

For the Omega-EP facility [1], the peak power of the laser is in the range of one petawatt, while the noise level is given by the energy of a photon at the laser wavelength (1050 nm), the gain factor (10^{13}) and the coherence length of the amplified noise ($\delta t = 0.44/\text{bandwidth}$ for Gaussian pulses). The signal-to-noise ratio (SNR) is then:

$$SNR = \frac{0.44\ P}{E_{photon} \times Gain \times bandwidth} = \frac{0.44\ P\ \lambda^3}{h\ c^2\ \delta\lambda} \tag{2.6}$$

It is interesting to note that the SNR in laser amplifiers according to the quantum theory depends on λ^3 in the same way as the ratio of the Einstein coefficient B and A of the rate equations. For the above given example, the numerical application gives:

$$SNR = \frac{0.44\ 10^{15} \times 1.05^3\ 10^{-18}}{6.63\ 10^{-34} \times 10^{13} \times 9\ 10^{16} \times 4\ 10^{-9}} = 2.13\ 10^8 \tag{2.7}$$

The value found represents however a limit which is relatively hard to reach. It supposes that the amplifier is providing a gain for the noise that equals the gain in energy for the main pulse. This is in reality altered as the laser pulse undergoes losses, like mode mismatching into the amplifier or saturation effects for instance, which requires the gross gain of the amplifier to be much larger than the net gain in energy.

Another way to look at the problem is to re-write eq. 2.6 with the approximation that an amplified pulse is also bandwidth limited. Eq. 2.6 reduces then to:

$$SNR = \frac{E_{in}^{eff}}{E_{photon}} = N_{in}^{eff} \tag{2.8}$$

where E_{in}^{eff} and N_{in}^{eff} are the energy and number of photons effectively coupled into the amplifier respectively. The effective coupled energy takes into account coupling losses into the amplifier so that the amplifier gains for both noise and signal are equal. This result demonstrates that the temporal contrast problematics reduces to the optimization of a simple parameter, namely the

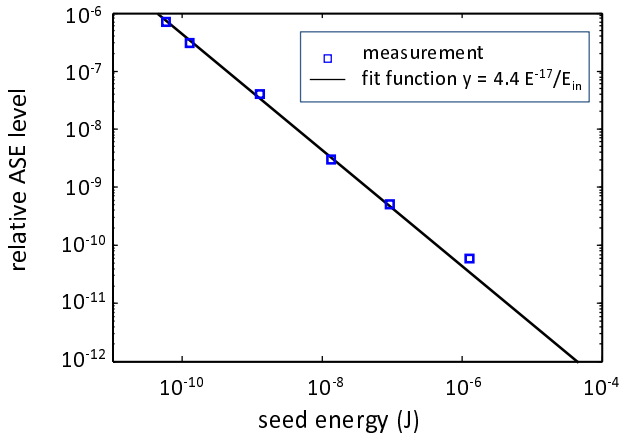

Figure 2.5: nanosecond ASE dependency on the seed pulse energy in a CPA laser system (PHELIX, 2012).

number of photons available before the amplifier. The validity of this prediction has been also experimentally studied in my group by Dr. Wagner, as shown in fig. 2.5, and is a central result of his PhD work. This plot shows the relative level of the nanosecond ASE of the PHELIX laser as a function of the seed energy which was adjusted by changing the gain in the parametric pre-amplifier as described later in the article by F. Wagner et al. page 52. When PHELIX is run in standard CPA mode, the oscillator pulses are directly stretched and the amplifier is seeded with pulses of less than 50 pJ energy, yielding an ASE relative level of 7×10^{-7}. As the energy of the seed pulse is increased, the relative ASE level drops as an inverse function of the seed energy. The measurement was performed over 4 orders of magnitude, only limited by the measurement threshold of the scanning third-order autocorrelator used for the measurement (Sequoia, Amplitude Techn. SA). The fit function shows that the data follow the linear dependence prediction, validating our assumption.

At the standard injection level for the PHELIX facility, the number of seed photons equals 2.6×10^8, a value remarkably similar to the theoretical SNR value found in eq. 2.7 for the OMEGA-EP facility underlining that the noise problematics is a universal one. However, the corresponding temporal contrast level should equal 4×10^{-9} at PHELIX, a SNR value being significantly different from the experimental temporal contrast value reported in fig. 2.5. This difference can be attributed to several effects: first, the laser pulse generated in the oscillator is nearly five times shorter than what the amplifier bandwidth allows and second, the coupling efficiency to regenerative amplifiers being notoriously low, the regenerative amplifier used at PHELIX is reducing N^{eff} even more. From this ratio, one sees that the coupling efficiency into the PHELIX amplifier equals 1/180.

Note that with this approach, it is clear that arguments brought forward at the beginning of the year 2000 with the introduction of optical chirped pulse amplification (OPCPA) [104] turn out to be wrong. At that time, OPCPA was proposed as a noise-free amplification technique because it does not suffer from amplified spontaneous emission. While the latter is true, parametric amplification suffers from parametric amplification noise or parametric fluorescence that yields more or less the same pulse pedestal. This idea is the central finding of the publication presented on page 38.

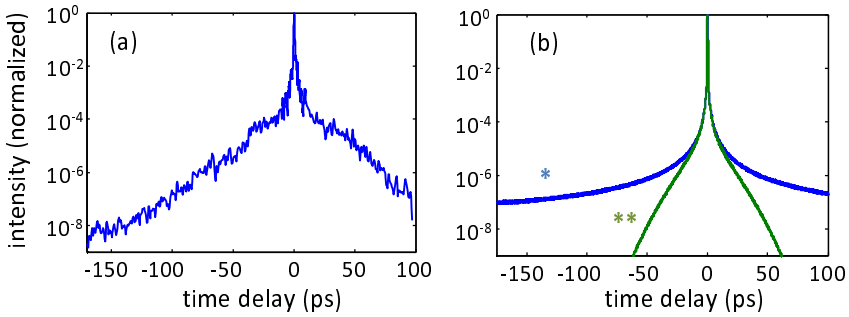

Figure 2.6: (a) Slow rise time of the pulse profile for pulses amplified by OPCPA (Omega-EP, 2005). This was later attributed to pump noise in ref. [107]. (b) Theoretical prediction for the same pulse undergoing spectral clipping happening in the stretcher: * infinitely sharp clipping, ** realistic clipping

2.3 Coherent and semi-coherent effects

The second aspect related to the temporal profile of laser pulses deals with the fidelity of the amplification. The widely used technique of chirped pulse amplification is not exempt of problems and still yields pulses that are not identical to the pulse before amplification. The pulse distortions can be sorted out in two categories: coherent and semi-coherent effects.

2.3.1 Coherent effects

Coherent effects are distortions of the laser pulse, defined as deviation from the bandwidth-limited pulse, happening homogeneously across the beam. Because of that, the spatial and temporal variables describing the electric field are mathematically separable and the temporal pulse distortion can be described by a one-dimensional temporal phase function or alternatively in the spectral domain using the spectral amplitude and phase of the pulse. Such effects include modulations of the spectrum like gain narrowing or spectral clipping in the stretcher and compressor. They can also include spectral phase effects like residual dispersion or non-perfect stretcher/compressor matching. It is possible to control coherent effects either statically or dynamically to a certain extent. Dynamic techniques include the use of spatial light modulators in the Fourier plane of a stretcher where the spectrum can easily be shaped in amplitude and phase or the use of an acousto-optic programmable dispersive filter (AOPDF) [83]. This type of filter associated with a closed-loop pulse measurement device enables some control over the pulse profile. Static techniques include characterization measurements and design optimization. These aspects have been at the centre of my PhD thesis [105, 106].

However, coherent pulse distortions can be seen relatively long before the maximum intensity of the pulse is reached, taking the form of a slow rise in intensity. This is illustrated in fig. 2.6.a that shows the temporal profile of a pulse amplified by OPCPA as example. Here, the slow rise time is a coherent effect induced by an amplitude noise imprinted on the pulse spectrum during amplification. But this slow rise of the intensity can be systematically found in standard CPA lasers. The precise mechanisms leading to this feature are manifold: while some have been studied and reported, new effects have still to be identified, clearly described and mitigation methods must be demonstrated.

Spectral clipping, which is mostly happening in the stretcher, was in the past often presented as a temporal-contrast degradation factor in the literature [108,109], but it has surely been overestimated as we were never able to observe it experimentally. This erroneous idea comes from a straightforward numerical result obtained when a truncated spectrum is Fourier-transformed to infer its pulse shape. Mathematically the result equals the convolution product of the ideal pulse and a cardinal sine function, showing a significant amount of energy away from the pulse maximum, as shown in fig. 2.6.b (blue curve). The simulation shows the third-order autocorrelation signal of a pulse supported by a 4-nm-wide Gaussian spectrum (FWHM) truncated at 8 nm. When the cut is infinitely sharp, wings appear on the pulse (plot *). Such a result is similar to the order of magnitude of the experimental measurement showed for comparison. One can however wonder how valid such a numerical treatment is, as it implies an infinitely sharp cut in the spectrum. A more realistic simulation of the clipping (plot **) including the finite spot size of the beam demonstrates that this effect is probably much smaller in reality. Here the realistic cut is numerically simulated with an error function transition at the location of the cut that takes into account the finite size of the beam on the clipping optical element. A comparison of this profile with the experimentally measured pulse profile in (a) shows that the expected spectral clipping is in general not experimentally observable.

As stated above, the slow rise-time in the pulse profile happening at times between 10 and 100 times the pulse duration is a feature that is currently not fully understood albeit universal in CPA systems. Here the concept of coherent noise is probably the best way to describe this effect that can either come from amplitude noise in the spectrum [107,110] or phase noise arising in the amplifier, stretcher and compressor. In the later references, a strong spectral amplitude noise is reported in an OPCPA where temporal modulations in the pump pulse imprint on the spectrum of the chirped pulse. After pulse compression, a pedestal created by this noise can be seen in the pulse profile as shown in fig. 2.6.a. This result underlines that OPCPA requires a pump laser of very high spectral purity since any phase noise in the pump-pulse spectrum creates temporal noise in the amplified pulse.

In chirped pulse amplifiers, the current assumption is that coherent noise originates from the stretcher (see for instance [111] and references therein). This noise probably forms from spatio-temporal coupling happening at high frequencies directly in the stretcher as shown recently in [112]. This spatio-temporal coupling finds its origin in the surface error of the optics (mirrors and gratings) used in the stretcher. Although spatio-temporal coupling is a semi-coherent effect, for CPA as a whole, it is an inherently coherent effect because the laser amplifier following the stretcher acts as a spatial filter. In particular in the case of a regenerative amplifier, the single spatial mode generated in there only accepts a one-dimensional temporal phase description. Amplitude modulations at high frequencies in the spectrum originating from non properly maintained pulse stretchers have been also reported [113]. Here one should recall that the spectrum of the short pulse is spatially dispersed in the pulse stretcher and that a spatially non-uniform reflectivity of optical elements then translates into spectral amplitude noise.

Coherent noise is actively being studied at the PHELIX facility. There, we made measurements of the pulse profile with high dynamic range at two target stations of the facility using radically different compressor configurations: the first pulse compressor is a double-pass folded compressor using a single gold-coated 1480-l/mm grating, while the second compressor is a single-pass compressor using MLD-coated 1740-l/mm gratings. Both measurements exhibit the same slow rise-time indicating that the compressor has probably very little responsibility in this feature. We have also measured the temporal profile of the pulse for various amplifier configurations and saw little effect, too. From this, we come to the same conclusion that the stretcher is a very likely candidate for the

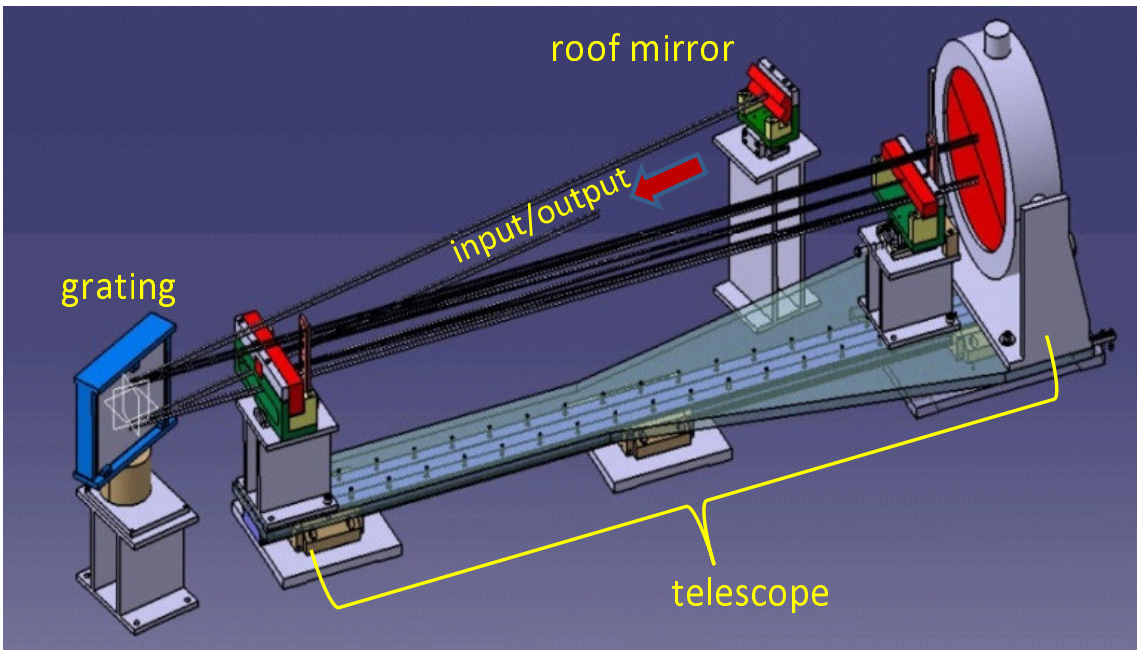

Figure 2.7: Mechanical model of a modified Banks stretcher. The all-reflective-optics telescope is folded to make the whole assembly compact. The input and output beams impact the grating on its lower side, while the spatially dispersed beam hits the grating on the top area. The roof mirror enables double-passing the stretcher.

coherent noise. Stretcher and compressor using similar components like gratings, our hypothesis is that the way the grating or other optics are used in the stretcher is at the base of the problem. A major difference between stretcher and compressor can be found in the beam-to-optics size ratio. While optics and beam have comparable sizes in the compressor that enable surface averaging effects, the beam-to-optics size ratio is much lower than unity, favouring spatial to spectrum noise transfer. Our interpretation is the following: for modern pulse stretchers, based on all-reflective optics as shown in fig. 2.7, a mirror is usually located in the Fourier plane of the stretcher optical assembly (see for instance [114]). This arrangement unfortunately ensures a good mapping of surface roughness noise into spectral noise.

We have validated that the slow rise in a high-power CPA system is a coherent effect by spatially filtering the beam coming out of the stretcher. If spatio-temporal coupling related to the pulse rise time happens in the stretcher, spatial filtering would strongly influence it. Fig. 2.8 shows an autocorrelation trace for a laser with a spatial filter located at the output of the stretcher and without the filter. We could not detect a significant difference between the two measurements, showing that the information on the pulse rising slope is uniformly distributed across the beam. If spatio-temporal effects had been generated in the stretcher, these would have been changed by the spatial filter. In addition, amplifiers especially when based on regenerative amplification act as spatial filters reinforcing our argument.

Another source of temporal noise comes from non-linear effects in chirped-pulse amplifiers, like the temporal Kerr effect, that can turn spectral amplitude noise into spectral phase noise and therefore amplify those perturbations. If a pulse with a modulated spectrum is sent to a chirped pulse amplifier, the spectral modulations are mapped to the time domain after the pulse stretcher and can undergo non-linear phase accumulation during amplification, which creates temporal noise

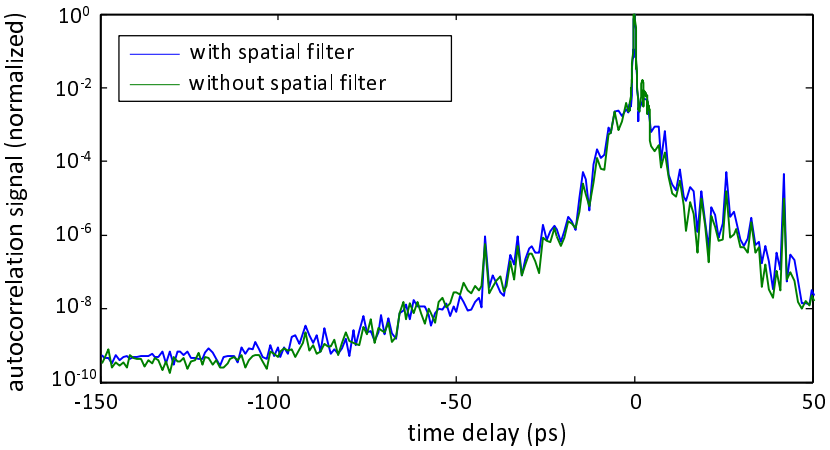

Figure 2.8: Autocorrelation measurement of the CPA system PHELIX when a spatial filter is inserted after the stretcher and when none is used.

after compression. If these modulations happen at high spectral frequencies, their effect can be seen far from the pulse maximum. The main complication is that non-linear effects are only to be seen at maximum power of the laser and are therefore extremely difficult to diagnose during alignment at low power.

2.3.2 Semi-coherent effects

Semi-coherent effects deal with all the effects described above but their amplitude strongly depends on the location across the beam. Mathematically, the associated spectral phase is a function of ω, x and y.

$$\varphi = f(\omega, x, y) \tag{2.9}$$

These effects are intimately linked to a loss of temporal coherence of the pulse. They are in particular extremely hard to correct and once they happen have an irreversible degradation effect of the pulse quality. When the variables in eq. 2.9 are separable, one can probably still think of correction methods but for cases when the variables are not separable any more, the spatial coherence of the beam is degraded and the time-bandwidth product of the pulse is increased.

One first example of such an effect can be found in large high-energy short pulse lasers where the entrance pupil of the laser amplifier is image-relayed throughout the amplifier stages. This type of amplifier enables the efficient use of the amplification section with beams whose spatial profile is super-Gaussian, a non self-similar beam profile that would ultimately have hot spots along its propagation without imaging. The beam transport is done with the help of telescopes based on lenses that can introduce a slight defocus of the beam when the telescope is not perfectly set. Alternatively thermal effects like thermal lensing appear during operation of the amplifiers and can add to the defocus. In such a case, the input direction of individual rays in the beam varies across the aperture, which can be seen as a variation of the input angle into the compressor that changes the compression. In other words, a spherical wavefront into the compressor yields a spatially varying compression factor.

An additional effect can be found for large-aperture laser systems where longitudinal chromatism introduced by telescope yields a colour-dependent input angle into the compressor, yielding again a non spatially uniform compression. Extending this to the more general case, any spatial distortion of the beam leads to poor compression of the pulse, too. In fact, a pulse compressor should be used only with perfectly collimated beams. This is the reason why special care has to be taken of the beam quality in chirped pulse amplifiers. Nowadays, this is done to a certain extent by the introduction of adaptive optics techniques whose aim should be to correct the beam before the compressor.

2.4 Solutions for controlling the temporal contrast of short laser pulses

2.4.1 Methods employed to reduce the amplification noise

As I showed in section 2.2, the reduction of amplification noise falls under the general signal-to-noise problematic and, for laser amplifiers, the theoretically achievable limit is unfortunately not sufficient to prevent pre-ionization of targets with standard CPA lasers. Eq. 2.8 shows also that the temporal pedestal in chirped pulse amplifiers is directly linked to the effective number of photons injected into the amplifier. To improve the temporal contrast, only an increase of this number is possible, which is obtained via an efficient coupling into the amplifiers and the use of energetic seed pulses. This means that an increase of the temporal contrast between 3 and 5 orders of magnitude over standard CPA seed energies is necessary to fulfil the requirements of modern petawatt lasers. And for upcoming systems like the ELI 10-PW laser systems, this requirement increases by another order of magnitude. In other words, temporally-clean laser pulses with energies between 10 µJ and 1 mJ must be created to inject CPA systems.

The typical femtosecond oscillators deliver nanojoule-energy pulses. High-energy oscillators developed with the purpose of generating high-energy short pulses [115] allow for an energy increase of about two orders of magnitude (100 nJ) without compromising the temporal contrast of the laser pulses. A similar result is obtained when a booster laser amplifier located after the oscillator is pumped in continuous or pulsed mode. Higher gains between 100 and 1000 can be obtained in such an arrangement but a cleaning of the pulse is necessary as the amplifier introduces temporal noise (ASE) [116]. Since the pulse is short and the energy still relatively low, saturable absorbers have been used to remove the ASE from the pulse train. However, both devices do not fulfil the requirements of high-intensity systems alone and can only be used in conjunction with an additional contrast-boosting technique like XPW described below.

Figure 2.9: Schematics of a double CPA arrangement

To reach the required seed energy, a first amplifier using the chirped-pulse amplification technique followed by a cleaning stage have been proposed, an arrangement known as double CPA [117]. As depicted in fig. 2.9 where a double CPA has been scaled to present orders of magnitude relevant to a

petawatt-class high-temporal-contrast titanium-doped-sapphire laser system, the first CPA system delivers energies significantly higher than the two previous methods and fulfils the seed energy requirements. However, the pulse amplified in the first stage is noisy and the temporal cleaning of the pulse requires a fast switch. The most successful technique so far is based on third-order non-linear polarization filtering: Cross-Polarized Waves (XPW) [118]. Here the pulse is sent through crossed polarizers and, between the polarizers a non-linear crystal of BaF_2 introduces an intensity-dependent polarization rotation. Because the Kerr effect is instantaneous, the transmission of the cleaning stage follows the intensity of the pulse. The temporal contrast increase is however only as good as the polarization extinction ratio of the polarizer arrangement. Typically, extinction ratios of 3 orders of magnitude can be reached so the XPW cleaning stage does not fully exploit the gain of the first CPA stage. For this reason, XPW is often used in combination with the other methods described above. In addition, the required intensity on the crystal is so high that non-linear effects in air are problematic and the set-up has to be installed in vacuum to avoid short term damage to the crystal. When one stays at intensity levels compatible with long term operation of the XPW stage, the polarization rotation efficiency is moderate at roughly 10 to 15 % of the initial pulse energy. A positive effect of XPW is the presence of a strong self-phase modulation in the non-linear crystal that significantly broadens the spectrum of the pulse compensating for the gain-narrowing occurring in the stage of amplification. Since this advantage is of particular importance for the shortest pulses, XPW is particularly adapted to lasers based on titanium-doped sapphire and is nowadays offered by all major vendors for lasers systems above 100 TW.

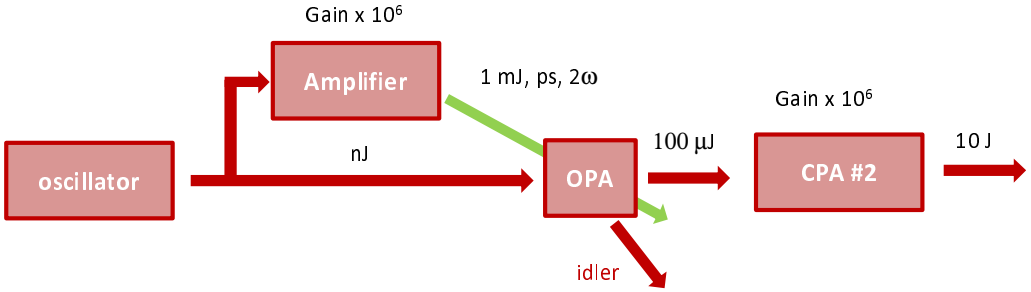

Figure 2.10: Schematics of a CPA laser including an OPA pre-amplifier for contrast boost

The technique of pulse pre-amplification based on the direct parametric amplification of the oscillator pulse has been proposed in Rochester in 2007 [119] as an alternative to XPW. The ultrafast OPA (uOPA) described schematically in fig. 2.10 exploits the instantaneous character of parametric amplification to create a pre-amplifier stage that is inherently free of nanosecond noise. In the uOPA scheme, it is essential that the pump pulse be short and synchronous to the oscillator pulse. Since parametric noise is confined to the duration of the pump pulse, the use of a short pump pulse ensures a pedestal-free amplification. The amplifier uses a non-linear crystal that can achieve very high single-pass gains up to 10^5 over a few millimetres, making the experimental arrangement quite simple. The advantages of the uOPA are manifold: first the amplification is inherently noise-free on a nanosecond time scale so the pulse does not require additional temporal cleaning afterwards. Second, the output energy of the uOPA directly relates to the seed photon number for the main amplifier and therefore characterizes the temporal contrast improvement directly. This is a practical consideration but it is very useful for the long-term stability and robustness of the amplifier. And third, the uOPA scheme is easily scalable to many hundreds of millijoules, keeping headroom for laser systems of even higher peak powers than what is currently available. The main drawback

of uOPA resides in the necessity of a very good synchronization between pump and seed pulses which cannot suffer from jitter or drift.

All in all, the methods described above are only solutions to the amplification noise problematic in CPA lasers systems. They, however, do not address the problem of prepulse, coherent and semi-coherent contrasts.

2.4.2 Improvement of the coherent contrast

As seen in section 2.3.1, the sources of the coherent noise have not been identified with certainty yet. There are cases where noise sources like the spectral purity of the pump pulse in OPCPA have been identified and mitigated [107]. However for CPA lasers, there is no definite answer to the question, although noise originating from the stretcher is the current hypothesis favoured in the community [112]. Here one must recall that an optical pulse stretcher is based on an all-reflective one-to-one imaging telescope. Popular implementations of this idea involve the use of an Öffner triplet [114] or its American pedant, the Banks stretcher [120] (see fig. 2.7). The interest of these designs lies in their compactness compared to the corresponding compressor and previous lens-based in-line stretchers. For these designs, a great care has been taken to minimize third order aberration and chromatism. In all cases, the beam diameter is small on the grating and focuses on an optical element located in the Fourier plane of the telescope. This means that the beam-to-stretch aspect ratio[1] on the grating and Fourier plane mirror is small in many places on the optical path. Local defects at these locations will then map into spectral modulations (phase and amplitude). With current stretchers, beam-to-stretch ratios of the order of 10^{-3} are found in the laboratory. Working under this assumption, a stretcher that would minimize the introduction of coherent noise is a stretcher that has a large beam-to-stretch ratio.

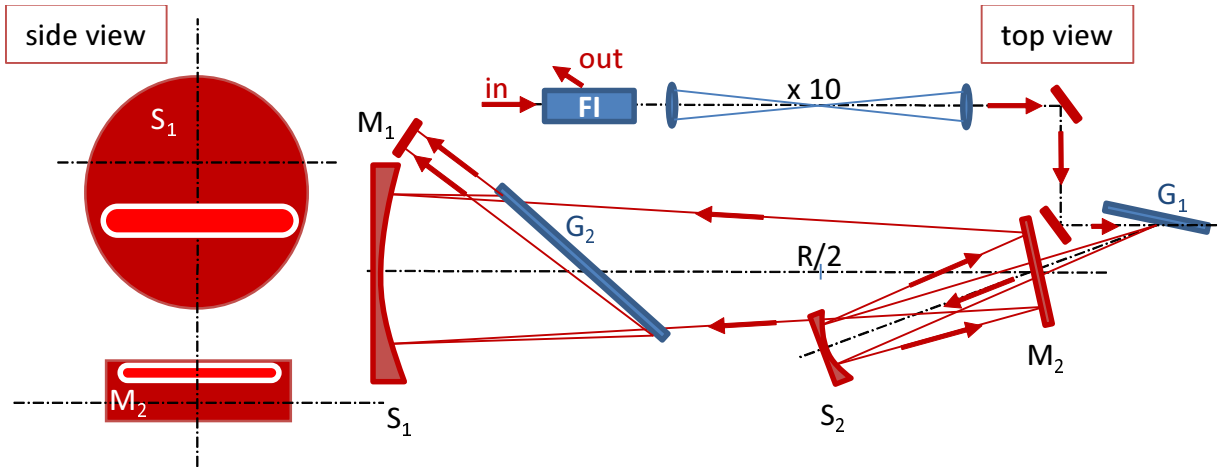

Figure 2.11: Principle of a stretcher working with large beams for enhanced coherent contrast. S_1, S_2: spherical mirrors; FI: faraday isolator; G_1, G_2: gratings, M_1, M_2: folding mirrors. The arrows show the beam propagation direction for the first pass. After the folding mirror M1, the beam comes back on itself.

Fig. 2.11 shows the conceptual schematics of a high-temporal contrast stretcher that could be tested

[1]The beam-to-stretch ratio is the ratio between the diameter of a monochromatic beam and the dimension of the dispersed beam at this location. For practical reasons, the beam-to-stretch ratio is also the optics-to-beam dimension ratio.

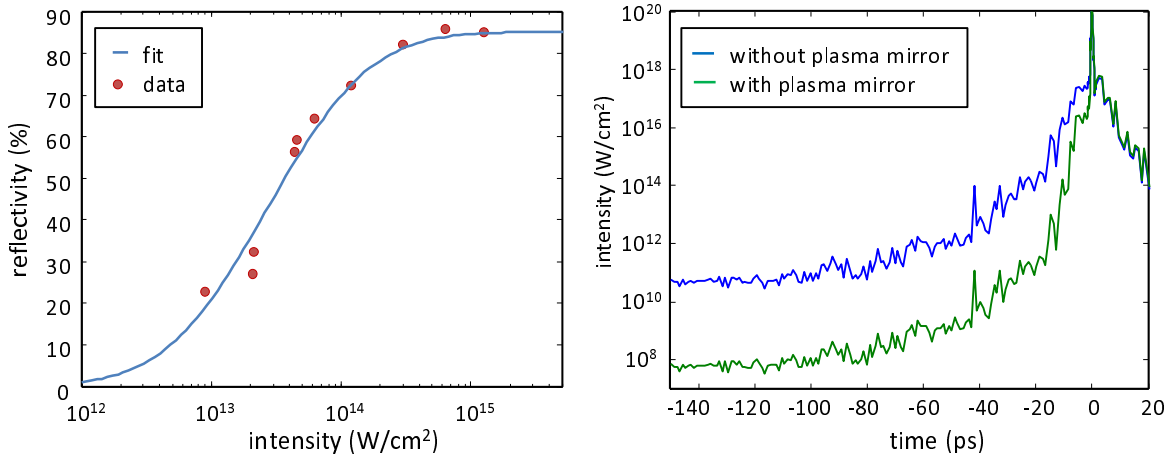

Figure 2.12: typical response of a plasma mirror (left) and calculated effect on the temporal profile (right)

to validate the ideas explained above. This proposed design is not more than an unfolded version of the Banks stretcher which I believe could be used as a test platform for the test of high-coherent-contrast pulse amplification. Here the beam is first magnified in a telescope to a waist size of about 1 cm and then sent to the first grating G_1. The telescope is made of two spherical mirrors S_1 and S_2 of same radius of curvature R. After diffracting on the grating, the beam propagates through the telescope and is intercepted by the second grating G_2. At last a 0-degree mirror M_1 is used to fold the stretcher. The beam is additionally off-centred vertically to enable the configuration without clipping on M_2 and G_2. The imprint of the beam on S_1 and M_2 is shown on the left of the figure. Here one can notice that such a design gives the stretcher a beam-to-stretch ratio of about 0.1, a value 100 times larger than the standard design.

2.4.3 Pulse cleaning after amplification

As described above, the sources of degradation of the temporal fidelity during the amplification are manifold. For this reason, it could be advantageous to employ a fast temporal switch or non-linear filter that can be used to filter out the pulse pedestal after the pulse has been amplified and compressed.

The first proposal to use plasma mirrors as a fast shutter was made nearly 25 years ago [121] and has been in use since then. A plasma mirror is a mirror with an anti-reflective coating that acts as an intensity reduction element as long as the pule intensity stays below a certain threshold. However, as soon as the intensity reaches the damage threshold of the material, the coating is turned into a plasma that starts reflecting light. The characterization of such a mirror is shown in fig. 2.12 (left) that gives measurements made at the PHELIX laser (red dot). The reflectivity of the mirror evolves from the reflectivity of the AR coating (0.1 %) for intensities below $10^{12}\,\mathrm{W/cm^2}$ to 85 % at intensities above $10^{15}\,\mathrm{W/cm^2}$ for an S-polarized beam under 45-degree incidence. A fit function based on an error function (erf) has been used to fit the data. This intensity transfer function can be used to estimate the effect of the plasma mirror on the temporal profile (right plot in fig. 2.12) of a laser capable of reaching $10^{20}\,\mathrm{W/cm^2}$. For this to work, the plasma mirror has to be located in a converging beam, where the peak intensity reaches $10^{15}\,\mathrm{W/cm^2}$, which happens

a few centimetres before the target typically. In such a case, not only can an improvement of the ASE contrast by more than two orders of magnitude be expected, but also one notices a significant steepening of the intensity rise near the peak.

Although the principle of plasma mirrors is relatively straightforward, this imposes a few boundary conditions and has drawbacks. First the plasma mirror should not ignite too early because of a long pulse, or prepulses reaching $10^{12}\,\mathrm{W/cm^2}$ too early before the maximum of the peak. In such a case, the plasma expands away from the substrate with a speed that is intensity dependent and the reflecting surface is not plane any more. In addition, the plasma starts absorbing and the reflectivity drops. A quantification of the effect has been done by Scott et al. on the dynamics of plasma mirrors at PHELIX [122] showing that the plasma mirror has a duration of a few picoseocnds. Second, a plasma mirror can be complicated to implement for high-energy lasers and its costs of operation are not neutral, limiting its use to single-shot types of experiments. Nevertheless, this method is widespread because it is simple, robust and its outcome predictable.

Finally, a second method based on the frequency doubling and rejection of the main frequency has been reported [123]. While the improvement on the pulse contrast cannot be denied, changing the wavelength of the laser has some effects: in particular it increases the penetration depth of the laser into the plasma which in turn increases the absorption. The normalized field potential a_0 is in theory independent of the wavelength (see eq. 1.1), but as the focal spot of many systems is aberration limited, changing the wavelength to the second harmonic reduces a_0 (at constant spot size) accordingly and the conversion efficiency at about 50% reduces this parameter even more. So a careful assessment of the experimental advantages has to be made on an experiment goal basis.

2.5 Peer-reviewed articles on aspects related to the temporal contrast of laser pulses

The articles presented in the following are focusing on various aspects of the temporal contrast of short pulse lasers which has received a growing interest starting in 2000. As many ultrashort-pulse lasers were being commissioned and research focused on the interaction of light with small, often thin targets, it became obvious that the interaction of lasers with matter was strongly affected by the real shape of the laser pulse. The needs for having precise measurement and pulse cleaning techniques was also very strongly debated in the community. In the following, a selection of the contributions to the field.

- V. Bagnoud et al. "High-Dynamic-Range Temporal Measurements of Short Pulses Amplified by OPCPA" Opt. Express **15** (9), 5504–5511 (2007)

  This article was a first contribution to the field and the characterization was done at the university of Rochester in collaboration with colleagues from France. At that time, a debate was taking place on the influence of the OPCPA technique as noise-free amplification technique and a measurement of the temporal contrast of one of the first running setups was decided. It shone new experimental insights on OPCPA backed with a theoretical estimate that led us to conclude that OPCPA is not a noise-free amplification technique. Nevertheless a low noise at the theoretical limit could be observed, which was attributed to the simple experimental implementation of OPCPA that shunts all sources of additional amplification noise.

- D. Javorková and V. Bagnoud, "60-dB-dynamic-range short-pulse measurement from an 8-bit CMOS camera" Opt. Express **15**, 5439-5444 (2007)

One of the aspects of high temporal contrast laser pulses deals with measurement techniques. In particular, there is no satisfactory method that enables single-shot measurement of the temporal contrast of laser pulses on a high dynamic range. In this contribution, we introduce a method to extend the dynamic range of the detection scheme in a second-order autocorrelator to the physical limit of the device. Here, an 8-bit CMOS camera is used as a massively parallel measurement device and noise reduction techniques are used to achieve a noise level lower than 0.1 counts.

- F. Wagner, C. P. João, J. Fils, T. Gottschall, J. Hein, J. Körner, J. Limpert, M. Roth, T. Stöhlker and V. Bagnoud "Temporal contrast control at the PHELIX petawatt laser facility by means of tunable sub-picosecond optical parametric amplification" Appl. Phys. B **116** (2) pp. 429-435 (2014) and,

  F. Wagner, S. Bedacht, A. Ortner, M. Roth, An. Tauschwitz, B. Zielbauer, and V. Bagnoud "Pre-Plasma Formation in Experiments using Petawatt Lasers" Optics Express **22**, Issue 24, pp. 29505-29514 (2014)

  Shortly after the commissioning of the PHELIX facility, it was decided to implement the newly developed concept of ultrafast parametric amplifier in the front end of the PHELIX laser. The demonstration work published by my former colleagues of the University of Rochester was not readily adaptable to a working laser like PHELIX and suffered from shortcomings that we decided to overcome with a technically different implementation. This work was a collaborative effort between GSI, the university of Jena and the higher technological institute of Lisbon. One of the original aspects of the work is the coupled operation of a regenerative laser amplifier with the ultrafast parametric amplifier that enables a full tunability of the temporal background (ASE pedestal) over more than 4 orders of magnitude. In the second article, we related the application of the former feature to the study of the pre-ionization of micrometre-thick targets irradiated by PHELIX.

High-dynamic-range temporal measurements of short pulses amplified by OPCPA

V. Bagnoud

Gesellschaft für Schwerionenforschung mbH, Planckstrasse 1, 64291 Darmstadt, Germany
v.bagnoud@gsi.de

J. D. Zuegel

Laboratory for Laser Energetics, University of Rochester, 250 East River Road, Rochester NY 14623, USA

N. Forget and C. Le Blanc

Laboratoire pour l'Utilisation des Laser Intenses (LULI), Unité Mixte n°7605 CNRS – CEA – Ecole Polytechnique-Université Pierre et Marie Curie, Ecole Polytechnique, 91128 Palaiseau, France

Abstract: We report on the first experimental measurement of high-dynamic-range pulse contrast of compressed optical parametric chirped-pulse-amplification (OPCPA) pulses on the picosecond scale. The measured –80-dB OPCPA contrast at 1054 nm agrees well with theoretical predictions and exceeds the estimated and measured levels for comparable amplification in a Ti:sapphire regenerative amplifier by approximately 10 dB. A key to achieving better contrast with OPCPA is the simpler experimental setup that promotes more-efficient coupling of seed pulse energy into the amplification system.

OCIS codes: 140.7090 (Ultrafast lasers), 190.4970 (Parametric oscillators and amplifiers), 320.7100 (Ultrafast measurements), 320.5520 (Pulse compression).

References and links

1. D. Umstadter, "Review of physics and applications of relativistic plasmas driven by ultra-intense lasers," Phys. Plasmas **8**, 1774–1785 (2001).
2. D. Strickland and G. Mourou, "Compression of amplified chirped optical pulses," Opt. Commun. **55**, 447–449 (1985).
3. G. N. Gibson, R. Klank, F. Gibson, and B. E. Bouma, "Electro-optically cavity-dumped ultrashort-pulse Ti:Sapphire oscillator," Opt. Lett. **21**, 1055–1057 (1996).
4. A. Fernandez, T. Fuji, A. Poppe, A. Fürbach, F. Krausz, and A. Apolonski, "Chirped-pulse oscillators: A route to high-power femtosecond pulses without external amplification," Opt. Lett. **29**, 1366–1368 (2004).
5. J. Itatani, J. Faure, M. Nantel, G. Mourou, and S. Watanabe, "Suppression of the amplified spontaneous emission in chirped-pulse-amplification lasers by clean high-energy seed-pulse injection," Opt. Commun. **148**, 70–74 (1998).
6. A. Jullien, F. Augé-Rochereau, G. Chériaux, J.-P. Chambaret, P. d'Oliveria, T. Auguste, and F. Falcoz, "High-efficiency, simple setup for pulse cleaning at the millijoule level by nonlinear induced birefringence," Opt. Lett. **29**, 2184–2186 (2004).
7. M. Nantel, J. Itatani, A.-C. Tien, J. Faure, D. Kaplan, M. Bouvier, T. Buma, P. Van Rompay, J. A. Nees, P. P. Pronko, D. Umstadter, and G. A. Mourou, "Temporal contrast in Ti:Sapphire lasers: Characterization and control," IEEE J. Sel. Top. Quantum Electron. **4**, 449–458 (1998).
8. A. Jullien, O. Albert, F. Burgy, G. Hamoniaux, J.-P. Rousseau, J.-P. Chambarét, F. Augé-Rochereau, G. Cheriaux, J. Etchepare, N. Minkovski, and S. M. Saltiel, "10^{-10} temporal contrast for femtosecond ultraintense lasers by cross-polarized wave generation," Opt. Lett. **30**, 920-922 (2006).
9. M. P. Kalashnikov, E. Risse, H. Schönnagel, and W. Sander, "Double chirped-pulse-amplification laser: A way to clean pulses temporally," Opt. Lett. **30**, 923–925 (2005).
10. A. Dubietis, G. Jonusauskas, and A. Piskarskas, "Powerful femtosecond pulse generation by chirped and stretched pulse parametric amplification in BBO crystal," Opt. Commun. **88**, 437–440 (1992).
11. L. J. Waxer, V. Bagnoud, I. A. Begishev, M. J. Guardalben, J. Puth, and J. D. Zuegel, "High-conversion-efficiency optical parametric chirped-pulse amplification system using spatiotemporally shaped pump pulses," Opt. Lett. **28**, 1245–1247 (2003).

#77130 - $15.00 USD Received 15 Nov 2006; revised 21 Feb 2007; accepted 2 Mar 2007; published 20 Apr 2007

12. I. N. Ross, P. Matousek, M. Towrie, A. J. Langley, and J. L. Collier, "The prospects for ultrashort pulse duration and ultrahigh intensity using optical parametric chirped pulse amplifiers," Opt. Commun. **144**, 125–133 (1997).
13. V. V. Ivanov, A. Maksimchuk, and G. Mourou, "Amplified spontaneous emission in a Ti:Sapphire regenerative amplifier," Appl. Opt. **42**, 7231–7234 (2003).
14. H. Yoshida, E. Ishii, R. Kodama, H. Fujita, Y. Kitagawa, Y. Izawa, and T. Yamanaka, "High-power and high-contrast optical parametric chirped pulse amplification by β-BaB_2O_4 crystal," Opt. Lett. **28**, 257–259 (2003).
15. V. Bagnoud, I. A. Begishev, M. J. Guardalben, J. Puth, and J. D. Zuegel, "5-hz, >250-mJ optical parametric chirped-pulse amplifier at 1053 nm," Opt. Lett. **30**, 1843–1845 (2005).
16. J. Zou, D. Descamps, P. Audebert, S. D. Baton, J. L. Paillard, D. Pesme, A. Michard, A. M. Suautivet, H. Timsit, and A. Migus, "LULI 100-TW Ti:Sapphire/Nd:Glass laser: A first step toward a high-performance petawatt facility," in *Third International Conference on Solid State Lasers for Application to Inertial Confinement Fusion*, H. Lowdermilk, ed. (SPIE, Bellingham, WA, 1999), Vol. 3492, pp. 94–97.
17. A. Yariv, *Quantum electronics*, 3rd ed. (Wiley, New York, 1989).
18. G. Chériaux, P. Rousseau, F. Salin, J. P. Chambaret, B. Walker, and L. F. Dimauro, "Aberration-free stretcher design for ultrashort-pulse amplification," Opt. Lett. **21**, 414–416 (1996).
19. V. Bagnoud, M. J. Guardalben, J. Puth, J. D. Zuegel, T. Mooney, and P. Dumas, "High-energy, high-average-power laser with Nd:YLF rods corrected by magnetorheological finishing," Appl. Opt. **44**, 282–288 (2005).
20. I. D. Jung, F. X. Kaertner, J. Henkmann, G. Zhang, and U. Keller, "High-dynamic-range characterization of ultrashort pulses," Appl. Phys. B **B65**, 307–310 (1997).
21. N. Forget, A. Cotel, E. Brambrink, P. Audebert, C. Le Blanc, A. Jullien, O. Albert, and G. Chériaux, "Pump-noise transfer in optical parametric chirped-pulse amplification," Opt. Lett. **30**, 2921–2923 (2005).

1. Introduction

Temporal pulse contrast is of foremost importance in high-intensity plasma-physics experiments where poor temporal contrast caused by prepulses and background pedestals can change the physical properties of targets before the arrival of the main laser pulse [1]. High-energy, ultrashort laser pulses are typically generated in a mode-locked oscillator followed by chirped-pulse amplification (CPA) [2]. The temporal contrast level typically associated with this technique is driven mainly by the amplifier noise or amplified spontaneous emission (ASE), resulting in a background intensity about 50 to 70 dB below that of the main pulse. When the laser is used to reach on-target intensities greater than 10^{18} W/cm^2, the intensity background is high enough, on a long-enough scale, to change the target's physical properties before the short pulse reaches it.

Two general approaches have been demonstrated to improve compressed pulse contrast: first, increasing the CPA amplifier seed improves the signal-to-noise ratio [3–5] and, second, nonlinear effects [6–9] can "clean" the short pulse from its pedestal after the pulse is temporally compressed. Both approaches add complexity to the system by adding one or more contrast improvement stages.

Optical parametric chirped-pulse amplification (OPCPA) [10] was proposed as a preamplification technique for the front end of large, petawatt-class Nd:glass laser systems because of its manifold advantages [11]. In OPCPA, optical parametric generation (OPG) plays a role analogous to ASE in laser amplification. Since OPCPA involves an instantaneous transfer of power from a pump pulse to the amplified signal pulse, OPG is generated only during the pump–pulse duration. Lower prepulse energy can be achieved for target experiments with OPCPA, given that OPCPA pump pulses are only a few nanoseconds or less. Theoretical predictions that OPCPA should achieve higher contrasts [12] than laser amplification have been controversial [13], although a measured OPCPA contrast of 78 dB for nanosecond time scales has been reported [14].

In this paper, we report on the experimental characterization of the picosecond-scale temporal contrast of an OPCPA system operating at 1054 nm [15]. In Sec. 2, we theoretically estimate the temporal contrast for an OPCPA system based on lithium triborate (LBO) as well as a Ti:sapphire regenerative amplifier. In Sec. 3, we describe the experimental setup for measuring the contrast of a compressed pulse amplified by OPCPA and, in Sec. 4, present the

#77130 - $15.00 USD Received 15 Nov 2006; revised 21 Feb 2007; accepted 2 Mar 2007; published 20 Apr 2007

first direct measurement of high-dynamic-range temporal contrast of a 20-mJ pulse amplified using OPCPA. In Sec. 5, we compare our OPCPA results to the reported temporal contrast of a Ti:sapphire regenerative amplifier [16] and also compare the contrast limitations of each system.

2. Theoretical contrast of parametric and regenerative amplifiers

The level of parametric fluorescence in an optical parametric amplifier can be evaluated by assuming one photon of noise per mode and per time unit at the input of the amplifier and summing all amplified contributions over the relevant spectral and angular windows [17]. To calculate the contrast, only the OPG that filters through the OPCPA system should be considered. This corresponds to the OPG emitted "on axis" with a spectrum included in the spectral bandwidth of the system. In such conditions, the OPG intensity emitted through the system is given by

$$I_{\mathrm{OPG}} = \frac{1}{2}\frac{n_c c}{\nu_c \lambda_c^2}\Delta\omega_{\mathrm{sys}}\Delta\theta_{\mathrm{sys}}^2 \sinh^2 \gamma L, \tag{1}$$

where $\Delta\omega_{\mathrm{sys}}$ is the spectral bandwidth of the system, $\Delta\theta_{\mathrm{sys}}$ is the divergence half-angle, and n_c, ν_c, and λ_c are the index, group velocity, and wavelength of the fluorescence complementary wave, respectively. Equation (1) is valid only for the unsaturated amplification case, which provides a lower limit when significant pump depletion occurs. In addition, it is assumed that OPG emission is uniform across the considered spatial and spectral windows, which can be verified in Fig. 1, which shows the OPG power as a function of the wavelength and interaction angle for an LBO crystal cut for slightly noncollinear interaction. The yellow square represents the projection of the system's angular and spectral windows and is included in an area of uniform OPG power.

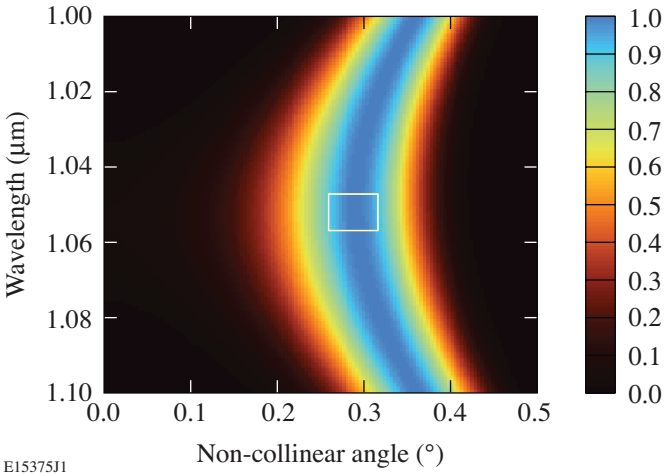

Fig. 1. Calculated relative OPG power of an LBO as a function of the internal noncollinear emission angle and emission wavelength. The yellow square represents the spectral and angular acceptance of the laser system.

The solid angle of the system accepts as a lower limit the divergence of the amplified beam ($\Delta\theta_{\mathrm{sys}} \sim \lambda/\omega_0$), but this limit is not easily reached for practical reasons. The spectrum of the OPG filtered by the system (laser amplifier, compressor) is more or less naturally matched to the amplified pulse spectrum [$\Delta\lambda_s \sim \lambda^2/(\Delta t_s \pi c)$], so, in the following, we assume $\Delta\lambda_s = \Delta\lambda_{\mathrm{sys}}$. For a nearly degenerate configuration, a spectral width that is small compared to the

#77130 - $15.00 USD Received 15 Nov 2006; revised 21 Feb 2007; accepted 2 Mar 2007; published 20 Apr 2007

wavelength and a system bandwidth that matches the OPCPA spectral width, Eq. (1) can be approximated as

$$I_{\mathrm{OPG}} = \frac{1}{\lambda^2}\Delta\omega_s\Delta\theta_{\mathrm{sys}}^2 \sinh^2 \gamma L. \tag{2}$$

To compare the OPG level to the signal level in terms of measurable input quantities, it is convenient to express the fluxes of OPG and signal photons. Assuming a pump pulse with a top-hat profile both in space and time, with area *S*, the equivalent flux of OPG photons emitted on axis is given by

$$\Phi_{\mathrm{OPG}} = \frac{1}{\lambda^2}\Delta\omega_s\Delta\theta_{\mathrm{sys}}^2 S \sinh^2 \gamma L. \tag{3}$$

When spectral gain variations can be neglected, the flux of amplified and compressed OPCPA signal photons is given by

$$\Phi_{\mathrm{signal}} = \frac{E_s}{\hbar\omega_s\Delta t_s}\sinh^2 \gamma L, \tag{4}$$

where E_s is injected signal energy, Δt_s is the ultimate pulse duration, and ω_s is signal pulsation. Assuming perfect spatial and temporal overlap of the amplified OPCPA signal and OPG fluxes, the pulse contrast is then given by

$$C = \frac{\Phi_{\mathrm{OPG}}}{\Phi_s} \approx \frac{\hbar\omega_s}{E_s}\frac{S\Delta\theta_{\mathrm{sys}}^2}{2\lambda^2}\left(\Delta\omega_s \cdot \Delta t_s\right). \tag{5}$$

This formulation of the pulse contrast can be understood as the product of three terms: the inverse of the number of injected photons, a term that characterizes the spatial discrimination between signal and OPG, and the time–bandwidth product of the recompressed pulse. Since Fourier-transform-limited pulses and good optical beam quality have been demonstrated with this OPCPA system [11], the theoretical limit for OPCPA pulse contrast is given by the number of injected photons.

In the case of an OPCPA injected with 0.6-nJ pulses, an OPCPA beam cross section of 3.4 mm^2, a 1054-nm central wavelength compressed to 400 fs, and a compressor bandwidth of 10 nm, the contrast of a beam of 1-mrad divergence equals 82 dB when Eq. (5) is used.

The ASE from a regenerative amplifier also originates from the same quantum noise (one photon per mode), and its power can be found in Eq. (3) of Ref. 13. The contrast can then be calculated from this formula and expressed in a form similar to Eq. (5)

$$C = \frac{1}{8\pi}\frac{\hbar\omega_s}{E_s}\frac{S}{\omega_{\mathrm{bd}}}\frac{\Omega}{\tau\sigma}\left(\Delta\omega_s \cdot \Delta t_s\right) \tag{6}$$

where $\Delta\omega$ is the spectral bandwidth of the regenerative amplifier, ω_{bd} is the effective bandwidth of the fluorescence spectrum (~200 nm), $\hbar\omega_s$ is the signal photon energy, σ is the stimulated emission cross section, τ is the lifetime of the metastable level, *S* is the area of the beam in the laser gain medium, and Ω is the small solid angle in which fluorescence is collected. E_s and Δt_s stand for the energy and time duration of the injected pulse. For a TEM_{00} mode, the product of the beam area by the divergence of the beam is $S\Omega = \lambda^2/n^2$:

$$C = \frac{\hbar\omega_s}{E_s}\frac{\lambda^2}{8\pi n^2\omega_{\mathrm{bd}}\tau\sigma}\left(\Delta\omega_s \cdot \Delta t_s\right). \tag{7}$$

#77130 - $15.00 USD Received 15 Nov 2006; revised 21 Feb 2007; accepted 2 Mar 2007; published 20 Apr 2007

Equations (5) and (7) both show a dependency on the number of injected photons; however, with OPCPA, this number is close to the available seed photons, while injection into a regenerative amplifier depends on many parameters and cannot easily be optimized. For the numerical application, the bandwidth of the Ti:sapphire regenerative amplifier operating at 1057 nm considered in Sec. 5 is 7 nm and limited by the transmission of the intracavity polarizer. The effective excited state lifetime τ is 2.8 μs. Despite careful mode matching, the fraction of energy effectively coupled to the Gaussian TEM00 mode of the cavity within the bandwidth of the regenerative cavity is estimated to be 20%, at best; therefore, the seed energy E_s does not exceed 80 pJ. With these parameters, the expected contrast for the regenerative amplifier is 74 dB.

3. Experimental setup

Figure 2 shows a schematic of the experimental setup, but a more detailed description of the OPCPA system can be found in Ref. 11. A Nd:glass mode-locked oscillator (GLX-200, Time-Bandwidth Product) generates 220-fs, 1.7-nJ pulses at a repetition rate of 76 MHz and a wavelength of 1053 nm. The short pulses are temporally stretched in an Öffner triplet stretcher [18] by a stretch ratio of 300 ps/nm. The stretcher offers a spectral bandwidth slightly greater than 8-nm FWHM with an energy transmission efficiency of approximately 40%. The stretched 2.4-ns pulse is then sent to the OPA stage for amplification, which is the two-crystal preamplifier described in Ref. 15.

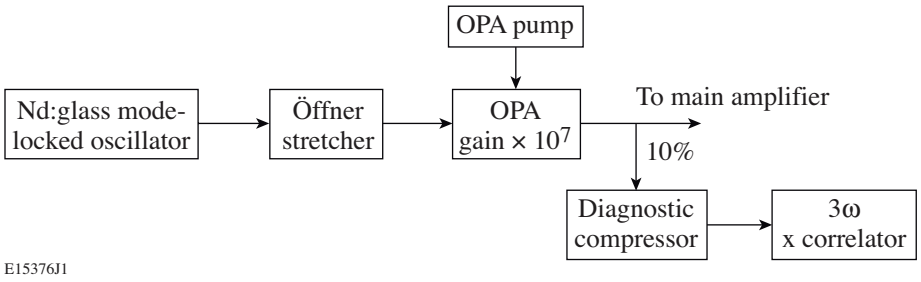

Fig. 2. Experimental setup of the OMEGA EP front-end prototype.

The seed beam is up-collimated to 2 mm (FWHM) to create a good overlap between the pump beam and the seed beam in the OPCPA crystal. Because of the instantaneous nature of parametric amplification, we use a 2.5-ns-long, top hat pump laser [19], running at 5 Hz, to provide a uniform gain across the pumped area in space and time, allowing for high conversion efficiency, without spatiotemporal effects. The amplifier uses two 29.75-mm-long lithium triborate (LBO) crystals in a walk-off compensated configuration and cut for nearly collinear, degenerate interaction. The pump beam is 2.2 mm in diameter, and its energy can be tuned to reach saturation of the parametric process, typically with 100-mJ pump pulses, at a pump laser intensity of 1 GW/cm^2. With this amplifier, the measured gain exceeds 10^3 per crystal, and the output energy, after the two crystals, is greater than 20 mJ, leading to an overall gain of 3×10^7. The pump and seed beams are slightly noncollinear to allow for separation of the idler and signal beams. At nominal pumping power, the energy balance of the system defined at the sum of the idler, signal, and transmitted pump energy equals 90% of the input pump energy, indicating that 10% of the energy is either absorbed, reflected, or dissipated in form of OPG in the nonlinear crystals.

After amplification to 20 mJ, about 10% of the energy is sent through a diagnostic compressor. The 2-mJ pulse compresses to within 7% of the theoretical limit in the folded two-grating compressor, and the high-dynamic-range temporal profile shown in Fig. 2 is measured using a third-harmonic cross-correlator (Sequoia, Amplitude Technologies). The 10-mm-wide beam is not imaged throughout the compressor and undergoes an ~8-m

#77130 - $15.00 USD Received 15 Nov 2006; revised 21 Feb 2007; accepted 2 Mar 2007; published 20 Apr 2007

free-space propagation before entering the cross correlator. The beam is not focused into the correlator crystal, and we can suppose that the entire beam participates in the measurement (no aperturing occurs).

The cross-correlation trace presented in Fig. 3 shows typical experimental data. The noise level of the cross correlator is assessed by blocking each of the arms of the apparatus during a scan. When the 2ω channel is blocked, as shown in Fig. 2, the noise level of –87 dB is higher than when the 1ω arm is blocked or when the input beam is totally blocked. In that case, the noise level drops to –110 dB, which is the detection noise floor. The noise floor of the cross correlator is apparently limited by self-third-harmonic generation of the 1ω arm due to scattering of the beam to a dynamic range of –87 dB.

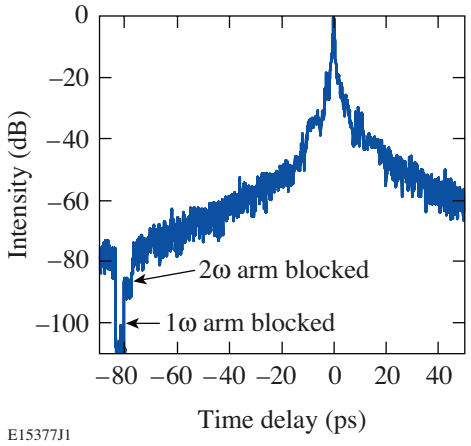

Fig. 3. 3ω cross-correlation trace recorded after the diagnostic compressor. On the measurement trace, the dips show the instrument noise floor, when the 1ω and 2ω arms of the cross correlator are blocked.

4. High-dynamic-range OPCPA contrast measurements and analysis

Four distinct regions of contrast can be identified in the compressed OPCPA pulse temporal profile shown in Fig. 3: a transform-limited pulse, a pedestal divided into two regions with different slopes, and a constant pedestal for delays greater than approximately 100 ps before the main pulse. The Fourier-transform-limited, 400-fs pulse is characterized by a contrast of –27 dB, and a slight asymmetry of the pulse is observed. A slower decrease of the pulse intensity is observed in the region between 2 ps and 25 ps before the pulse with a slope of 10 dB per 15 ps, while the pulse intensity decreases even slower with a slope of 10 dB per 25 ps in the range of –25 ps to –100 ps. At this point, the temporal contrast reaches a steady value around an average of –79 dB up to the maximum range of the measurement window at –170 ps.

The mode-locked seed oscillator contributes to part of the slow-rise-time pedestal. The seed pulses were characterized using a scanning, noncollinear, second-order autocorrelator with a maximum dynamic range of ~60 dB, which is mostly limited by scattering effects in the frequency-doubling crystal. The result of the autocorrelation trace is superimposed on the OPCPA cross-correlation trace in Fig. 4(b). These two plots were not recorded simultaneously, but they both exhibit a pedestal with a similar slope between +20 ps and –20 ps, although the pedestal levels are different. We later found that the oscillator pulse pedestal is present when the oscillator spectrum is tuned toward 1053 nm to match the central wavelength of LHG8 Nd:glass, as required for injection of a petawatt-class laser. When the oscillator central wavelength is allowed to shift to 1055 nm and above, we experimentally verified that this pedestal disappears. Moreover, when monitored over time, the level of the

#77130 - $15.00 USD Received 15 Nov 2006; revised 21 Feb 2007; accepted 2 Mar 2007; published 20 Apr 2007

pedestal varied during the day. This shows that part of the pedestal seen in the OPCPA output pulse is likely to have been present before amplification and should not be attributed to an effect arising during the parametric amplification. This slow rise time of the temporal intensity of pulses produced by a mode-locked oscillator using a SESAM has been reported before [20] and corroborates our observations.

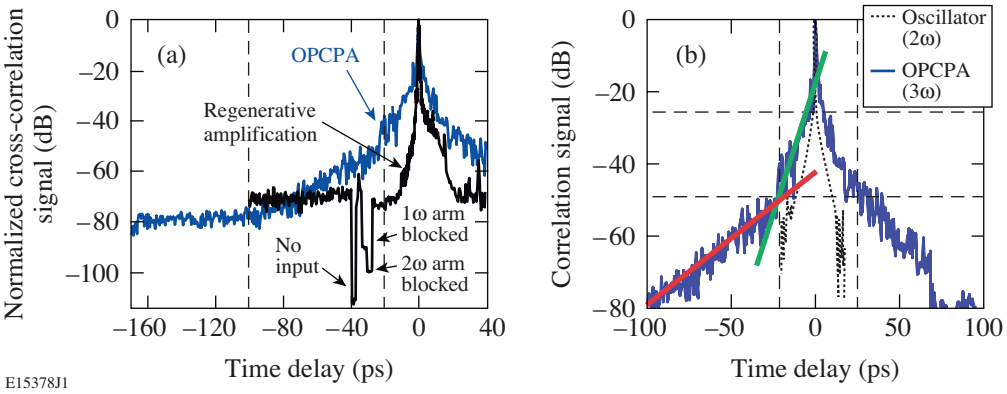

Fig. 4. (a) Third-order cross correlations show the measured maximum contrast of –79 dB for a compressed OPCPA pulse for times greater than ~100 ps before the main compressed pulse. For comparison, the maximum contrast measured for a comparable Ti:sapphire regenerative amplifier [16] with the same instrument is –70 dB. (b) A higher-resolution cross-correlation signal of the OPCPA pulses (blue line) shows three additional regions of contrast. The contrast of the transform-limited pulse is limited to –27 dB, while two additional pedestal regions are observed with different slopes. The slope (10 dB per 15 ps) of a second-order autocorrelation signal of the mode-locked oscillator (black dots) is consistent with the first observed pedestal, which indicates it might be limited by the performance of the seed pulse.

The –100-ps to –25-ps region of the slow-rise-time pedestal, before the pulse, is consistent with OPCPA contrast degradation resulting from temporal noise on the OPCPA pump pulse [21]. This high-frequency temporal noise is transferred to the OPCPA spectrum of the chirped pulse, which causes poor recompression on a picosecond time scale. Further investigation is required to fully evaluate and confirm this contrast degradation mechanism.

The level of the background signal was monitored daily over one week and, again, one month later and showed a constant value. No specific spatial filtering was applied to the OPCPA beam, nor was it image relayed to the correlator. However, when the beam was apertured in the compressor, we saw a decrease of the measured noise floor to values between –86 dB and –89 dB. As this is very close to the detection limit of the apparatus, the data are not quantitatively reliable. However, this would tend to verify that by reducing the second term in Eq. (5), which is the allowed propagation solid angle, one can improve the contrast.

5. Comparison with regenerative amplification

A direct comparison of contrast achieved with equivalent OPCPA and regenerative amplification performance highlights several of the advantages of OPCPA. The LULI 100-TW laser front end uses a regenerative amplifier that performs similarly to our OPCPA setup. In this setup, a commercial Ti:sapphire mode-locked oscillator (Tsunami, Spectra-Physics) delivers 100-fs (FWHM) pulses at 1057-nm pulses with a bandwidth of 12 nm at a repetition rate of 82 MHz. Pulses are stretched in an Öffner triplet stretcher to 1 ns. The energy of the stretched pulses is 0.5 nJ, which is practically identical to the OPCPA seed injection level described in Sec. 4. Selected pulses are injected into a Ti:sapphire regenerative amplifier pumped by a frequency-doubled Nd:YAG laser (SureLite, Continuum) and amplified to 2 mJ with a 10-Hz repetition rate. Gain narrowing reduces the bandwidth of the amplified pulses to 5 nm. A pair of gratings is used to recompress the pulse to 350 fs and characterized using the same high-dynamic-range cross-correlator, as shown in Fig. 4(a). The

#77130 - $15.00 USD Received 15 Nov 2006; revised 21 Feb 2007; accepted 2 Mar 2007; published 20 Apr 2007

temporal contrast behavior for regenerative amplification differs significantly from that measured for the OPCPA system. A pulse pedestal extending ~20 ps before and after the peak of the compressed regenerative amplifier pulses is attributed to residual spectral phase. This pedestal drops to a steady contrast level of –70 dB, which agrees well with the theoretical estimate for ASE discussed in Sec. 2. Although the cross-correlator measurement is limited to ~100 ps before the pulse, this ASE pedestal is expected to extend over several nanoseconds corresponding to the pump laser pulse length.

The measured background ASE level for the regenerative amplifier is 10 dB higher than the OPG-limited background measured for the OPCPA system, which agrees well with the theoretical predictions and shows that pulse contrast is primarily differentiated by the efficiency of coupling seed energy into the amplification system. Given the simpler experimental setup, achieving high contrast is more straightforward with OPCPA than regenerative amplification because cavity mode-matching is more stringent than simple spatial and temporal pulse-overlapping.

6. Conclusion

We report the first high-dynamic-range temporal measurements of an optical pulse amplified by OPCPA on a picosecond time scale and compare them with results obtained for with regenerative amplification. Our results show a –79-dB noise floor for OPCPA that is limited by OPG and is in good agreement with theoretical estimates, but an approximately 100-ps temporal pedestal was observed that is consistent with measurements reported in Ref. 21. On a nanosecond scale, OPCPA offers approximately 10-dB-better contrast than classical regenerative amplification, primarily due to better coupling of seed pulses into the amplification system.

Some solutions should be tested to improve the contrast of pulses amplified by OPCPA. First, the use of an OPCPA preamplifier stage, strongly spatially filtered, should improve the contrast as close to the theoretical limit as possible, and, second, the use of high-energy seed lasers, as was recently demonstrated, would improve the signal-to-noise ratio by 20 dB. With these two steps, it should be possible to improve the contrast of pulses amplified by OPCPA to –110 dB or –120 dB.

Acknowledgments

This work was supported by the U.S. Department of Energy Office of Inertial Confinement Fusion under Cooperative Agreement No. DE-FC52-92SF19460, the University of Rochester, and the New York State Energy Research and Development Authority. The support of DOE does not constitute an endorsement by DOE of the views expressed in this article.

#77130 - $15.00 USD Received 15 Nov 2006; revised 21 Feb 2007; accepted 2 Mar 2007; published 20 Apr 2007

60-dB-dynamic-range short-pulse measurement from an 8-bit CMOS camera

D. Javorková[1, 2], and V. Bagnoud[1]

[1]*PHELIX project, Gesellschaft fur Schwerionenforschung, Planckstrasse 1, 64291 Darmstadt, Germany*
[2]*Department of Experimental Physics, Faculty of Mathematics, Physics and Informatics Comenius University, Mlynská dolina, 84248 Bratislava, Slovakia*
d.javorkova@gsi.de, v.bagnoud@gsi.de

Abstract: We have developed a simple detection scheme that uses an 8-bit CMOS camera and spans over 60-dB dynamic range. By use of noise reduction techniques, the 8-bit CMOS camera yields a 40-dB dynamic-range signal, which is further increased by 20 dB by making a replica of the signal beam on another part of the detector chip. We have experimentally validated this scheme in a scanning and a single-shot autocorrelator.

OCIS codes: (230.4320) Nonlinear optical devices; (320.7100) Ultrafast measurements; (140.7090) Ultrafast lasers; (190.1900) Diagnostic applications of nonlinear optics; (040.1490) Cameras

References and links

1. M. D. Perry, et al., "Petawatt laser pulses," Opt. Lett. **24**, 160-162 (1999).
2. J. D. Zuegel, et al., "Laser challenges for fast ignition," Fusion Sci. Technol. **49**, 453-482 (2006).
3. D. Strickland and G. Mourou, "Compression of amplified chirped optical pulses," Opt. Commun. **56**, 219-221 (1985).
4. D. Umstadter, "Review of physics and applications of relativistic plasmas driven by ultra-intense lasers," Phys. Plasmas **8**, 1774-1785 (2001).
5. P. A. Norreys et al., "PW lasers: matter in extreme laser fields," Plasma Phys. Controlled Fusion **46**, 13-21 (2004)
6. C. Iaconis and I. A. Walmsley, "Spectral phase interferometry for direct electric-field reconstruction of ultra-short optical pulses," Opt. Lett. **23**, 792-794 (1998).
7. D. J. Kane and R. Trebino, "Single-shot measurement of the intensity and phase of an arbitrary ultra-short pulse by using frequency-resolved optical gating," Opt. Lett. **18,** 823-825 (1993).
8. F. Salin et al., "Single-shot measurement of a 52-fs pulse," Appl. Opt. **26**, 4528-4531 (1987).
9. A. Brun et al., "Single-shot characterization of ultra-short light pulses," J. Phys. D: Appl. Phys. **24**, 1225-1233 (1991).
10. M. Raghuramaiah et al., "A second-order autocorrelator for single-shot measurement of femtosecond laser pulse durations," Sadhana **26**, 603–611 (2001).
11. N. Forget et al., "Pump-noise transfer in optical parametric chirped-pulse amplification," Opt. Lett. **30,** 2921-2923 (2005).
12. O. Konoplev et al., "Ultrahigh dynamic range measurement of high-contrast pulse using second-order autocorrelator," LLE Review **75**, 159-170 (1998), http://www.lle.rochester.edu/03_publications/03_01_review/pastreviews/lle-review-75.html
13. A. Braun, et al., "Characterization of short-pulse oscillators by means of a high-dynamic-range autocorrelation measurement," Opt. Lett. **20**, 1889-1891 (1995).
14. P. F. Curley, et al., "High dynamic range autocorrelation studies of a femtosecond Ti:sapphire oscillator and its relevance to the optimisation of chirped pulse amplification systems," Opt. Commun. **120**, 71-77 (1995).
15. E. J. Divall and I. N. Ross, "High dynamic range contrast measurements by use of an optical parametric amplifier correlator," Opt. Lett. **29**, 2273-2275 (2004).
16. A. Hoffman, et al., "CMOS Detector Technology," Exp. Astron. **19,** 111-134 (2005)
17. L. Sarger and J. Oberle, *How to measure the characteristics of laser pulses in Femtosecond Laser Pulses*, C. Rulliere, ed., (Springer-Verlag, New York, 2004).

#79388 - $15.00 USD Received 24 Jan 2007; accepted 23 Mar 2007; published 20 Apr 2007

1. Introduction

The development of modern high-energy petawatt laser systems around the world [1, 2] is made possible by applying the chirped-pulse-amplification (CPA) technique [3] to systems with a large number of amplification stages. After the last stage of amplification, the stretched pulse is usually compressed to sub-picosecond durations before being sent to the experimental area. The adjustment of a compressor with meter-size optics requires an efficient and versatile temporal diagnostic that should be able to work in single-shot mode and at low energy during the alignment of the compressor. Indeed, two temporal parameters are important during the compressor adjustment: the pulse duration which is directly related to the achievable on-target peak intensity and the pulse pedestal. In particular the pulse pedestal has received a growing interest because temporal contrast [4, 5] is crucial for most applications of high-peak power laser pulses.

Many devices have been developed to allow the measurement of pulse durations either directly [6] or indirectly through a retrieval algorithm [7] in scanning as well as in single-shot modes [8-10]. Since pulse contrast was of lesser importance and compressor adjustment easy, the dynamic range performance of such devices was never optimized, leaving the high-dynamic-range measurement to the tedious 3-ω scanning cross-correlator. However, investigating the temporal behavior of pulses amplified by new techniques such as OPCPA [11] as well as the complex alignment of compressors with meter size gratings require the development of a device with a high-dynamic range and the capability of single-shot operation.

A standard non-collinear autocorrelator offers a dynamic range which spans over several 10's of dB [12-15], theoretically limited by background photon noise from self-doubled scattered light. Experimentally, this limit is not easily met by lack of a simple detector scheme matching that dynamic range. For the detection scheme, the main challenge resides in achieving analog-to-digital conversion (ADC) with the required bit depth.

In this paper, we experimentally demonstrate a simple detection scheme that can be applied to a cross-correlator setup and improves its dynamic range by several orders of magnitude. To achieve the required bit depth, we use a detector array, as a massively parallel measurement device. Detector arrays, whether Charged Coupled Device (CCD) or Complementary Metal Oxide Semiconductor (CMOS), are now available in large array sizes that exceed 1k x 1k pixels. When collectively used for measuring a single value, an 8-bit 1k x 1k detector array offers virtually 28 bits of detection. However, such a measurement is only beneficial if the signal-to-noise ratio of the unit pixel can be improved through the collective use. Therefore, the first part of the paper addresses the increase of the signal-to-noise ratio, which is done along two axes: the first method increases the signal by modulation of the signal intensity such that the detector scans the signal; the second one uses averaging to reduce the noise. Since single-shot operation is required, these operations need to be performed in parallel on the same detector array. The second part of the paper reports on the experimental implementation of the scheme, as the detection for both scanning and single-shot autocorrelators, where one reaches 57-dB and 60-dB dynamic range respectively, matching the theoretical dynamic-range limit of such devices.

2. Method and predictions

The signal modulation is implemented by use of an uncoated wedge with a reflectivity of 0.18 % at 527 nm, in order to generate a replica of the beam with a reduced intensity on the detector array. The wedge creates a large number of beam replicas, all separated in intensity by the same factor. When two signals are analyzed simultaneously, this gives an additional dynamic range of 27 dB; when three signals, the increase in dynamic range is 54 dB. However, the blooming effect that appears on the CCD signal, when one area is highly saturated, is a technical limitation that makes CCD impractical. The CMOS detector is less sensitive to blooming making it more appropriate for the detection scheme. For experimental reasons, we only used a single replica and therefore our signal gain is limited to 27 dB.

#79388 - $15.00 USD Received 24 Jan 2007; accepted 23 Mar 2007; published 20 Apr 2007

However, it has been reported that CMOS suffers more from noise than scientific CCD cameras [16], and careful noise reduction has to be performed. The noise reduction is based on the averaging technique, but this can only be achieved efficiently when one understands the noise contribution to the signal. The noise can be attributed to two sources: a local contribution σ_{pix} and a contribution σ_{corr} correlated across the detector array:

$$\sigma_{noise} = \sigma_{pix} + \sigma_{corr} \quad (1)$$

The correlated noise, due to fluctuations of external factors, does not benefit from averaging out. The relative weight of the two terms σ_{pix} and σ_{corr} can be analyzed from the graphs in Fig. 1. The graph (a) shows the average pixel value for two different 250 x 250 pixel areas on the CMOS detector chip (Basler A622f camera) recorded simultaneously as a function of the frame number. The second area plot has been offset to increase the visibility of the two plots. The correlated noise is responsible for the correlated evolution of the signals, while the pixel-to-pixel noise characterizes the difference. At first sight, it is clear that the correlated noise dominates the signals. Fig. 1(b) shows the standard deviation of the averaged signal counts, for 1000 frame series, as a function of the pixel number. The log-log plot shows the theoretical limit that is expected from a purely random pixel-to-pixel noise, following the "square root" law. Two types of noise are plotted: first the standard deviation for a single averaging area, and second the standard deviation for the difference between two areas within the same frame (labeled "referenced area" on the plot). Both plots follow the "square root" law for small areas below 10. The benefit from the averaging techniques is clear as the noise reduction is then 10 dB. However, the referenced area method is more efficient for square areas larger than 10 pixels. While a steady state at 12 dB noise reduction is reached for the single-area method, the noise is further decreased when the signal area is referenced to another non-illuminated area of the same frame. For the 250 x 250 pixel square area used later in the paper, the noise is reduced by 18 dB, only 3 dB above the theoretical limit.

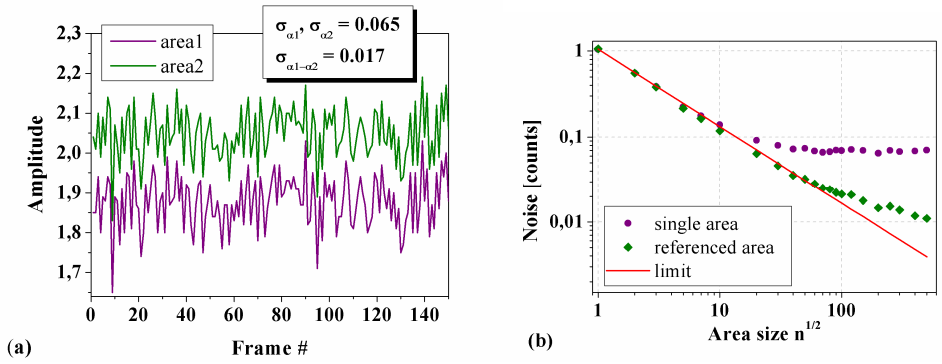

Fig. 1. (a). Noise measurement from two independent 250 x 250 pixel areas of the CMOS chip (, where the second area plot has been offset) shows the possibility to increase the S/N ratio of the camera using an online background reference from a non-illuminated part of the chip. (b) Measurement of the noise dependence from the area size (the 1000 frames statistics): for single signal area (purple) and for signal area after a background subtraction of the 250 x 250 pixel reference area (green). Red line shows the theoretical limit in the case of purely random pixel-to-pixel noise.

As a conclusion, averaging does not help beyond 10 x 10 pixels areas, unless the correlated noise is removed from the frame by utilizing a reference area within the chip. Practically, this corresponds to removing a background term calculated from an unilluminated area (the reference area), scaled by a calibration factor calculated from a dark calibration frame. In such a case, the processed signal S_p will be:

#79388 - $15.00 USD Received 24 Jan 2007; accepted 23 Mar 2007; published 20 Apr 2007

$$S_P = S - S_r \frac{S_0}{S_{r0}}, \tag{2}$$

where S, S_0, S_r and S_{r0} are the signal, the signal of the dark calibration frame, the reference signal and the reference signal of the dark calibration frame, respectively.

This noise reduction, provided it yields a noise at the 0.017 count level, is greatly improving the dynamic range of the CMOS detector. By assuming that the signal fully fills the 255 counts of the detector, the signal-to-noise ratio equals 42 dB. The addition of the replica technique as described above will extend the dynamic range by 27 dB, adding up to a total theoretical dynamic range of 69 dB, if a 250 x 250 pixel detection area is used.

3. Experimental setup and results

Fig. 2 shows a schematic of the experimental setup implemented for the scanning and the single-shot autocorrelators. The details of each autocorrelator scheme are out of the scope of this paper and can be found elsewhere [8-10,17]. In both cases, the detector is an 8-bit CMOS camera - Basler A622f - and the signal is magnified to cover a large area of the chip.

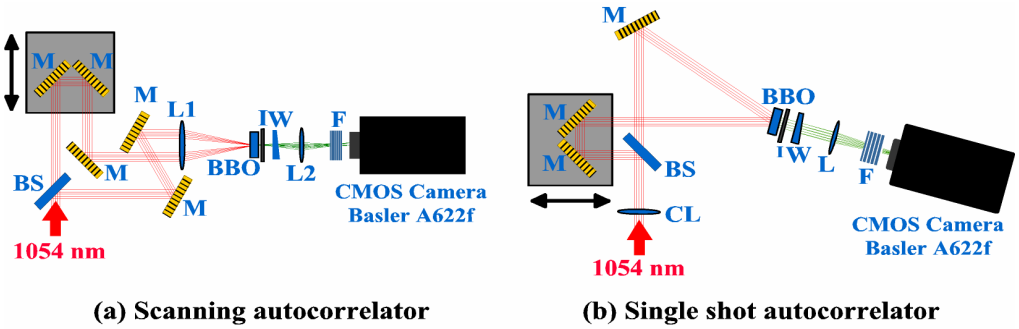

Fig. 2. Experimental setup for the (a) scanning autocorrelator and (b) single-shot autocorrelator: CL - cylindrical lens, BS – beam splitter, M - mirror, BBO - nonlinear crystal, I - iris, W - wedge, L - lens, F - filters (ND, BG39).

In addition the 1° uncoated wedge is located into the setup, creating a beam replica shifted on the camera [Fig. 3(a)]. Fig. 3(b) shows an example of the resulting camera image with the three different areas used for the detection. In the case of the single-shot autocorrelator, a cylindrical lens, located in front of the setup, is used to control the size of the autocorrelation trace in the vertical direction and therefore prevent cross-talk between the main and replica signals on the CMOS chip.

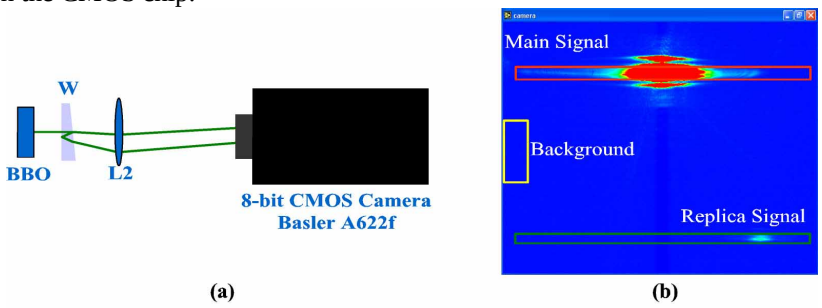

Fig. 3. (a). Using a 1° uncoated wedge a signal replica with an intensity decrease of a factor of 0.0018 is created. (b) CMOS camera image (of the single-shot autocorrelator) showing the three areas used for the signal retrieval.

#79388 - $15.00 USD Received 24 Jan 2007; accepted 23 Mar 2007; published 20 Apr 2007

The detection scheme of the scanning autocorrelator has been validated by measuring the autocorrelation signal from a 150 fs, 300 mW, 76 MHz Ti:sapphire oscillator running at 1053 nm. Fig. 4 shows the results in three different signal retrieval methods. In all cases, the signal is averaged over 10 frames. In the first case, the signal is determined by recording the value of a single pixel without image replica. This autocorrelation trace shows a dynamic range of 27 dB, which is mostly due to the average over 10 frames. The second trace shows the result when the image averaging is performed, but the replicated signal not used. In this case, the dynamic range is increased to 37 dB. The third trace shows the measurement with the replica beam used and yields a dynamic range equal to 52 dB. In this case, the limiting factor comes from the SHG light scattered in to the camera. If one considers the detection noise floor, when the input beam is blocked, the value is 57 dB as shown in Fig. 4.

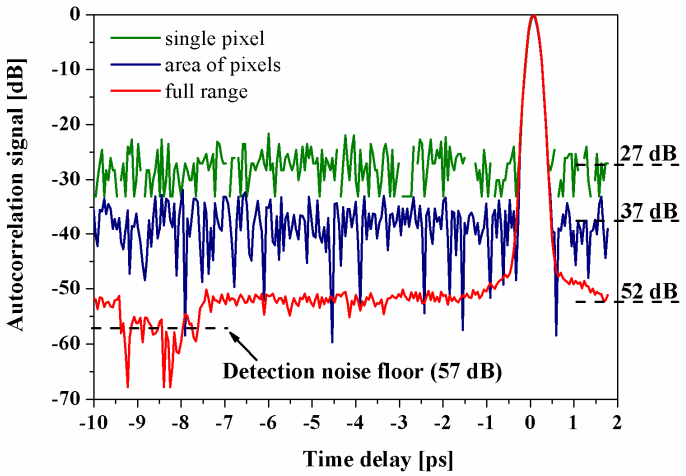

Fig. 4. Autocorrelation signals of the scanning autocorrelator (averaged over 10 frames) for three different detection schemes: (green) the signal is retrieved from a single pixel, (blue) the signal is averaged over a 250 x 250 pixel area, (red) the full detection scheme is used.

The prediction stated that the detection background would be 69 dB. Experimentally, we measure a noise background of 37-dB without the replica and 57-dB with the replica. This shows that the noise reduction done by Eq. (2) does not fully remove the noise from the signal and thus explains for the loss of 5 dB. The second experimental limitation is the available power from the laser that does not allow the replica to fully use the 8-bit dynamic range of the camera. Instead, only 20-dB are used, at best.

Similar results were obtained with the single-shot autocorrelator. The light pulse under study originated from the same Ti:sapphire oscillator running at 1053 nm. However, the pulse energy was too low for a direct measurement; and the pulse was thus amplified in a chirped-pulse amplifier before the measurement. After stretching the pulse to 3 ns, its amplification to 5 mJ and the recompression to ~ 500 fs, only ~ 125 μJ were required for the measurement.

Blurring is not totally absent in the CMOS detector. In particular, the area located in a vertical line of the saturated area exhibits a measurement artifact. For this reason, the replica peak center is shifted horizontally to the side of the chip, as shown in Fig. 3(b). Calibration is easily done in two steps: first for background removal, second for relative peak position assessment. The signal being mapped along one direction, the background referencing is done pixel by pixel rather than globally. Although more CPU intensive, this seems to be more efficient in the background removal as it can be seen later. The raw signal is obtained by binding the pixels along the vertical direction. The mapping of time delays along one direction of the chip means that the number of pixels used for the signal measurement is not as large as in the case of the scanning autocorrelator. To mitigate this effect, a temporal convolution of

#79388 - $15.00 USD Received 24 Jan 2007; accepted 23 Mar 2007; published 20 Apr 2007

the raw signal is operated to reduce the pixel noise. We limit the correlation window to 100 fs to avoid signal broadening. Fig. 5 shows a typical measurement plot. The autocorrelation peak was offset in order to offer a 20-ps temporal window. After a sharp 30-dB decrease of the intensity in 5 ps, the signal exhibits a slow decrease of 10 dB in the following 15 ps. This behavior was not expected and is attributed to a large spectral clipping in the pulse stretcher. We checked that this is not a measurement artifact by blocking one and then the other arm of the autocorrelator to look for self SHG from each arm, which was absent. The time delays beyond 20 ps are mapped outside the SHG crystal area and show the detection background noise, around 60 dB.

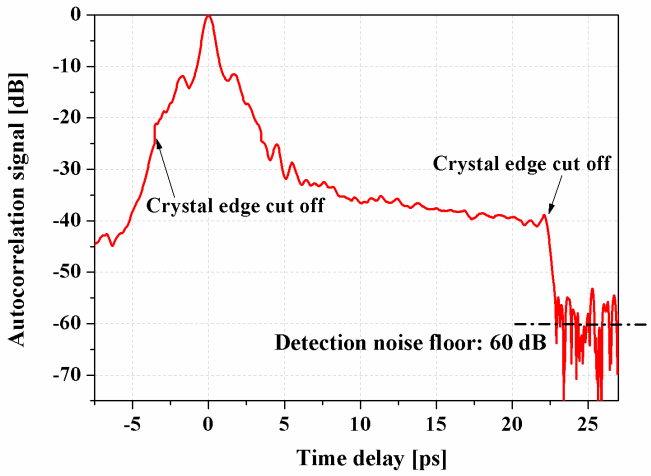

Fig. 5. Autocorrelation signal of the single-shot autocorrelator using the full detection scheme. The sharp edge on the right shows clearly a cut off caused by the limited crystal size.

The average number of pixel used for a single-point measurement is 150, which is 400 times less than used for the prediction. From the plot on Fig. 1(b), a 9-dB reduction can be expected. So the prediction for the single-shot autocorrelator is a 60-dB dynamic range, which is the experimental value. For this setup, the amplified pulse energy allows to make full use of the total dynamic range of the detector. So, by setting the maximum count value for the replica beam above 200 counts, the loss from the maximum range is lower than 1 dB. In addition, background removal seems more efficient than in the scanning autocorrelator so the background noise of the signal without replica is equivalent, although a smaller number of pixels are used.

4. Conclusion

In this paper, we have shown that by using the collective response of the individual pixels of a CMOS detector, one can greatly improve the dynamic range of a standard autocorrelator setup. We have demonstrated that a standard off-the-shelf low-cost 8-bit detector yields up to 60-dB-dynamic-range temporal measurement of short pulses. It is not clear that the use of a detector with a higher bit depth ADC would improve our results; we believe instead that the careful selection of a low noise detector is the solution to improve the result further. In our case, the maximum signal-to-noise ratio of the camera equals 24 dB but other devices can probably exceed this, improving the available dynamic range of this scheme. Although the 60-dB dynamic range does not totally reach the level required for characterizing high-contrast pulses, we have found the autocorrelator an easy-to-use tool for the alignment and early diagnostic of our system.

#79388 - $15.00 USD Received 24 Jan 2007; accepted 23 Mar 2007; published 20 Apr 2007

Appl. Phys. B (2014) 116:429–435
DOI 10.1007/s00340-013-5714-9

Applied Physics B
Lasers and Optics

Temporal contrast control at the PHELIX petawatt laser facility by means of tunable sub-picosecond optical parametric amplification

F. Wagner · C. P. João · J. Fils · T. Gottschall · J. Hein · J. Körner · J. Limpert · M. Roth · T. Stöhlker · V. Bagnoud

Received: 30 May 2013 / Accepted: 22 October 2013 / Published online: 20 November 2013

Abstract We report on the development of a preamplifier module for temporal contrast enhancement and control at petawatt-class lasers. The module is based on an ultrafast optical parametric amplifier (uOPA), which produces temporally clean pulses at the 60 μJ level for seeding a chirped pulse amplification (CPA) system, namely the petawatt facility PHELIX. The amplifier module allows for gain reduction in the following amplifiers, resulting in an attenuation of amplified spontaneous emission (ASE) by more than 4 orders of magnitude. Since the ASE of a CPA system linearly depends on the seeding energy, we were able to demonstrate a continuous variation of the temporal contrast by tuning the gain of the uOPA.

F. Wagner (✉) · M. Roth
Inst. für Kernphysik, Technische Universität Darmstadt, Schlossgartenstr. 9, 64289 Darmstadt, Germany
e-mail: f.wagner@gsi.de

C. P. João
GoLP, Instituto de Plasmas e Fusao Nuclear-Laboratorio Associado, Instituto Superior Técnico, Av. Rovisco Pais, 1049-001 Lisbon, Portugal

J. Fils · T. Stöhlker · V. Bagnoud
GSI Helmholtzzentrum für Schwerionenforschung GmbH, Planckstr. 1, 64291 Darmstadt, Germany

T. Gottschall · J. Limpert
Institute of Applied Physics, Friedrich-Schiller-Universität Jena, Albert-Einstein-Str. 15, 07745 Jena, Germany

J. Hein · J. Körner
Inst. für Optik und Quantenelektronik, Friedrich-Schiller-Universität Jena, Max-Wien-Platz 1, 07743 Jena, Germany

J. Hein · J. Limpert · T. Stöhlker · V. Bagnoud
Helmholtz-Institut Jena, Fröbelstieg 3, 07743 Jena, Germany

1 Introduction

In the last 10 years, ultra-high-intensity lasers have become widely spread in laboratories around the world. With the ever-increasing achievable on-target intensities, the temporal contrast of such lasers has recently been brought to the foreground of laser development preoccupations. Ultrashort laser pulses are traditionally amplified using the chirped pulse amplification (CPA) technique [1] or optical parametric CPA [2]. Both techniques suffer from an intrinsic temporal pedestal on the nanosecond timescale [3]. In general, the energy of the pulses effectively seeding the amplifier is in the sub-nanojoule range, and the corresponding signal-to-noise ratio after amplification reaches typically 10^6–10^8 depending on the seed coupling efficiency. Moreover, since the pulse is stretched during the amplification process, fast optical switches like Pockels cells (PCs) cannot be used to discriminate between the coherent pulse and its pedestal at this stage, while this becomes very complicated after the laser pulses have been re-compressed.

At the same time, the requirements of recent solid target interaction experiments on the temporal contrast become more and more specific. While for several lately proposed experiments like probing ion acceleration mechanisms with thin targets in the sub-micrometer range [4, 5], a high temporal contrast is mandatory to ensure that the target is not destroyed by a prepulse or pedestal; for others, a certain preplasma at the target surface is favorable. Depending on the scale length of the preplasma, different laser absorption mechanisms may dominate resulting in different efficiencies of coupling laser energy into the target. Additionally, ponderomotive and relativistic self-focussing might occur in the preplasma, changing the maximum achievable intensity. Hence, the optimum preplasma strongly depends

on the application, and an adjustable contrast level is desirable for a user laser facility.

It was demonstrated in 1998 [6] that the amplified spontaneous emission (ASE) in CPA lasers could be suppressed by injection of a clean seed pulse at the microjoule level. By now, a high temporal contrast level is typically achieved by the step-wise approach of temporal pulse cleaning during amplification [7]. In this scheme, the laser pulse is amplified to the millijoule level in a first stage of the laser using a first CPA arrangement and temporally filtered using nonlinear techniques. The resulting pulse has similar properties to the oscillator pulse but, at an energy level many orders of magnitude higher, so that the signal-to-noise ratio of the second stage of amplification is much more favorable. One particular implementation of the double CPA concept uses nonlinear cleaning based on crossed wave polarization [8], and it is now widely used in titanium-doped sapphire CPA laser systems around the world. Unfortunately, the double CPA concept turns out to be very unpractical for petawatt-class lasers based on Nd:glass or Ytterbium-doped amplifiers because the corresponding stretcher and compressor are very bulky, even in the front end of the laser. For this reason, Dorrer et al. [9] proposed an alternate method based on direct amplification of the oscillator pulses in an ultrashort optical parametric amplifier (uOPA). More recently, this method has also been successfully applied to a Ti:sapphire-based CPA system [10] showing its versatility. Because of the instantaneous nature of the parametric process, the signal-to-noise ratio of the laser oscillator is not degraded outside of the amplification time window, which can be very short. Ideally, the pump pulse used for the uOPA should be shorter than 1 picosecond to avoid plasma expansion on the picosecond scale. But unfortunately, in previous work [9, 11], the pump pulse was generated by direct amplification of a short pulse in a diode-pumped Nd:YLF laser, and the achievable pulse duration was limited by the bandwidth of the amplification material to more than 5 ps.

In this paper, we demonstrate that the simultaneous operation of an uOPA together with a linear regenerative amplifier allows for continuous tuning of the temporal contrast in a petawatt-class laser. One inherent advantage of our approach is that the pump pulse is generated using a diode-pumped Yb-doped amplifier that has enough bandwidth to support sub-picosecond laser pulses as dictated by solid target interaction experiments. In addition, the requirement on the temporal quality of the pump laser in the uOPA is not as high as for the double CPA scheme, which allows for using a compact and cost-effective stretcher/compressor setup based on a single chirped volume Bragg grating (VBG). Finally, with VBGs available at larger sizes and laser diode-pumped Ytterbium amplifiers nowadays reaching the 1 J level, the scheme is fully scalable to higher contrast levels. This paves the way for pedestal-free pulses at even higher intensities.

2 Temporal contrast at the PHELIX laser facility

The uOPA was developed and optimized to be applied as a pulse cleaner at the PHELIX [12] short-pulse laser system. The system uses the technique of CPA to deliver pulses with minimum duration of 400 fs, maximum energy of up to 250 J at a repetition rate of one shot every 90 min. With a F2-parabolic mirror, the beam can be focused down to reach maximum intensities of up to 2×10^{21} W/cm^2. This requires a good contrast to prevent ionization of targets prior to the main pulse.

In order to understand the contrast deterioration, one has to consider generation and build-up of the high energy pulses in the system. Like in all conventional petawatt-class laser systems, the high energy level is achieved by using a multi-stage amplification chain (see Fig. 1). A Ti:sapphire-based short-pulse oscillator (Mira 900, Coherent) provides 100 fs pulses at a nanojoule energy level with a repetition rate of 72 MHz. The spectrum of the pulses is shown in Fig. 3a. Even though the laser medium is Ti–sapphire with a maximum cross section around 800 nm, the spectrum is shifted to 1,053 nm to match the cross section of the subsequent glass amplifiers. Without the contrast-boosting uOPA, these pulses first go to a grating stretcher where they are stretched by a factor of 190 ps/nm to a duration of 2.4 ns. Then, two successive regenerative Ti–sapphire amplifiers, both working at

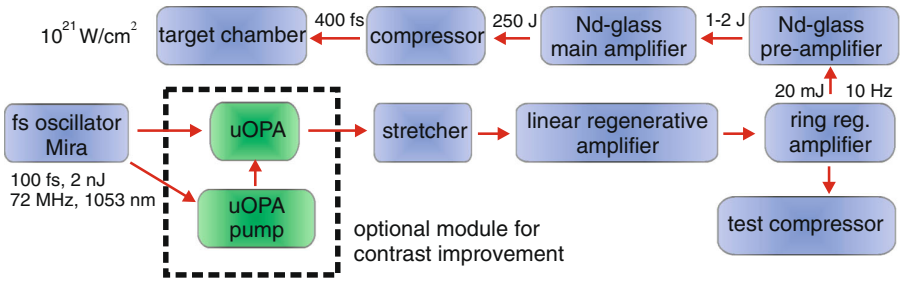

Fig. 1 The PHELIX short-pulse laser system

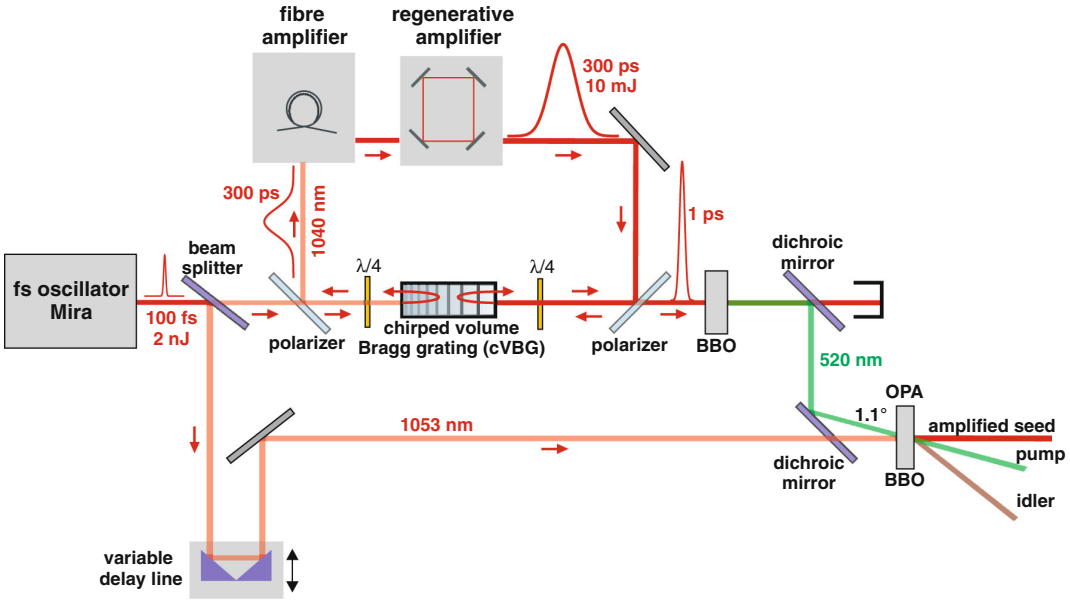

Fig. 2 Setup of the uOPA

10 Hz, deliver pulses with energies above 20 mJ. One of these pulses is then further amplified up to 250 J by two Nd:glass amplifiers and finally recompressed to 400 fs using a grating compressor. In addition, a 30-cm diameter faraday rotator protects the system against back-reflected light, and four isolation stages based on PC pulse pickers are used to eliminate prepulses and the ASE on the nanosecond timescale.

The contrast, in the context of this paper, is defined by the ratio of the main pulse intensity to the intensity of the background radiation of the system. This is linked to the more general problem of signal-to-noise ratio in quantum amplifiers. Here, in the temporal range of some tens of ps up to 1.5 ns before the pulse, the noise is due to ASE which cannot go below the quantum noise level. Therefore, our approach aims for increasing the signal to improve the contrast. This can be accomplished directly after the short-pulse oscillator.

Other contrast-deteriorative factors, such as spectral clipping, or phase noise in the CPA process, or generation of pre- and postpulses due to multiple reflections, are not addressed by the uOPA and must be considered separately.

3 Setup of the uOPA

A main challenge of the uOPA is the generation of a pump pulse which fulfills the following requirements: a duration of not more than one picosecond, as well as a low temporal jitter between the pump and signal pulses. An additional demand for the pump laser is a setup as compact as possible to be suitable for the PHELIX system. The setup of the uOPA is shown in a schematic in Fig. 2. In our realization, both pump and signal pulses originate from the same oscillator in order to account for the low jitter requirements. By using a 50:50 beamsplitter, half of the beam directly propagates to the beta barium borate (BBO) crystal, where it is amplified in the OPA process. A motorized delay line is used to temporally overlap the seed with the pump pulse. The other part is amplified in a compact CPA system and serves as the pump pulse in the OPA. First, the pulse is stretched to 300 ps after being reflected in a VBG (OptiGrate Corp.). This VBG was designed to reflect a 5-nm bandwidth pulse centered at 1,040 nm. The central wavelength matches the amplifiers which both use Ytterbium as active material. The main advantage of the VBG compared with conventional grating-based stretcher–compressor assemblies is its compactness, cost and ease of use. Both stretching and recompression of the pulse are carried out in the same VBG with dimensions in the order of a few centimeters. In Fig. 3a, the part of the spectrum which is extracted from the original spectrum delivered by the fs oscillator is shown. It can clearly be seen (the spectra are not normalized with respect to each other) that the efficiency of the VBG in the dedicated wavelength range is nearly 100 %. Besides its compactness, this is another important advantage of the VBG. The stretched pulses are then amplified in two consecutive amplifiers. The first amplification takes place in a two-stage Ytterbium-doped fiber amplifier. In a

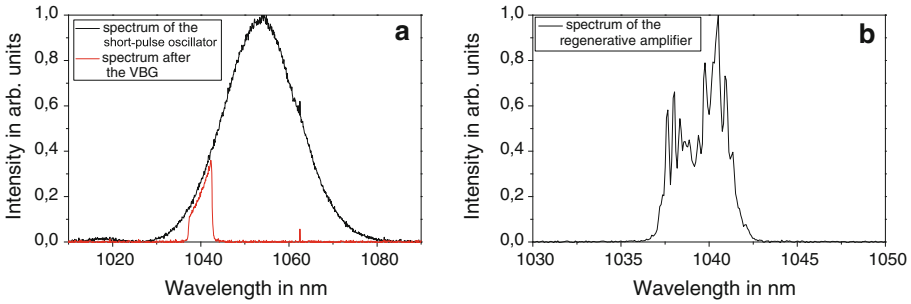

Fig. 3 Spectra of the short-pulse oscillator (*a-black*), after the VBG (*a-red*) and output of the regenerative amplifier for a pulse energy of 4.5 mJ (**b**)

single mode fiber, the stretched pulses with an average power of 1–2 mW and a repetition rate of 72 MHz are amplified to 160 mW. The repetition rate is then reduced to 1 MHz using an acousto-optical modulator (AOM) synchronized with the PHELIX laser system. A second stage then creates an output of 1 W corresponding to pulse energies of 1 μJ. The beam then goes to a regenerative ring amplifier operating at 10 Hz [13]. The amplifier uses Yb:KGW as an active medium pumped by a laser diode module (Lastronics GmbH) which is capable of delivering up to 2.4 kW peak power at 940 nm. Output of the ring is a pulse train with nominal pulse energies of 10 mJ and a bandwidth of 5 nm centered at 1,040 nm. However, due to nonlinear effects, the spectrum exhibits strong modulations at higher energies. Therefore, we decided to limit the output energy to 4.5 mJ, an energy level for which no visible effect on the parametric amplification could be detected. The spectrum after the ring amplifier (Fig. 3b) exhibits the same bandwidth as the input beam, which enables compression of the pulses to 1 ps with the VBG. This is accomplished by using the VBG in the direction opposite to the stretching direction. It should be noted that the compression factor applied by the VBG does not address the additional dispersion introduced by the propagation through the fiber and material in the regenerative amplifier. For this reason, the output pulse is not as short as its corresponding Fourier transform limit (600 fs), but rather lightly chirped and its duration increased to 1 picosecond.

In order to use the pulses as pump pulses in the OPA process, they need to be frequency doubled, which is accomplished in a BBO crystal. The frequency-doubling stage for the pump laser and the parametric amplifier were simulated and dimensioned using the Miro software [14] with the specific module handling four wave mixing of broadband pulses. The doubling crystal is located about 250 cm from the waist of the regenerative cavity, and the pump-laser beam diameter equals 2.9 mm (FWHM) at the crystal location, due to the natural divergence of the beam. This produces a maximum available intensity of 150 GW/cm^2. For this intensity, we estimated that a 2.9 mm Type I BBO crystal offers the optimal length to drive the frequency conversion into saturation, and consequently, it minimizes the energy fluctuation noise. A fraction of 50 % from the 4.5 mJ at fundamental wavelength can be converted to green, which results in a pump-pulse energy of about 2.3 mJ at the OPA-crystal. Two dichroic mirrors are used to separate the pump beam at 520 nm from the residual infrared radiation that has not been converted in the BBO crystal. The second dichroic mirror also serves as a beam combiner for the signal and pump, since it is highly transmissive for infrared and highly reflective for 520 nm. To meet the requirements for phase matching in the BBO crystal, the angle between the pump pulse at 520 nm and the seed pulse at 1,053 nm has to be unequal to zero degrees. Using the Miro software, an optimum angle of 1.1 degrees was calculated. This also enables to separate the amplified signal from the residual pump and the idler.

Due to the long optical path in the fiber amplifier as well as the regenerative amplifier, a single pulse generated by the oscillator cannot be used simultaneously as pump and seed pulse in the OPA. Therefore, two different pulses with a temporal separation of 1.2 microseconds are used in our setup which was identified as a possible source of jitter or drift.

First, jitter was minimized in our setup by locking the oscillator to an external 72 MHz reference rf signal which is stabilized to the Hz level. This ensures the stability between the subsequent pulses of the oscillator. Second, a compact design allows for minimizing the impact of local vibration effects.

With a pump-pulse energy of 2.3 mJ, we reach saturation in the OPA, which corresponds to a conversion efficiency of about 3 %. This value can be explained by the not optimally matched pulse duration of the pump and seed pulses. To improve the conversion efficiency, the seed pulse was stretched to a duration of 300 fs using multiple reflections from two chirped mirrors. Consequently, we were able to double the efficiency. However, the outcome

of this was fluctuations in the pulse duration after re-compression of the amplified pulses after the regenerative amplifiers of the PHELIX front end (Fig. 1). This was attributed to the jitter between the seed and the pump pulses resulting in a nonlinear, pulse-to-pulse varying spectral phase which cannot be compensated for within the compressor. Therefore, we decided to operate the uOPA at the lower conversion efficiency in favor of a better long-term stability of the whole system.

In order to maintain a constant energy output level of the OPA, the temporal overlap between the pump and seed pulses needs to be preserved during operation. In the course of the day, we observed an unidirectional drift of a few ps between both pulses which was related to the warm-up of the regenerative cavity resulting in a longer optical path for the pump pulse. This effect can be compensated for by adjusting the variable delay line for the signal beam. This is achieved by an automated closed-loop locking the delay line position to the uOPA output energy. When this loop is active, the synchronization is maintained in routing operation over more than 12 h per day. As far as jitter is concerned, with the compressed signal pulse, we could not observe any instability that could be attributed to it. With the pump-pulse duration being by a factor of ten longer compared with the signal pulse, the low jitter requirement becomes less critical.

4 Integration to the PHELIX short-pulse laser chain and contrast measurements

The uOPA module was integrated to the PHELIX short-pulse system and can be used at any time during daily operation. Switching between the configuration with and without the pulse cleaner is very easy and can be arranged within minutes. As illustrated in Fig. 1, the uOPA is placed directly behind the short-pulse oscillator. After the uOPA the amplified signal pulse is sent to the grating stretcher and subsequently to the two regenerative amplifiers of the PHELIX short-pulse front end. Due to the higher input signal the amplification in the regenerative amplifiers can be reduced to deliver the same output energy level of 20 mJ. This is accomplished by decreasing the pumping laser energy in the linear regenerative amplifier which results in less ASE production. Because the optical path and timing of the regenerative amplifier is identical for both operation modes, the changeover between the two configurations is straightforward.

To measure the contrast with the new module, the laser pulses amplified in the front end were sent to a local compressor (Fig. 1). Because the amplification in the glass amplifier is not saturated, we do not expect a degradation of the temporal contrast between the front part of the pulse and its peak. In addition, the ASE contribution of the glass

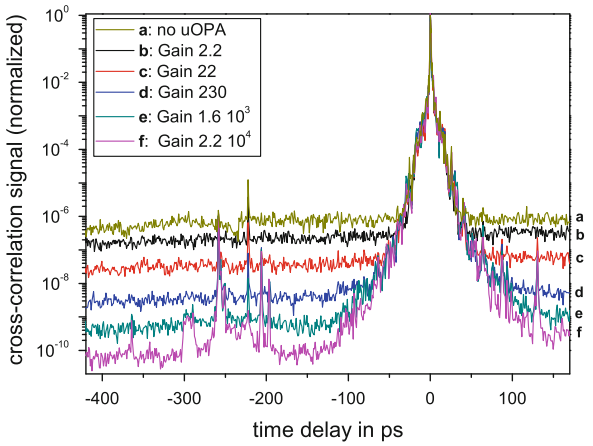

Fig. 4 Improvement of the ASE contrast for different gain levels in the uOPA

amplifier was estimated theoretically and measured experimentally to be negligible to play any role in the picosecond ASE contrast level of the laser pulse. Therefore, we believe that the measurement done at the output of the front end is also representative of the temporal contrast of the laser pulse at full energy. At this stage, the system is still operating at 10 Hz. Hence, a scanning third-order cross-correlator with high dynamic range (Sequoia, Amplitude Technology) can be used. We performed the measurement for different gain levels in the uOPA by variation of the OPA pump-pulse energy. This was done with a half-waveplate and polarizer arrangement, used together with a photodiode that monitored the uOPA gain on an oscilloscope. For each gain level, the subsequent regenerative amplifier was maintained in saturation by adjusting the pump energy of the driving Nd:YAG pump laser using a waveplate and polarizer. By doing so, the energy at the output of the regenerative amplifier remains nearly unchanged, while the gain is shifted from the regenerative amplifier to the uOPA and the ASE originating in the regenerative amplifier accordingly reduced. The results are shown in Fig. 4. In order to compare the different ASE levels, the curves were normalized with respect to each other. This was carried out by overlapping the slopes of each curve. The upper curve was recorded with no gain in the OPA corresponding to the standard setup without the uOPA module. The ASE is at the 10^{-6} level which is typical for a front end with no additional contrast-improving components. Starting with a gain factor of 2.2 and increasing it stepwise by factors of nearly 10, the ASE drops down almost linearly with the OPA gain. For a gain of 2.2×10^4, the ASE level exceeds the detection limit of the cross-correlator which is slightly below 10^{-10}.

The curve with the highest contrast exhibits a slowly rising slope ranging up to 100 ps before the peak. This is

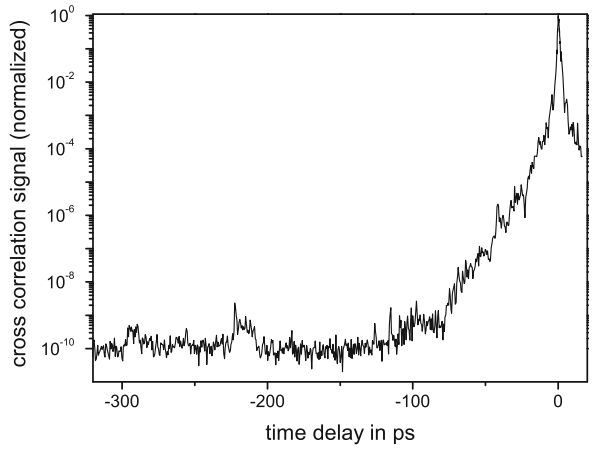

Fig. 5 Temporal contrast after the removal of all prepulses for a gain of 2×10^4 in the uOPA

attributable to coherent effects such as clipping of the spectrum or scattering from the diffraction gratings in the stretcher [15]. This slope can be detrimental to the experiments that are the most sensitive to pre-ionization effects. Therefore, solutions like increasing the stretcher bandwidth by 50 % and replacing the gratings for higher quality components are currently considered.

In addition, when a very high ASE contrast is achieved, prepulses between -300 and -200 ps become visible. These effects are not addressed by the uOPA and therefore have to be treated separately. In general, prepulses can be generated in a CPA system from the interplay between postpulses and nonlinear effects (nonlinear Kerr effect) [16]. In particular, we could identify that the prepule at 200 ps was due to double reflections from a PC with parallel surfaces in the PHELIX front end. Hence, it was not addressed by the uOPA. By switching to a specially designed PC with tilted end faces, the prepulse could be removed. Furthermore, the prepulses around 250 ps which were caused by double reflections from several cube polarizers in the front end could be eliminated by exchanging these polarizers.

The prepulse at about 220 ps is caused by injection of another pulse from the oscillator into the regenerative amplifiers. Therefore, it drops down with increasing uOPA gain, as well. The final contrast level after the prepulse removal and with an applied gain of 2×10^4 in the uOPA is shown in Fig. 5.

5 Conclusion

A compact preamplifier based on sub-picosecond OPA was developed and successfully integrated to the PHELIX petawatt laser system. With this module, an improvement of the ASE contrast from 10^6, which is typical for CPA systems, to more than 10^{10}, could be demonstrated. This enlarges the spectrum of experiments feasible at the PHELIX laser facility. Preliminary tests on ion acceleration with thin targets showed that the current contrast allows studying laser matter interaction with targets in the submicrometer range. In particular, this enables testing new laser ion acceleration mechanisms like the laser break-out afterburner [4], or radiation pressure acceleration [5] at PHELIX which are planned for the near future.

Our measurement also confirms that the ASE level in a CPA system linearly depends on the energy of the seed pulse. Consequently, by proper tuning, the gain between the uOPA and the following linear regenerative amplifier, an arbitrary ASE level between 6 and 10 orders of magnitude can be accomplished, while maintaining the total output energy level of the system. This is very favorable for a user laser facility, since a controllable preplasma can be useful for many types of applications.

Acknowledgments This work was supported by the BMBF 06DA9044I and the Helmholtz-Institute Jena.

References

1. D. Strickland, G. Mourou, Opt. Commun. **55**, 447–449 (1985)
2. A. Dubietis, G. Jonusauskas, A. Piskarskas, Opt. Commun. **88**, 437–440 (1992)
3. V.V. Ivanov, A. Maksimchuk, G. Mourou, Appl. Opt. **42**, 7231–7234 (2003)
4. L. Yin, B.J. Albright, B.M. Hegelich, J.C. Fernández, Laser Part. Beams **24**, 291–298 (2006)
5. A. Macchi, S. Veghini, T. Liseykina, F. Pegoraro, New Phys. **12**, 045013 (2010)
6. J. Itatani, J. Faure, M. Nantel, G. Mourou, S. Watanabe, Opt. Commun. **148**, 70–74 (1998)
7. M.P. Kalashnikov, E. Risse, H. Schönnagel, W. Sandner, Opt. Lett. **30**, 923–925 (2005)
8. A. Jullien, O. Albert, F. Burgy, G. Hamoniaux, J.-P. Rousseau, J.-P. Chambaret, F. Augé-Rochereau, G. Chériaux, J. Etchepare, N. Minkovski, S.M. Saltiel, Opt. Lett. **30**, 920–922 (2005)
9. C. Dorrer, I.A. Begishev, A.V. Okishev, J.D. Zuegel, Opt. Lett. **32**, 2143–2145 (2007)
10. C. Liu, Z. Wang, W. Li, Q. Zhang, H. Han, H. Teng, Z. Wei, Opt. Lett. **35**, 3096–3098 (2010)
11. I. Musgrave, W. Shaikh, M. Galimberti, A. Boyle, C. Hernandez-Gomez, K. Lancaster, R. Heathcote, Appl. Opt. **49**, 6558–6562 (2010)
12. V. Bagnoud, B. Aurand, A. Blazevic, S. Borneis, C. Bruske, B. Ecker, U. Eisenbarth, J. Fils, A. Frank, E. Gaul, S. Goette, C. Haefner, T. Hahn, K. Harres, H.-M. Heuck, D. Hochhaus, D.H.H. Hoffmann, D. Javorková, H.-J. Kluge, T. Kuehl, S. Kunzer, M. Kreutz, T. Merz-Mantwill, P. Neumayer, E. Onkels, D. Reemts,

O. Rosmej, M. Roth, T. Stoehlker, A. Tauschwitz, B. Zielbauer, D. Zimmer, K. Witte, Appl. Phys. B **100**, 137–150 (2010)
13. C. P. João, J. Körner, M. Kahle, H. Liebetrau, R. Seifert, M. Lenski, S. Pastrik, J. Hein, T. Gottschall, J. Limpert, G. Figueira and V. Bagnoud, High-power Yb:KYW picosecond regenerative amplifier for optical parametric amplifier pumping. Proc. SPIE 8001, International Conference on Applications of Optics and Photonics, 80011E (July, 2011)
14. O. Morice, Opt. Eng. **42**, 1530–1541 (2003)
15. C. Hooker, Y. Tang, O. Chekhlov, J. Collier, E. Divall, K. Ertel, S. Hawkes, B. Parry, P.P. Rajeev, Opt. Exp. **19**, 2193–2203 (2011)
16. N.V. Didenko, A.V. Konyashchenko, A.P. Lutsenko, S.Yu. Tenyakov, Opt. Exp. **16**, 3178–3190 (2008)

Pre-plasma formation in experiments using petawatt lasers

Florian Wagner,[1,*] Stefan Bedacht,[1] Alex Ortner,[1] Markus Roth,[1] Anna Tauschwitz,[2] Bernhard Zielbauer,[3,4] and Vincent Bagnoud[3,4]

[1]*Institut für Kernphysik, Technische Universität Darmstadt, Schlossgartenstr. 9, 64289 Darmstadt, Germany*
[2]*Institute for Theoretical Physics, Frankfurt University, Max-von-Laue-Str. 1, 60438 Frankfurt am Main, Germany*
[3]*GSI Helmholtz Center for Heavy Ion Research, Planckstr. 1, 64291 Darmstadt, Germany*
[4]*Helmholtz Institute Jena, Fröbelstieg 3, 07743 Jena, Germany*
[*]*f.wagner@gsi.de*

Abstract: We used time-resolved shadowgraphy to characterize the pre-plasma formation in solid-target interaction experiments with micrometer-scale accuracy. We performed quantitative measurements of the plasma density for amplified spontaneous emission (ASE) levels ranging from $2 \cdot 10^{-7}$ to 10^{-10} backed with 2-dimensional hydrodynamic simulations. We find that ASE levels above 10^{-9} are able to create a significant pre-plasma plume that features a plasma canal driving a self-focusing of the laser beam. For ASE levels of 10^{-10}, no ASE pre-plasma could be detected.

OCIS codes: (350.5400) Plasmas; (280.5395) Plasma diagnostics; (140.3295) Laser beam characterization; (140.3330) Laser damage; (140.7090) Ultrafast lasers.

References and links

1. A. Macchi, S. Veghini, T. Liseykina, and F. Pegoraro, "Radiation pressure acceleration of ultrathin foils," New J. Phys. **12**(4), 045013 (2010).
2. C. Thaury, F. Quéré, J.-P. Geindre, A. Levy, T. Ceccotti, P. Monot, M. Bougeard, F. Réau, P. d'Oliveira, P. Audebert, R. Marjoribanks, and Ph. Martin, "Plasma mirrors for ultrahigh-intensity optics," Nat. Phys. **3**(6), 424–429 (2007).
3. P. McKenna, D. C. Carroll, O. Lundh, F. Nürnberg, K. Markey, S. Bandyopadhyay, D. Batani, R. G. Evans, R. Jafer, S. Kar, D. Neely, D. Pepler, M. N. Quinn, R. Redaelli, M. Roth, C.-G. Wahlström, X. H. Yuan, and M. Zepf, "Effects of front surface plasma expansion on proton acceleration in ultraintense laser irradiation of foil targets," Laser Particle Beams **26**(04), 591–596 (2008).
4. A. Jullien, O. Albert, F. Burgy, G. Hamoniaux, J. P. Rousseau, J. P. Chambaret, F. Augé-Rochereau, G. Chériaux, J. Etchepare, N. Minkovski, and S. M. Saltiel, "10^{-10} temporal contrast for femtosecond ultraintense lasers by cross-polarized wave generation," Opt. Lett. **30**(8), 920–922 (2005).
5. C. Dorrer, I. A. Begishev, A. V. Okishev, and J. D. Zuegel, "High-contrast optical-parametric amplifier as a front end of high-power laser systems," Opt. Lett. **32**(15), 2143–2145 (2007).
6. H. C. Kapteyn, M. M. Murnane, A. Szoke, and R. W. Falcone, "Prepulse energy suppression for high-energy ultrashort pulses using self-induced plasma shuttering," Opt. Lett. **16**(7), 490–492 (1991).
7. M. M. Basko, J. Maruhn, and A. Tauschwitz, "Development of a 2D radiation hydrodynamics code RALEF for laser plasma simulations," in *GSI Report 2010–1* p. 410 (GSI Helmholtzzentrum für Schwerionenforschung, 2010).
8. V. Bagnoud, B. Aurand, A. Blazevic, S. Borneis, C. Bruske, B. Ecker, U. Eisenbarth, J. Fils, A. Frank, E. Gaul, S. Goette, C. Haefner, T. Hahn, K. Harres, H.-M. Heuck, D. Hochhaus, D. H. H. Hoffmann, D. Javorková, H.-J. Kluge, T. Kuehl, S. Kunzer, M. Kreutz, T. Merz-Mantwill, P. Neumayer, E. Onkels, D. Reemts, O. Rosmej, M. Roth, T. Stoehlker, A. Tauschwitz, B. Zielbauer, D. Zimmer, and K. Witte, "Commissioning and early experiments of the PHELIX facility," Appl. Phys. B **100**(1), 137–150 (2010).
9. F. Wagner, C. P. João, J. Fils, T. Gottschall, J. Hein, J. Körner, J. Limpert, M. Roth, T. Stöhlker, and V. Bagnoud, "Temporal contrast control at the PHELIX petawatt laser facility by means of tunable sub-picosecond optical parametric amplification," Appl. Phys. B **116**(2), 429–435 (2014).
10. C. P. João, J. Körner, M. Kahle, H. Liebetrau, R. Seifert, M. Lenski, S. Pastrik, J. Hein, T. Gottschall, J. Limpert, and V. Bagnoud, "Development of a 10 mJ-level optically synchronized picosecond Yb:KYW amplifier at 1040 nm for OPCPA pumping," Proc. SPIE **8080**, 808008 (2011).
11. N. V. Didenko, A. V. Konyashchenko, A. P. Lutsenko, and S. Y. Tenyakov, "Contrast degradation in a chirped-pulse amplifier due to generation of prepulses by postpulses," Opt. Express **16**(5), 3178–3190 (2008).

#224082 - $15.00 USD Received 30 Sep 2014; revised 4 Nov 2014; accepted 5 Nov 2014; published 18 Nov 2014

12. M. Borghesi, J. Fuchs, S. V. Bulanov, A. J. Mackinnon, P. K. Patel, and M. Roth, "Fast Ion Generation by high-Intensity Laser Irradiation of Solid Targets and Applications," Fusion Sci. Technol. **49**, 412–439 (2006).
13. P. Mulser and D. Bauer, *High Power Laser–Matter Interaction* STMP 238 (Springer, 2010) p.78.
14. S. Faik, M. M. Basko, A. Tauschwitz, I. Iosilevskiy, and J. A. Maruhn, "Dynamics of volumetrically heated matter passing through the liquid-vapor metastable states," High Energy Density Phys. **8**(4), 349–359 (2012).
15. A. F. Nikiforov, V. G. Novikov, and V. B. Uvarov, *Quantum-statistical models of hot dense matter: methods for computation of opacity and equation of state* (Birkhäuser, 2005).

1. Introduction

Lasers reaching peak powers in the petawatt range and intensities above 10^{21} W/cm^2 are nowadays available for a wide range of experiments in laboratories around the world. For many experiments, the interaction with solid and mostly undisturbed targets is a prerequisite [1, 2]. However, the temporal shape of highly intense short laser pulses often exhibits complicated structures including pre-pulses, an incoherent nanosecond pedestal and wings, which pre-ionize the target and thereby strongly influence the laser-matter interaction. The temporal structure of these light pulses is far from the Gaussian or "top hat" pulses used in simulations and this feature makes experimental results hard to interpret: first, a precise measurement of the laser pulse over 120 dB and many nanoseconds would be necessary to perfectly characterize the experimental conditions, and second, simulation tools capable of handling the many physical processes happening over intensities ranging from the ionization threshold at 10^9 W/cm^2 up to maximum intensities exceeding 10^{21} W/cm^2 would be required. Still, both experiment and simulation fail to deliver such tools.

There is a general agreement that pre-ionization strongly influences experimental data. In a limited number of cases, a certain pre-plasma can improve the outcome of the experiment. For instance in laser-ion acceleration with micrometer-thick targets, the enhanced absorption and self-focusing in the pre-plasma leads to higher maximum ion energies [3]. However, in order to exploit this effect, a precise control of the pre-plasma is essential. In contrast to these cases, there are also applications that cannot tolerate pre-ionization [1, 2]. For this reason, several techniques have been proposed and implemented to improve the temporal contrast of short-pulse lasers either in the front-end of those [4,5] or shortly before the interaction point [6]. As a consequence, a qualitative improvement has been reported for those experiments requiring high temporal contrast. However, these techniques also create different temporal pulse-profiles that complicate the comparison between experimental results. Therefore a systematic characterization of the pre-plasma plume for different contrast levels is desirable.

In this paper, we exploit a standard time-resolved shadowgraphy method to make an in situ characterization of the pre-plasma created by a short-pulse laser whose temporal contrast can be adjusted over up to 5 orders of magnitude. We use three pulse profiles which we consider representative of what can be found in short-pulse lasers around the world, with temporal contrast levels ranging from standard to ultra-high. The measured pre-plasma shadow shows a complicated spatial structure, which is analyzed and explained with the help of the RALEF-2D hydrodynamic simulation code [7]. In particular, the pre-plasma geometry can yield a significant self-focusing of the beam for the standard temporal contrast case.

2. Experimental setup

The experimental data was gathered at the PHELIX high-energy laser facility [8] in Darmstadt, Germany, where a high-contrast front-end based on the ultrafast Optical Parametric Amplification (uOPA) concept [5] was recently commissioned [9]. As shown in Fig. 1, the short oscillator pulses (100 fs) are directly amplified at the output of the short pulse laser oscillator using a time-gated parametric amplifier leading to short pulses of 100 microjoules without any degradation of its picosecond and nanosecond temporal-contrast properties. Parametric amplification imposes serious requirements on the pump beam used in the process such that a dedicated laser-diode-pumped pump laser had to be developed to fulfill the tight timing, pulse-duration and energy requirements. Thanks to this design [10], 5-

#224082 - $15.00 USD Received 30 Sep 2014; revised 4 Nov 2014; accepted 5 Nov 2014; published 18 Nov 2014

1 December 2014 | Vol. 22, No. 24 | DOI:10.1364/OE.22.029505 | OPTICS EXPRESS 29506

mJ pulses at 520 nm with a pulse duration of about 1 ps enable reaching amplification gains of up to $2 \cdot 10^5$, which linearly translates into a reduction of the final nanosecond ASE of the laser. Depending on the amplification factor of the uOPA, the pumping-laser energy delivered to the first regenerative amplifier is accordingly reduced such that the regenerative amplifier still reaches saturation and delivers about the same output energy. In all cases, the amplification factor of uOPA and regenerative amplifiers remains constant at about 10^8.

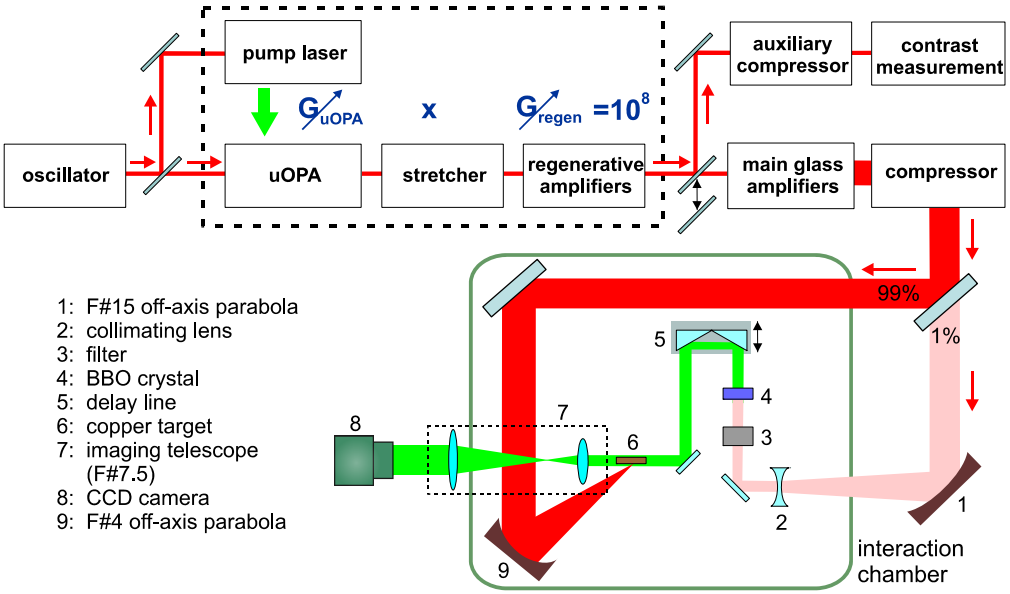

Fig. 1. Experimental setup.

For the experiment three gain levels of the uOPA were used: 1, 200 and $4 \cdot 10^4$, yielding the three temporal curves shown in Fig. 2, exhibiting a temporal ASE pedestal at $2 \cdot 10^{-7}$, $4 \cdot 10^{-9}$ and 10^{-10} with respect to the maximum intensity of the pulse, respectively. The temporal profiles where recorded at the output of the front-end, using an auxiliary compressor and a scanning high-dynamic-range third-order cross-correlator (Sequoia, Amplitude Technologies). As was already documented and discussed before [9], this measurement is a true representation of the final pulse profile that undergoes little distortion in the rest of the amplifier. Because the cross-correlator only delivers an information in the vicinity of the pulse maximum over a temporal window of roughly 500 ps, the temporal profile of the laser pulse is additionally recorded at full energy at the output of the compressor with sub-nanosecond accuracy using a fast photodiode (Thorlabs D400FC) and a 2.5 GHz oscilloscope (Tektronix TDS7254), as shown in the insert of Fig. 2. The measurement is truncated at 1 because of the scale used with the oscilloscope. Since the photodiode had to be highly saturated at the maximum intensity in order to attain a detectable ASE level, this measurement does not provide proper results for times which are closer to the maximum than 100 ps. For the highest ASE level, a pre-pulse at −115 ps can be noticed, which we attribute to beats between the oscillator and the first regenerative amplifier (multiple pulse injection). The amplitude of this pre-pulse is anti-proportional to the gain of the uOPA since only one pulse of the 72 MHz oscillator is amplified. This is confirmed by the intermediate and high-contrast traces where this pre-pulse is significantly reduced. For these two other curves, a pre-pulse coming from the interplay between an etalon effect in a Pockels cell and the temporal Kerr effect [11] is present at −210 ps. No other significant pre-pulses could be diagnosed within the −300 ps to 0 ps window of the cross-correlator. In addition to the constant nanosecond ASE pedestal, the pulse profile exhibits a slow rise of the pulse intensity with a

#224082 - $15.00 USD Received 30 Sep 2014; revised 4 Nov 2014; accepted 5 Nov 2014; published 18 Nov 2014

1 December 2014 | Vol. 22, No. 24 | DOI:10.1364/OE.22.029505 | OPTICS EXPRESS 29507

slope factor of 5 per 10 ps between −100 ps and 0 ps, a feature which is typical for high-energy short-pulse laser systems. After amplification and compression, the short pulses are sent to the experiment chamber using the setup depicted in Fig. 1. The first dielectric mirror is a leaky mirror that transmits about 1% of the beam used for the shadowgraphy. This beam is first down-collimated to about 1-cm diameter with the help of an off-axis 90° copper parabolic mirror and a diverging lens. A set of reflective filters allows for controlling the pulse energy in the diagnostic beam-line during the alignment phase and the full-energy shot. We use frequency doubling with the help of a 1-mm BBO crystal to reduce the detection background due to scattering of the main pulse on the target. After a 50-mm delay-line the beam is sent to the target, whose interaction plane is image-relayed outside the chamber using a magnifying telescope. The F number of this imaging system is 7.5, a good trade-off between spatial resolution and sensitivity of the shadowgraphy setup. Indeed as explained below, a high F number is required in order to probe thin plasma clouds using shadowgraphy, while the small dimension of the pre-plasma requires an optical system with a reasonably small F number for spatial resolution purpose.

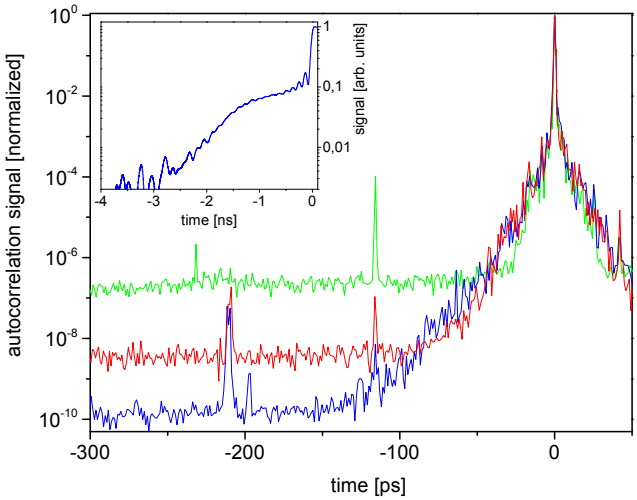

Fig. 2. Temporal profile of the PHELIX laser pulse for various adjustments of the contrast boosting module from standard (green) to intermediate (red) and high (blue) contrast levels. In the insert, a photodiode measurement of the nanosecond pedestal.

After entering the chamber, the main beam is reflected off a first turning mirror and finally focused with an f = 400-mm 45-degree off-axis parabolic mirror onto the target. Micrometer-thin copper targets were shot at an average energy of 47 J in 600 fs focused to a 4-µm spot (FWHM). Based on these values and a calibration of the focal spot image at low power the peak intensity was estimated at $2(\pm 1)\cdot 10^{20}$ W/cm^2 at the peak of the pulse. Flat 1-mm wide foils were used as targets for the interaction. The target thickness equal to 10 µm was chosen as a compromise to get the thinnest shadow on the shadowgraphy camera. Thinner targets did not give satisfactory results as they warped during mounting, increasing the effective thickness seen by the camera. During the shots, radiochromic films located in forward direction, perpendicular to the target, recorded the proton beam accelerated from the rear surface of the target. This additional diagnostic ensured that the expected intensities were reached. We measured maximum proton energies near 25 MeV, which is consistent with data reported in the literature for such an arrangement [12].

The timing of the diagnostic and main beams is crucial in this experiment. We used a fast photodiode (New Focus model 1454) together with a 8 GHz oscilloscope (Tektronix DPO70804) to simultaneously observe both main and diagnostic pulses, using the 10-Hz

#224082 - $15.00 USD Received 30 Sep 2014; revised 4 Nov 2014; accepted 5 Nov 2014; published 18 Nov 2014

1 December 2014 | Vol. 22, No. 24 | DOI:10.1364/OE.22.029505 | OPTICS EXPRESS 29508

front-end beam. By making several measurements for various time delays, a +/−10 ps accuracy in the relative timing could be achieved.

3. Experimental results

In the experimental campaign we took about 40 shots to characterize the pre-plasma formation for the three different ASE levels described above. For these shots the time delay of the probe beam with respect to the main beam was varied between −233 ps (before the impact of the main pulse at 0 ps) and + 100 ps. Each shot was preceded by a low-energy reference shot where the main beam was blocked and only the probe beam was used to illuminate the target. A selection of images which were obtained from shots with the highest ASE level is presented in Fig. 3. The upper row shows the reference images and the lower row the images with the main beam on target. The laser beam comes from the right. On these images, one clearly sees a shadow developing on the front side of the target which is due to the pre-plasma expansion. As the light pulse interacts with the target, ionization occurs at the target surface as soon as the intensity exceeds a certain threshold and the resulting plasma expands hydrodynamically into the vacuum. In such a case, the plasma density gradient is very high close to the target surface and decreases away from it. This plasma gradient deflects the rays of the probe beam crossing the plasma in a similar way to a diverging lens. When the gradient is strong enough, the rays exit the plasma at an angle higher than the opening angle of the imaging telescope and are not recorded by the camera. This non-illuminated area appears then as a shadow on the picture. It must be noticed that the plasma gradient does not allow measuring the position of the plasma critical density but rather plasma densities orders of magnitude lower.

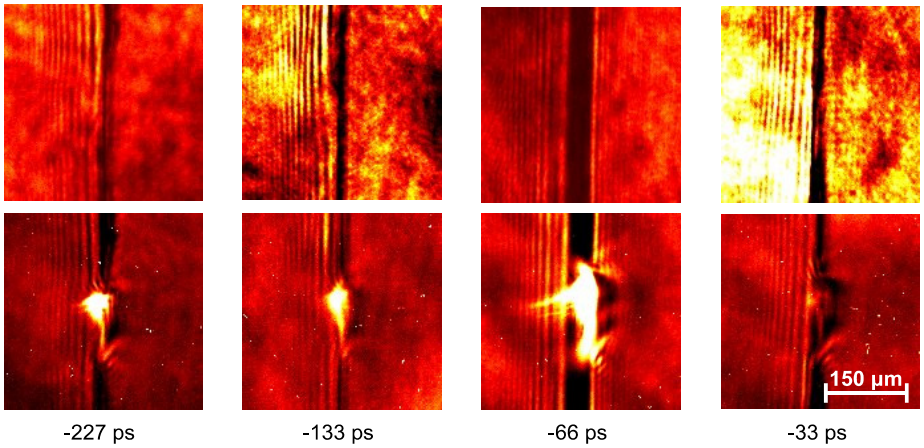

Fig. 3. Shadow images: reference image before the shot (upper row) and on-shot shadowgraphy images at various instants before the main shot for the highest ASE level.

On the images, one also notices a bright spot due to frequency-doubled light of the main beam. This is a known complication of shadowgraphy measurement at 2ω, but it did not affect the precision of the measurement. Here, we could reduce the magnitude of the spot by using perpendicular polarizations between main and probe beams, and a polarizer in front of the camera. The pre-plasma appears similar in shape and size for all time-delays between probe and main beams. At −227 ps the pre-plasma shadow is already well established with an extension perpendicular to the target plane of 38 µm, and stays rather constant up to −100 ps before the maximum of the pulse. For the other two time delays, the pre-plasma is slightly larger at 50 µm. The shape of the plasma shadow is also interesting because of its rather rectangular shape, indicating that the plasma expansion is stronger parallel to the target surface than perpendicular to it.

#224082 - $15.00 USD Received 30 Sep 2014; revised 4 Nov 2014; accepted 5 Nov 2014; published 18 Nov 2014

1 December 2014 | Vol. 22, No. 24 | DOI:10.1364/OE.22.029505 | OPTICS EXPRESS 29509

We repeated the analysis made above for all three ASE levels and at time delays before and after the peak of the pulse. The results are shown in Fig. 4. For the few hundreds of picoseconds ahead of the pulse, the pre-plasma shadow remains nearly constant. For the higher ASE level, the pre-pulse at −115 ps could be responsible for the slightly larger shadow at instants −66 ps, −33 ps and 0 ps. For the intermediate contrast level, the plasma shadow remains constant at about 20 μm. For the highest contrast level, no pre-plasma shadow could be measured. After the main peak of the pulse has been reached, the plasma expansion accelerates and the plasma shadow expands at a much faster rate. The vertical error bars in the measurement come mostly from the effective target thickness that creates an uncertainty on the interaction point, while the position reached by the shadow could be identified within a few microns. The targets exhibited various shadow thicknesses not correlated with their actual thicknesses because all targets warped somehow on their holders. A best +/– 5 micrometer accuracy of the measurement could be reached while other targets limited this accuracy to 30 μm. More sophisticated laser-cut targets and holders would be necessary to reduce this uncertainty to the micrometer level.

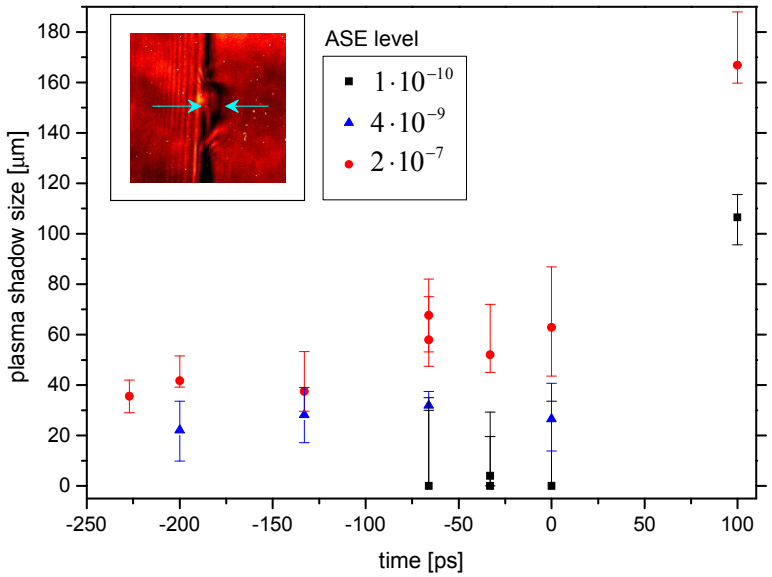

Fig. 4. Shadow size as a function of time. The zero delay corresponds to the maximum of the pulse intensity.

4. Interpretation and discussion

The images can be directly used to gain a qualitative understanding of the pre-plasma conditions. However in order to quantitatively explain this experiment, the plasma shadow must be interpreted in terms of plasma parameters, like position of the critical density and plasma temperature. Yet, the plasma shadow does not indicate the position of the plasma critical density but rather the location of a plasma density gradient characteristic of the numerical aperture of the measurement system. We used the 2-dimensional radiation hydrodynamics code RALEF-2D (Radiation Arbitrary Lagrangian-Eulerian Fluid dynamics) [7] to simulate our experiment. The code uses a second-order Godunov-like scheme on a structured quadrilateral grid and employs the arbitrary Lagrangian-Eulerian technique. Heat conduction and radiation transport in the plasma are taken into account, and the energy deposition by the laser is described by means of the inverse bremsstrahlung absorption, the dominant absorption mechanism for intensities below 10^{15} W/cm^2 [13]. The simulations were

#224082 - $15.00 USD Received 30 Sep 2014; revised 4 Nov 2014; accepted 5 Nov 2014; published 18 Nov 2014

1 December 2014 | Vol. 22, No. 24 | DOI:10.1364/OE.22.029505 | OPTICS EXPRESS 29510

performed assuming a cylindrical symmetry. The equation of state necessary for the simulations is described in [14] and the thermal conduction coefficient and spectral opacities have been generated by the THERMOS code [15].

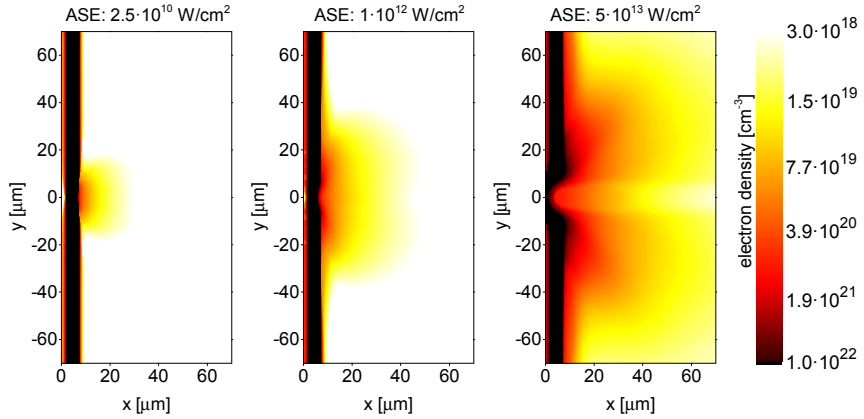

Fig. 5. Simulated electron density profiles for 3 ASE levels at $2.5 \cdot 10^{10}$ W/cm^2, 10^{12} W/cm^2 and $5 \cdot 10^{13}$ W/cm^2 (left to right).

The three ASE levels used in the experiment correspond to ASE intensities of $5 \cdot 10^{13}$ W/cm^2, 10^{12} W/cm^2 and $2.5 \cdot 10^{10}$ W/cm^2. The two-dimensional electron-density distribution obtained for the three ASE levels is shown in Fig. 5, where the simulated target is 5 micrometer thick and located between x = 2 and x = 7 µm. In the simulation, the laser comes from the right and illuminates the target with a linearly growing intensity for 1 ns and a constant plateau for the following 1.5 ns, to fit the experimental conditions as shown Fig. 2. The plasma cloud expands into the vacuum at different velocities and its shape changes with growing intensity. For the highest ASE level, one can see a plasma channel developing along the laser axis. This occurs because of the particular conditions of the laser-matter interaction, happening after the plasma has expanded during the initial irradiation phase, due to the fact that the ablated plasma expands perpendicular to the ablation front inside a crater. Our hydrodynamic simulations show that the radial component of the plasma velocity which is directed towards the channel axis in the vicinity of the crater is transformed into an axial plasma flow away from the target by interaction with the surrounding plasma. This leads to a well-defined plasma channel with a purely axial velocity. Due to the high velocity in the channel the density is lower than in the surrounding plasma plume.

Table 1. Comparison of simulated plasma shadow sizes and measured ones.

ASE intensity (W/cm^2)	$2.5 \cdot 10^{10}$	10^{12}	$5 \cdot 10^{13}$
Experimental shadow size (µm)	0 - 13	17 - 33	35 - 42
Simulated shadow size (µm)	5 - 6	10 - 15	29 - 38
Corresponding electron density (10^{20} cm^{-3})	0.7 - 1	0.4 - 0.7	0.6 - 1.2

The electron density in the plasma is responsible for the index of refraction seen by the probe beam. Rays propagate along the target surface and accumulate a phase that depends on their distance to the target surface. For electron densities small compared to the critical density, the absorption in the plasma can be neglected and the plasma can be approximated by a purely refractive medium. The total phase accumulated by the probe beam can be written in the form:

$$\phi(x) = \int_{-L}^{L} \frac{2\pi}{\lambda} n(x, y)\, dy . \qquad (1)$$

#224082 - $15.00 USD Received 30 Sep 2014; revised 4 Nov 2014; accepted 5 Nov 2014; published 18 Nov 2014

1 December 2014 | Vol. 22, No. 24 | DOI:10.1364/OE.22.029505 | OPTICS EXPRESS 29511

Where L is a distance large compared to the plasma extension, and n the spatially dependent index of refraction. For the rays propagating near the surface, the gradient of ϕ(x) along x becomes steeper and the rays exit the plasma at a large angle given by the gradient of the accumulated phase. For a certain value of $\nabla\phi(x)$, these rays are not collected by the imaging system and the area appears dark on the camera. In this approach, we used the thin-object approximation which is only valid for small gradients. This approximation is valid because the F number of the imaging system corresponds to a half collection angle of 3.8 degrees, well within the paraxial approximation.

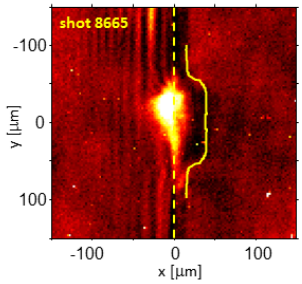

Fig. 6. Experimental (picture) and simulated (yellow line) plasma shadow extension for an ASE intensity of $5 \cdot 10^{13}$ W/cm^2. The dotted line shows the target position and the laser comes from the right.

We computed the ray positions corresponding to this maximum allowed deviation and reported them in Table 1, which shows the simulated plasma extensions together with the experimental data as plotted in Fig. 4. For the simulated data, the shadow size depends on the F number of the imaging system where an uncertainty given by alignment inaccuracies (mostly centering on folding mirrors) has to be taken into account. The simulated and experimental values are in very good agreement. The simulation predicts a significant plasma extension of many 10's of micrometers for the highest ASE level. This was detected and measured at the same level by our setup. For the lowest ASE level, a pre-plasma in the micrometer range is predicted but its extension is smaller than the detection accuracy of the setup. For the intermediate level, the experimental values exceed slightly the predicted values.

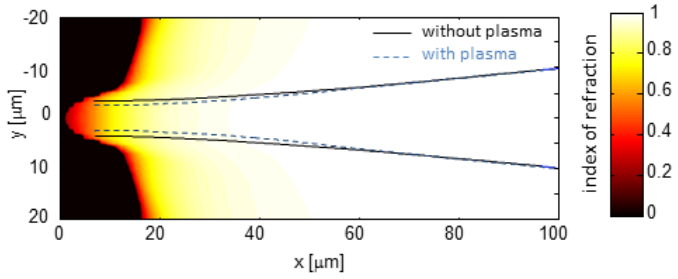

Fig. 7. Self-focusing of the ASE beam. The laser comes from the right and the background describes the index of refraction of the pre-plasma. Without plasma (yellow line), the beam focuses to a 3.4 µm waist, which is being reduced to 2.6 µm when the pre-plasma is considered.

The simulation also shows a plasma that deviates from the half-sphere geometry usually described in textbooks [13]. Here the shape is showing a lower electron density on axis when the ASE level is high, that can be explained by the geometry of the laser-matter interaction that takes place during the nanosecond-long interaction. In order to further compare the simulated and measured shapes of the plasma plume, we calculated the wavefront gradient at various Y positions along the target surface by rotating the electron densities given in Fig. 5.

#224082 - $15.00 USD Received 30 Sep 2014; revised 4 Nov 2014; accepted 5 Nov 2014; published 18 Nov 2014

1 December 2014 | Vol. 22, No. 24 | DOI:10.1364/OE.22.029505 | OPTICS EXPRESS 29512

This gives the shadow positions for all Y locations. This curve superimposed to the shadow image is presented in Fig. 6. We find again a very good agreement between the hydrodynamic simulation and the experimental measurement, not only in the X direction as reported above but also in the Y direction. This confirms the simulated plasma shape and the existence of a plasma canal created by ASE, only due to hydrodynamic effects.

The existence of a pre-plasma changes the index of refraction in the vicinity of the target and when this pre-plasma extends over many 10's of micrometers, it can in turn influence the propagation of the main beam. In order to test this hypothesis, we simulated in a first approximation the propagation of a Gaussian beam by numerically solving the Helmholtz equation in cylindrical coordinates for the radially varying index of refraction:

$$\left(\frac{\partial^2}{\partial r^2}+\frac{1}{r}\frac{\partial}{\partial r}+\frac{\partial^2}{\partial z^2}\right)E+\frac{\omega^2 n^2(r)}{c^2}E=0. \qquad (2)$$

The result is shown in Fig. 7, where a perfect Gaussian beam is focused with a 3.4 μm waist (5 μm full width at half maximum) at the target surface. As can be seen in the figure, the plasma acts like a focusing lens which induces a focusing of the beam. According to this simulation, an increase of the intensity by a factor of 2 is reached at the target surface. This effect can significantly influence the outcome of an experiment, as the main part of the pulse undergoes self-focusing by the same amount. A rigorous simulation should for each time-step include the heating enhancement due to the self-focusing, which in turn creates more self-focusing. However, this laser-propagation effect is not presently included in RALEF-2D.

5. Conclusion and outlook

In conclusion, we presented an analysis of pre-plasma generation during the interaction of ultra-intense laser pulses with solid targets for three different contrast levels ranging from standard (ASE intensity of $5\cdot10^{13}$ W/cm^2) to high contrast (ASE intensity of $2.5\cdot10^{10}$ W/cm^2). The used temporal pulse profiles are considered representative for common high-power laser systems, hence we believe our findings can be utilized for the interpretation of experimental results obtained at any laser facility. Using time-resolved shadowgraphy we can identify an extended pre-plasma for the lowest contrast which stays constant on the 100 ps timescale. With the help of 2-dimensional radiation hydrodynamic simulations, the measured shadow boundary whose distance perpendicular to the target surface is on the order of 30-40 microns, can be linked to an electron density around 10^{20} cm^{-3}. When changing over to the higher contrast levels, this shadow can be significantly reduced. For the highest contrast the pre-plasma is below the detection limit of our setup while the simulation reveals a minor plasma with a corresponding shadow dimension on the order of 5 microns. In addition, the 2-dimensional electron density distribution shows a remarkable feature: while for the higher contrast levels it is close to the half-sphere geometry which is typically described in literature, for low contrast shots it strongly deviates from such a shape. In fact, the lower electron density along the laser axis acts on the laser beam like a convex lens leading to an increase of intensity by a factor of two.

The pre-plasma defines the initial conditions for any experiment exploring the interaction of ultra-intense lasers with matter. Hence our results could contribute to a deeper understanding of physical processes happening in laser-generated plasmas. In particular, the plasma density distribution provided by this paper could be used as an initial distribution for numerical simulations of laser-plasma interactions. Starting with such a realistic configuration, instead of the steep density gradients which are commonly utilized could lead to much more realistic simulation results which could help to interpret experimental findings.

#224082 - $15.00 USD Received 30 Sep 2014; revised 4 Nov 2014; accepted 5 Nov 2014; published 18 Nov 2014

1 December 2014 | Vol. 22, No. 24 | DOI:10.1364/OE.22.029505 | OPTICS EXPRESS 29513

Acknowledgments

The authors want to thank the PHELIX team at GSI for their support and advice in the planning and realization of the experiment. This work was supported by the BMBF 05P12RDFA1 and the Helmholtz-Institute Jena. This work has been carried out within the framework of the EUROfusion Consortium and has received funding from the European Union's Horizon 2020 research and innovation programme under grant agreement number 633053. The views and opinions expressed herein do not necessarily reflect those of the European Commission.

#224082 - $15.00 USD Received 30 Sep 2014; revised 4 Nov 2014; accepted 5 Nov 2014; published 18 Nov 2014

1 December 2014 | Vol. 22, No. 24 | DOI:10.1364/OE.22.029505 | OPTICS EXPRESS 29514

Chapter 3

High spatial fidelity in laser amplifiers

High-energy high-intensity lasers aim at reaching the highest on-target light intensities required to explore the uncharted intensity territories lying within the relativistic regime and beyond. The intensity is a four-dimensional quantity that is based on two spatial dimensions, being theoretically only limited by diffraction, but in practice often by beam aberrations. A strong focus has been long put on the reduction of the pulse duration to achieve higher intensities but this possibility is nowadays more limited, since lasers are working close to the theoretical limit in pulse-duration. The energy is being also constantly increased but this is done at the expense of the beam dimension that becomes large and more sensitive to spatial distortions. This brings a renewed interest for working with beams of excellent focus quality, i. e. to keep operating lasers at the diffraction limit. As second motivation, working close to the damage threshold of materials requires a high level of control on the beam fluence distribution in the near field, while in the far field, modern experiments often require engineered intensity distributions to enable coherent control. A last point motivating the high spatial fidelity is the study of low amplitude signals and/or the search for applications, that benefit from a high average power. But the delivery of high-average power beams is only possible as long as this does not compromises the laser beam quality and trade-offs must be made.

So high-intensity lasers should not only deliver high quality beams with a high level of control but also high average powers. These are much more stringent requirements than for lasers used in other fields, and it explains why specific developments had to be made. In this chapter, I cover the aspects related high-fidelity spatial amplification where I made a personal contribution to the field, with the exception of the metrology aspects. High-performance metrology is an essential issue in high-power lasers where my group is particularly active at GSI. But it would deserve a dedicated chapter which I decided not to include in the manuscript. The first sections deal the beam control techniques with some unpublished results like the correct mathematical formulation of the serrated apodizer transmission and the sensitivity of Laguerre-Gaussian beams to aberrations. The second part introduces the effort made in the field to deliver high average-power laser beams.

3.1 Beam shaping and amplification distortions

3.1.1 Beam shaping in the near field with apodizers

Beam shaping is an aspect of growing importance for modern high-energy short-pulse lasers as the required beam shapes become ever more sophisticated as described in chapter 1 and shown in fig. 1.6

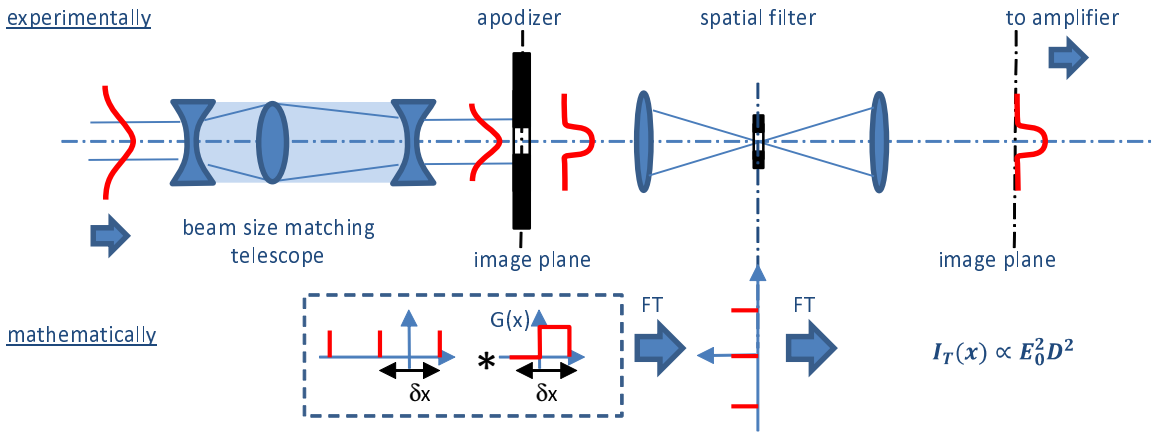

Figure 3.1: Principle of the beam shaping with transmission apodizers. The top sketch shows the experimental principle. The bottom part is the mathematical justification.

page 14. Already in the nineteen-seventies, alongside with the development of the first MOPA laser systems, it became clear that the natural Gaussian spatial profile of the beam was not optimal for high-energy lasers. At that time, rod pre-amplifiers could be found in systems like the Janus and SHIVA lasers [124] that were characterized by a very strong radial gain non-uniformity, the highest gain being found at the edge of the amplifier rods. A good mitigation step consists in seeding the amplifier with an apodized Gaussian beam and, at some point along the amplifier chain, the beam becomes "top hat" because the edges of the seed beam undergo a higher gain. Such a scheme faces two problems: first the exact beam intensity profile at the edge of the beam becomes important and must be tailored very precisely and second the tolerance on the beam centring in the rod amplifier becomes very small. At the OMEGA facility drifts and lack of precision in the alignment would result in so-called "donkey ear" or "figure of death" beams that were often discussed in the control room of the facility by the operation crew and that was notoriously a source of damage for the amplifier. For a report on the beam shapes of the early OMEGA amplifier, see ref [125].

To precisely control the edge of the beam, in particular the zero-energy point, and avoid diffraction ripples created by hard apertures, serrated apertures were introduced [126] and are still a major beam-shaping tool. The serrated apodizer can be used to shape a Gaussian beam into a beam with a well-defined zero energy point as shown in fig. 3.1. In this set-up, the combined use of a serrated apodizer with a spatial filter enables shaping the beam. In addition, a three-lens telescope can be used to adapt the size of the collimated input Gaussian beam to the apodizer dimension and obtain the right shaping effect. The serrated aperture introduces an amplitude modulation at the edge of the beam, usually by means of teeth, using either mechanically-made or etched elements whose duty cycle D is related to the required transmission. The theoretical formulation of the problem has been published by Auerbach et al. [126] but a calculation or typographical error is present so I think it is necessary to give the correct mathematical expression for the one-dimensional case as shown in the lower part of fig. 3.1. For the calculation, the input is a plane wave of amplitude E_0 (and corresponding intensity I_0) and the apodizer is one dimensional and infinite. It can be described by a transmission function that is applied to the incoming wave to give the transmitted field E_1:

$$E_1(x) = E_0 \left(III_{\delta x}(x) * G_{\delta x, D}(x) \right) \tag{3.1}$$

The transmission function is the convolution of G and III, where G is binary function describing the apodizer that accepts non-zero values for x belonging to $[-\delta x/2 , \delta x/2]$ with a duty cycle D

(defined as the integral of G over δx) and III is the Dirac comb function. In the focal plane of a telescope whose first lens has a focal distance f, the electric field distribution equals the scaled Fourier transformation of the field, where $\tilde{G}$ indicate the Fourier transformation of the function G:

$$E_1'(x) = E_0 \left(III_{\frac{\lambda f}{\delta x}}(x) \times \tilde{G}_{\delta x, D}(\omega = \frac{x}{\lambda f}) \right) \tag{3.2}$$

The spatial filter transmits only the field around the x = 0 point, so that the field after the pinhole $E_2(x)$ has non-zero values only at the origin with $E_2(0) = \tilde{G}(0)$:

$$E_2(x) = \delta \times \frac{E_0}{\delta x'} \int_{-\delta x'/2}^{\delta x'/2} g(x')dx' = E_0 D\delta \tag{3.3}$$

with δ the Dirac function. During propagation to the second lens of the telescope the field undergoes another Fourier transformation and we get as transmitted intensity:

$$I_T(x) \propto |E_T(x)|^2 \tag{3.4}$$

$$= I_0 D^2 \tag{3.5}$$

This result shows that the combination of the apodizer and spatial filter is able to modulate the intensity of the beam by D^2, and it is at the base of the amplitude mask definition strategy in laser amplifiers. For this to experimentally work, the pattern definition must follow two rules: at first, fine periodic structures should be used to ensure that no aliasing is introduced in the Fourier plane of the following spatial filter and secondly, the fabrication method should have the spatial resolution to minimize manufacturing errors. These two conditions are somehow contradictory and require some clever optimization.

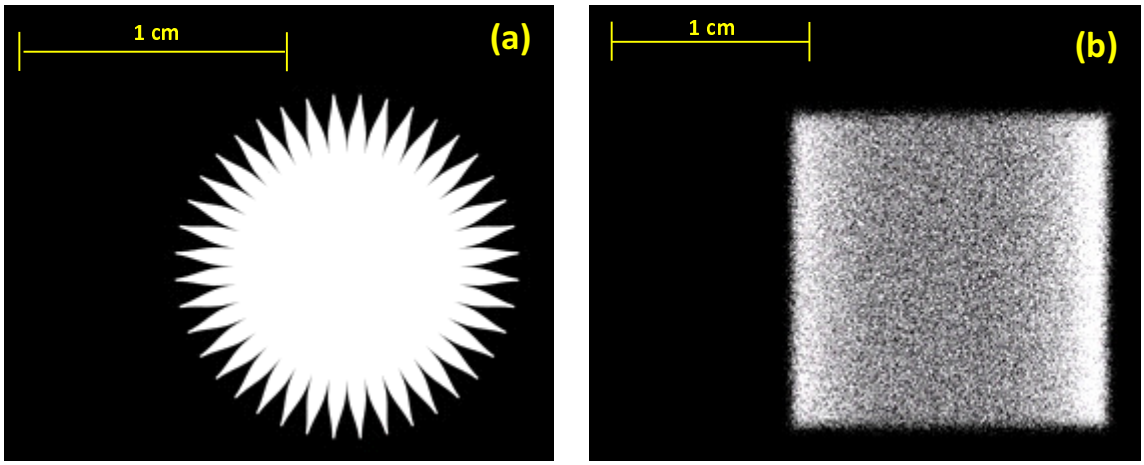

Figure 3.2: Binary beam shapers: (a) standard quasi one-dimensional apodizer, (b) dotted two-dimensional apodizer

An example of such an apodizer design for a round beam is given in fig. 3.2.a as used at the PHELIX facility. For this apodizer designed to shape 10-mm (FWHM) beams, 40 teeth defining the edge of the beam have been used. Because of the cylindrical geometry and the tooth aspect ratio, the condition for one dimensionality is respected. An interesting point to raise here is the choice of the mathematical description of the "top hat" transmission. While profiles are in the literature often super-Gaussian, the profile used for the edges follows an error function because such a function

allows for higher fill factors[1]. To come to this conclusion, one must compare two profiles in the view of a common criterion. The comparison criterion here is the modulation transfer functions (MTF) or encircled-energy function in the far field that need to be similar on a high dynamic range. In other words, two profiles are equivalent when diffraction effects induced by the edges are equivalent, as depicted in fig. 3.3. Following this, a beam defined by an error function has a 72 % theoretical fill factor, while the corresponding 10^{th} super-Gaussian beam only 66 %. In the case when a 20^{th} super-Gaussian profile is considered, the corresponding equivalent error function profile yields a 88 % fill factor, i. e. an increase of 6 % compared to the value in table 1.2. In other word, the error function allows for steeper edges but without additional diffraction effects.

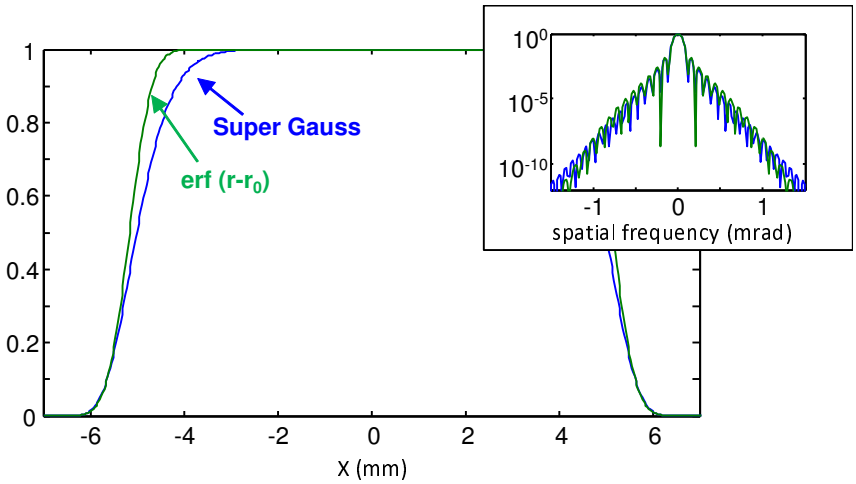

Figure 3.3: Near field profiles for a 10^{th}-order super-Gaussian (blue) and an erf(r-r_0) (green) beam. The erf beam has beam optimized to have the same transmission (99.96 %) and MTFs (in insert) as the super-Gaussian beam.

As far as manufacturing aspects are concerned, the transmission at the location of the teeth tips reaches 98 % for tips that are 5-micrometre wide, while the foot yields a transmission of 0.5 % for a void width of 70 micrometres. In both cases, this is well within the spatial resolution of lithographic methods while it represents a significant challenge for mechanically made apodizers.

Although it is desirable to work with "top hat" beams for energy optimization reasons, such a beam does not propagate very well and diffracts after some propagation distance. To avoid this, laser amplifiers working with "top hat" beams must incorporate some degree of beam image relaying.

However, a shaping of the beam edges might not be sufficient: for instance non-cylindrically symmetric amplifiers like slab amplifiers and also strong technical constraints (see for instance fig. 1.6.a and .c and [127]) require a complicated beam shaping that is truly two-dimensional, out of reach of a serrated apodizer. An evolution of the serrated apodizer design is shown in fig. 3.2.b, where a two-dimensional dot apodizer addresses both the beam edge definition and a non-uniform spatial gain that requires pre-compensation. For this apodizer design which I generated for the OMEGA-EP laser, small dots are inscribed on a substrate using lithographic techniques such that the dot density in a given area equals the square root of the required local transmission in accordance with eq. 3.4. Although the dot distribution might appear random, it cannot be done so because a random dot distribution contains also low spatial frequency noise that makes it through a spatial filter. For this reason, the distribution of dots is partially random but its Fourier spectrum shows

[1]The fill factor has been defined page 13

a fully deterministic profile around the zero-th frequency. Here a trade-off between pixel size that needs to be large enough to be made with accuracy and spatial resolution must be found and therefore optimization algorithms can also be used to improve the apodizer design [128]. With this technique, about any beam intensity profile can be made from a standard TEM_{00} beam profile by tailoring the transmission of the apodizer. The relatively low damage threshold of apodizers dictates that they be used in areas of low fluence only, early in the amplifier. Standard fabrication techniques include the step-wise coating of a bare substrate with a reflecting metallic coating, the layering of a photo-resist, the inscription of the mask features on the photo-resist and finally, the etching of the metallic coating. These many steps prevent in particular the use of complicated multi-layer dielectric coatings. The typical damage threshold observed varies from $100\,\mathrm{mJ/cm^2}$ for softer materials like chromium to $1\,\mathrm{J/cm^2}$ for aluminium at a wavelength of $1\,\mu\mathrm{m}$.

It is also possible to control the amplitude of laser beams by use of phase elements. I developed this idea in Rochester and demonstrated it with programmable spatial light modulators (see article page 87).The principle is mathematically close to eq. 3.1 for which we substitute G with a complex function H with an amplitude equal to 1 and a periodic step-like phase term of duty cycle 0.5 having values equal to $\varphi_0 + \delta\varphi$ and $\varphi_0 - \delta\varphi$. At the focus of a lens, one gets:

$$E'(0) = \frac{E_0}{\delta x}\int_{-\delta x/2}^{\delta x/2} H(x)dx \tag{3.6}$$

$$= E_0\frac{e^{i(\varphi_0+\delta\varphi)} + e^{i(\varphi_0-\delta\varphi)}}{2} \tag{3.7}$$

$$= E_0\cos(\delta\varphi)\,e^{i\varphi_0} \tag{3.8}$$

where the field amplitude is modulated by $\cos(\delta\varphi)$ and its phase equals φ_0. When a spatial filter is used, the out coming beam exhibits a modulation of its amplitude similarly to the dot amplitude apodizer. For a phase jump of π ($\delta\varphi = \pi/2$), the transmission equals zero while other values for the phase step offer a continuously controllable amplitude transmission. Phase elements do not absorb and offer an interesting alternative where the laser fluence is too high for standard amplitude apodizers [129]. In addition, the average phase level is conserved through the filter such that such a phase element simultaneously allows for controlling the phase and amplitude of the beam. While this technique works remarkably well, the depth of the blacks or zero-point transmission is finite and does not compare to the level achieved with amplitude modulation.

3.1.2 Laser mode shaping

Shaping a Gaussian beam into a "top hat" beam using apodizers is not very efficient from an energy stand-point. As long as the amplifier is based on amplification rods that require an apodized Gaussian-like spatial profile to compensate for edge effects, this is still tolerable but with slab amplifiers, this intermediate step does not happen any more and, the use of an apodizer can be lossy. As an example, the theoretical efficiency for carving a super-Gaussian from a Gaussian beam is of 57 % and 49 % for a 10^{th}- and 20^{th}-order super-Gaussian profile, respectively. For this reason, it is advisable to develop laser cavities that generate beam intensity distributions that deviate from the standard Gaussian spatial distribution. Hermite-Gauss beams are the natural solutions of laser cavities using spherical optics, because their phase is a sphere at all locations, which fulfils the condition on the end mirrors for stable mode oscillation. Another feature enabling Hermite-Gauss beams to be solutions of laser cavities is their self-similar character, i. e. the spatial fluence

distribution is a propagation invariant. However on the other hand, "top hat" spatial distributions are more interesting for laser amplification architectures but they are neither self-similar nor natural solutions of laser cavities because of complicated wavefront structures in the intermediate field that rule them out as solution of standard laser cavities.

Fourier-transform laser cavities are a first solution to the problem that were developed originally by Kermene et al. for the CEA in 1992 [130]. This cavity is made of two end mirrors located at the focii of an imaging element like a lens or a spherical mirror. Such a cavity is at the edge of the stability range and is fully degenerate. The laser emission from such a cavity is spatially multi-mode, only limited by spatial apertures located along the beam path. In order to get single spatial mode operation, a constraint is applied to the cavity: first with an aperture in the near field to enable the "top hat" operation, and second, with an engraved mirror with losses at the location of the zero-th intensity points for the cardinal sinus function or Bessel function for square or round "top hat" beams, respectively. Both elements constrain the cavity by imposing higher losses to the unwanted modes, which otherwise would have the same chance to oscillate. As a result, single spatial mode operation of the laser cavity can be obtained. A drawback of such cavity is that the beam size is limited: when a larger mode is necessary, its size in the Fourier plane decreases, the fluence on this mirror increases accordingly and damage can occur.

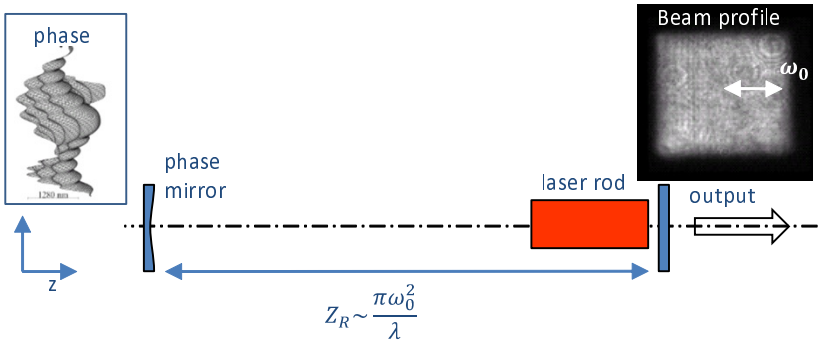

Figure 3.4: Laser cavity with phase-coupling mirror designed for "top hat" operation.

An improved solution capable of bearing higher mode dimensions is based on the use of highly mode selective cavities that include a phase-conjugating mirror, that is a mirror that introduces a phase exactly twice opposite to the phase accumulated during propagation [131]. In such a case, the condition for stable oscillation that requires that the beam distribution repeats itself after one round trip is fulfilled, because the beam propagates back to the initial shape corresponding to the phase engraved in the mirror. The principle of such cavity is shown in fig. 3.4 where one of the grade-phase mirrors that were developed during my time at CEA is depicted instead of the diffractive or refractive phase plate proposed by Leger et al. in their work [131]. I designed graded phase mirrors to generated both square or round "top hat" beams efficiently matching the amplification rod section. The phase mirror can be made by ion etching techniques on a curved mirror substrate in an iterative process dealing with stepwise layering of a photoresist and etching into the mirror. This technique is widely available and the most straightforward way to make the mirror or refractive element. It yields discrete 2^N-level phase plates in N iterations. However such a phase element accumulates fabrication errors and exhibits scattering losses at the step boundaries. In collaboration with the Institut d'Optique in Paris, we developed a better technical implementation that relies on the generation of a continuous (non-discrete) graded phase substrate that is later coated with a highly-reflective coating [132]. This technique is however limited to

cylindrically symmetric geometries, i. e. for round beams. In any case, this type of cavity works at best when its length equals the Rayleigh-distance of the required beam, that is with a cavity length of the order of a few meters for a half beam size around 1 mm. This way, the lowest-order mode in the cavity can oscillate with low losses while the higher-order modes are filtered out by the laser rod that plays the role of the aperture. As a result, high-energy single-mode "top hat" operation can be obtained as we demonstrated when I worked for the CEA in Bordeaux [133], where we built a regenerative amplifier delivering pulses in excess of 100 mJ. Later, my former colleagues even applied it to short pulse lasers [134]. A drawback of this design however, is that the graded-phase mirror is only matched to a given cavity length and mode size. Beyond the increased alignment complication, this reduces the flexibility of use, since one mirror per beam size is necessary in a similar way to the Gaussian reflectivity mirrors used for unstable resonators.

All in all, many beam shaping techniques exist to control the beam amplitude from the generation of custom fluence distributions to the more traditional beam intensity sculpting with apertures. It is however equally important to provide a control on the beam phase and here many techniques exist as described in the introduction, such that a modern laser system usually incorporates beam shaping and spatial phase control tools like deformable mirrors.

3.1.3 Active beam amplitude and phase control

To deliver beams with a fully-controlled amplitude distribution, static apodizers are only a first order solution because evolutions of the beam amplitude distortions (alignment drifts, change in gain) happen in time and the static method must be complemented by dynamic beam shaping techniques. Spatial light modulators (SLM) based on liquid crystals matrices have been known since many years and find applications in consumer electronics like in laser printers. SLM dedicated to high-intensity lasers and the manipulation of coherent-light beams are more complicated devices that need to fulfil the quality requirements (wavefront, uniformity) at a higher level, but they follow the same principle. SLM can be either used between crossed polarizers to introduce an intensity modulation by tailoring the amount of polarization rotation locally or they can introduce phase corrections being then an alternative to other active wavefront control devices like deformable mirrors [135].

A more powerful use of SLMs resides is the possibility to address both phase and amplitude with a single phase-only SLM as mathematically shown in eq. 3.8. The underlying idea is based on the superposition of a phase mask at low spatial frequency and a high-spatial frequency phase modulation that addresses the amplitude encoding. This was originally proposed by Kirk and Jones in 1971 [136] for computer-generated holograms but in the case of holograms the encoding is done in a Fourier-conjugated plane. For laser beam spatial control, the modulation with the SLM has to be done in the near field, which adds a complication. This is obtained by encoding the phase and amplitude information in the zero-th order and spatially selecting this mode with a spatial filter as shown for amplitude-only apodizers in fig. 3.1. The modulation effect is that of the equation 3.8, that is, an independent phase AND amplitude modulation. This idea has been developed first by Mindlovic et al. [137] but I proposed it at about the same time independently in our group in Rochester for applications with high-energy lasers. As demonstrated in the following article, page 87, phase-only SLMs can be exploited to get a spatial phase and amplitude modulation of the beam provided they offer a high enough spatial resolution. In the first attempt, the proof of principle was made but the precision achieved was not high enough for real-world applications because of several problems like linearity of the SLM device, precision in the phase measurement

and spatial registration of the beam on the device (alignment). Better performing devices are now available to address this problem and this has been exploited by my former colleagues to improve the beam shaping performance from the principle demonstration level to a much better level of control [138].

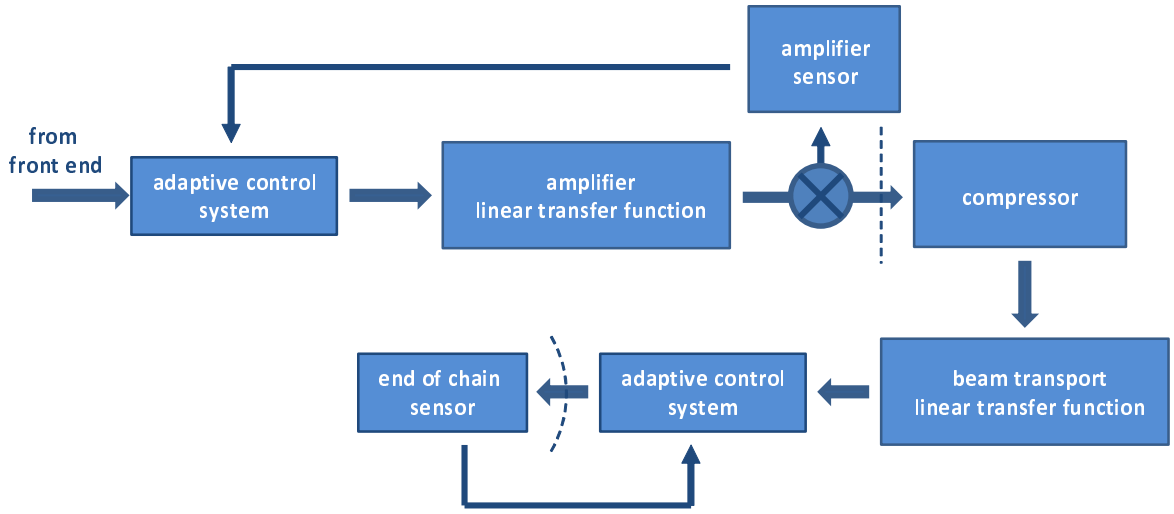

Figure 3.5: Principle of the beam wavefront handling in high–energy high–intensity lasers. The location of the adaptive control system is arbitrary and can be set at any location in the system, when its transmission function is linear.

Another field of application of the active beam control is the compensation of static or dynamic aberration happening in the laser system. Large laser system comprise many tens of components which introduce large metre-long amounts of materials and many interfaces. This is a source of beam distortion because of material non-homogeneities on one hand but also surface figure errors in the polishing (and coating) on the other hand. For CPA systems, it is crucial to ensure a flat wavefront at the entrance of the compressor to avoid deleterious spatio-temporal coupling effects as described in section 2.3.2 and also to create a perfectly spherical wavefront after the last focusing element of the laser system as depicted in fig. 3.5. For this, adaptive optics exploiting deformable mirror techniques first proposed in the nineteen-fifties [139] for astronomy and later demonstrated for civilian applications [140] in the early nineteen-nineties are employed in addition with high-performance sensors (e.g. Shack-Hartmann sensors). Fig. 3.5 shows a schematic view of the wavefront control strategy implemented at high-energy high-intensity lasers. The system can be divided in two sub-assemblies that find their interface at the entrance of the compressor. The first sub-assembly ensures that the wavefront is flat at the entrance of the compressor while the second takes care of the focus quality. The adaptive optics system must be located in the near field and at best at an image plane that is image-relayed throughout the system. In the schematics, the adaptive control system is located before the amplifier, possibly where the beam is smaller to save on implementation costs. But it could be located at the end of the amplifier or mid-way along it depending on the possibility of the hardware. The most commonly used device is the deformable mirror first patented in the USA in the nineteen-seventies [141] and later made commercially in the nineteen-nineties [142] whose surface figure is controlled by many tens of actuators. Actuators can be piezo-motors for fast response or stepper motors for in-vacuum use and larger pitch.

High-energy nanosecond lasers usually concentrate on the first sub-assembly [143, 144] because it is intimately linked to machine safety considerations, while the requirements on the focus quality

is not as stringent as for high-intensity lasers. In all cases, high-performance diagnostics aiming at emulating the wavefront of the laser at the targeted correction plane on the detector have to be implemented. This wavefront-sensor-based set of diagnostics must work during the alignment and calibration phases at high repetition rates and also at full energy to be able to measure on-shot wavefront data. The closed loop works as long as the transmission function of the system is linear in the sense of the propagation equations, i. e. the effect of hard apertures like pinholes can be neglected. Lower-order distortion like beam pointing or defocus should be compensated for by use of standard optical element like mirrors for tip and tilt and adjustable telescopes for defocus. Third- and higher-order aberration should ideally be handled by the deformable mirror up to the spatial frequency limit imposed by the vacuum spatial filters, which also means that the deformable mirror needs a number of actuator high enough to fulfil this requirement.

For high-intensity lasers, the emphasis shifts to the focal spot quality. Historically, titanium-doped sapphire lasers have worked at lower energies up to the joule and now the multi-ten joule levels. The beams associated with such amplifiers are small and non image-relayed during amplification such that it is possible to generate high-quality beams up to the later amplification and compression stages. And logically, the wavefront correction is done close to the target [145]. Unfortunately, there exists here some technical complications because of the higher requirements at the end of the laser chain, e. g. operation in vacuum and under high fluence close to the damage threshold. For high-energy high-intensity lasers both aspects become important such that beam correction before the compressor and close to the target becomes important [146].

In conclusion, adaptive beam control in high-energy lasers is the necessary step to ensure a high spatial fidelity during the amplification. Many tools exist in order to realize it with a high level of accuracy using both static and programmable beam shaping devices that can address both phase and amplitude simultaneously. Phase-only devices like SLMs are able to modulate the amplitude, too. But their dynamic range is limited because of the difficulty to get a full amplitude extinction. For this reason, static amplitude apodizers able to define the zero-point for the intensity profile have to be used in any case. Phase-only devices like deformable mirrors when used in conjunction with a high-fidelity wavefront measurement device can deliver distributed beam quality control systems to ensure the safe operation of the machine and reach focal spots near the diffraction limit.

3.1.4 Beam shaping in the far field

One of the wishes and actual requirements of modern high-intensity lasers is to prepare spatially engineered intensity distributions in the focus of the laser where some degree of coherent control is desirable. Long-pulse-duration nanosecond lasers have been used since many years to generate large “top hat” intensity distributions that are many orders of magnitude larger (mm) than the diffraction limit (usually µm) to drive quasi one-dimensional experiments [147]. In order to do that, random phase plates are used at or near the last focusing element to obtain this effect. When a phase plate alone is used, it generates the desired average fluence distribution but also a high spatial frequency speckle pattern that can compromise the interaction conditions. An evolution to the static phase plate design is the spatial smoothing technique by spectral dispersion (SSD) that requires modulating the pulse temporally to create spectral side bands and dispersing them spatially [148]. By doing so, the speckle pattern resulting from the interference of the many frequencies is evolving in time with a typical coherence length related to the spectral broadening applied. Thanks to this effect, a smoothing of the fluence distribution is obtained, enabling quasi one-dimensional interaction geometries used to launch planar shocks or compression waves for instance that are

useful for warm dense matter studies and ICF related research.

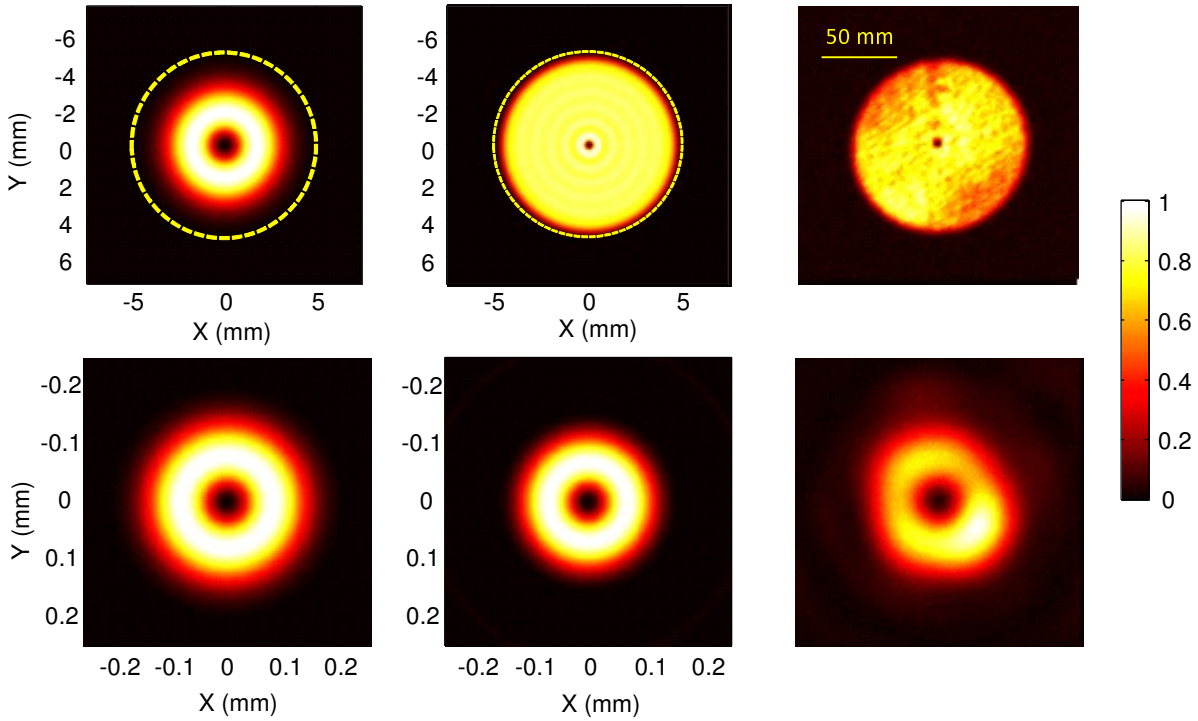

Figure 3.6: Near field (top row) and far field (lower row) intensity distribution of a $LG_{(0,1)}$ mode (left), a modified $LG_{(0,1)}$ mode (middle), and an experimental realization (PHELIX). The wavelength equals 1 µm in experiment and simulation.

For high-intensity lasers, the use of beam-smoothing phase plates is not advisable because ultra-high intensities well above the relativistic intensity threshold are sought after, which prevents distributing the intensity over too large a surface. In the last years, several theoretical articles underlining the advantages of employing "top hat" [149] or "donut-like" intensity distributions were published. In particular, beams with orbital angular momentum (OAM) could enable new interaction geometries [150]. At GSI, the possibility to create, transport and focus such exotic laser beams has been a subject of development in the last years in my group. Self-similar solutions of the electromagnetic field are good candidates because, regardless of their point of origin, they will propagate without damaging diffraction effects (intensity spikes) and focus without losing their characteristics. Self-similar beams can be in principle created in the front end of the laser where the small size and low fluence open many more opportunities and then, they can be magnified and amplified through the amplifier before being transported and focused onto the target. One of the lowest-order mode showing orbital angular momentum is best described by a Laguerre-Gaussian polynomial $LG_{(0,1)}$ in cylindrical coordinates (r,θ,z):

$$E_{(0,1)}(r,\theta,z) \propto \frac{r\sqrt{2}}{\omega(z)} e^{-\frac{r^2}{\omega^2(z)}} e^{il_{(=1)}\theta} e^{ik\frac{r^2}{2R(z)}} e^{-ikz+i\phi(z)} L_0(r), \quad \text{with } L_0(r) = 1 \tag{3.9}$$

where ω(z), R(z) and ϕ(z) are the beam waist, the radius of curvature and the Gouy phase at the position z along the propagation direction, respectively, and L_n is the n^{th}-order Laguerre polynomial. However, the fill factor (see table 1.2 for definition) of such a mode through an aperture

with a diameter equal to $4\,\omega_0$ is about 34 %, which compares to the 82 % for a 20^{th}-order super Gaussian fluence distribution. For this reason, it is interesting to generate an OAM beam, the spatial distribution of which exhibits a higher fill factor. In the front end of high-intensity lasers, there are many degrees of freedom that one can control to tailor the desired electromagnetic field distribution. Starting from the standard Gaussian beam distribution, apertures and phase plates can be designed to generate the desired beam fluence distribution. Fig. 3.6 shows a series of beam images in the near and far fields from theoretical predictions for a pure $LG_{(0,1)}$ mode (left) and a modified $LG_{(0,1)}$ mode (middle) to an experimental realization at the PHELIX facility. For the theoretical simulations, a 10-mm round aperture defines the pupil of the system (yellow dotted line) and the mode sizes are defined with respect to that aperture, such that the energy transmission through the aperture is larger than 99.5 %. For the Laguerre-Gaussian mode, this gives a waist of 2.5 mm. The far field images (bottom row) are obtained by numerically propagating the modes to the focus of a perfect lens with a 1-m-long focal length.

One clearly recognizes the self-similar character of the $LG_{(0,1)}$ mode as the spatial fluence distribution in the near field and far fields are identical. However, as stated above, the fill factor of such a mode is only 34 % and does not make an efficient use of the aperture from an energy stand point. A modified mode with OAM but a better fill factor as depicted in the middle column can be generated by combining a serrated aperture for the amplitude and an helicoidal phase element. This mode modification in the near field does not alter the far field that looks nearly identical in shape and size to a pure $LG_{(0,1)}$ mode, but the near field fulfils the requirement of a better fill factor. Here, little care has been given to the fluence definition near the phase discontinuity in the middle and this results in an additional intensity ripple near the center of the beam. In the experimental realization, the beam is measured at the output of the amplifier with an energy equal to about 50 joules and this ring structure is not present any more, being probably smoothed after the many spatial filters found in the amplifier section of the laser.

Aberration	"top hat" [151, page 531]	20^{th}-order Super Gaussian	Gaussian	modified $LG_{0,1}$
Spherical ab.	0.94	1.1 (+17 %)	1.3 (+38 %)	1.2 (+28 %)
Coma	0.6	0.7 (17 %)	1 (+67 %)	0.15 (-75 %)
Astigmatismus	0.35	0.4 (+15 %)	0.63 (+80 %)	0.05 (-86 %)

Table 3.1: Tolerance condition in λ units for several beams.

The far field image of the experimental realization in fig. 3.6 clearly shows the "donut"-like feature that is being sought after. However, the ring is somehow distorted and empirically, we found that the modified $LG_{(0,1)}$ mode seems affected by systems aberrations at a higher level than the standard TEM_{00} mode. To explain this observation, we conducted a series of simulations emulating the propagation of the beam from an initial aperture as defined above in fig. 3.6 to an ideal lens and then to the lens focal plane. The beam is defined on a 4096 x 4096 grid and propagated with the help of the Fresnel diffraction integral computed in the Fourier domain for CPU efficiency reasons [152]. In addition, to the mode definition, various amounts Seidel aberration can be added to the initial beam and the maximum intensity at the focus of the lens is being computed until the maximum intensity of the aberrated beam reaches 80 % of the un-aberrated beam in a Strehl ratio sense. The visibility of the aberrations has been discussed by Lord Rayleigh in the nineteenth century and later by Marechal around 1950 and their criterion is still being widely used nowadays [151].

However, the theory supposes a uniform illumination of the pupil with a plane wave, which is not the case for LG modes. The result of such simulations is shown in table 3.1 where the theory is compared to our findings.

Because the aberration magnitude is higher at the edge of the pupil, it is obvious that a beam with a centred peak-intensity distribution is less sensitive to the aberration, because the relative influence of the edge is weighted by a near to zero fluence. As compared to the theoretical values, the super-Gaussian beam is the one that is closest, a result that is also intuitive as the super-Gaussian profile is very close to a pure "top hat" distribution (second column in table 3.1). This result has been used in particular as a bench mark for our simulation model. For a Gaussian fluence distribution, the level of aberration that can be tolerated is significantly higher than for the "top hat" case for all aberrations, with astigmatism impacting Gaussian beams seemingly less.

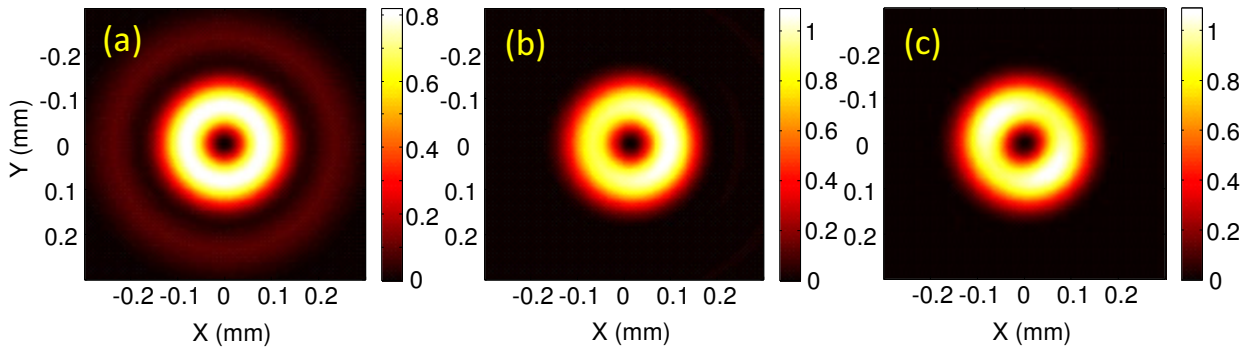

Figure 3.7: Fluence distribution of the modified LG mode for three aberration cases at the maximal acceptance criterion: (a) spherical aberration of 1.2 λ, (b) coma of 0.15 λ, (c) astigmatism of 0.05 λ.

For the modified LG mode, the situation is dramatically different. While the beam does not seem very sensitive to spherical aberration, being even more robust than the corresponding super-Gaussian beam used in the simulation, a strong distortion appears when off-axis aberration come into play. The criterion used for the analysis of the coma and astigmatism was a modulation of the fluence on the ring of 20 %, since a uniform distribution of fluence along the ring circumference in the focus can describe at best an un-affected beam. Fig. 3.7 gives the fluence distribution of the beam for the three aberration cases as given in table 3.1. The images are normalized to the peak fluence of the un-aberrated beam showing a reduction of 20 % of the peak fluence for spherical aberration and a modulation of 20 % of the ring fluence for coma and astigmatism. From this, it can be concluded that LG modes are much less robust and much more sensitive to system imperfections and misalignment. It should be noted also that the position of the beam shaping either in the front end or at the end of the amplifier does not play a role here since the aberration add to the helicoidal phase of the LG mode.

Nevertheless it is possible to generate, amplify and transport LG modes, making them available for applications at high intensities. When doing so, a great care has to be taken to the aberration in the system, in particular coma and astigmatism. As an application, the control of the angular distribution of proton beams generated by the interaction of a high-intensity laser with micrometre-thick foils in the TNSA regime has been explored with a certain success in my group [153]. Current work is in progress to improve the wavefront control at PHELIX to comply with the requirement of utilizing LG modes for even more demanding applications.

3.2 High average-power operation of amplifiers and beam fidelity

The two concepts in the title of this section are somehow in contradiction and probably one of the largest technical bottlenecks that lasers face. On one hand, experiments require high average power because many effects can be studied with a much higher precision when statistics can be made. This is particularly true for applications where simple targets like gas jets do not impose limits on the repetition rate. However on the other hand, heat is accumulating in laser materials working at high average power and thermal effects like stress-induced birefringence or wavefront distortion can ruin the laser beam quality. In the following, we cover two aspects of the operation of lasers in the thermally loaded regime: first the optimization of the amplifier and second the minimization of the thermal effects.

3.2.1 Heat deposition and thermal loading in laser amplifiers

From a power consumption stand-point high-intensity lasers have relatively low power needs, even when one takes into account their poor conversion efficiency. Indeed, thermally-induced effects limit the average output power and prevent running these devices at high average powers. To understand these limitations, it is necessary to keep a few basic principles in mind that explain why high-energy lasers are limited in their average power.

High-energy laser materials are all optically pumped and the heat deposition in the material is defined by the difference between the energy and number of absorbed photons to the number of photons available for radiative transitions. This is quantified by the quantum defect, i. e. by the difference between absorbed and emitted photon energies for optically pumped lasers, and the quantum ratio that defines the coupling efficiency of the absorbed photon to a radiative transition level. As shown in table 3.2, the resulting radiative energy to heat ratio will vary from roughly 1:1 for neodymium-doped glass pumped with flash lamps to 20:1 for Ytterbium-doped materials pumped with laser diodes. But in any case, a fraction of the total laser radiative energy is dissipated as heat in the material.

Material	Nd:glass, flash lamp pumped	Nd:glass, diode pumped	Ti:sapphire	Ytterbium, diode pumped
laser to heat ratio (%)	30 - 60	77	67	95
thermal conductivity (room temp.) W.m/K	0.57	0.57	33	1.4
thermo-optical coef. ($\times 10^{-6}$) 1/K	-4.7	-4.7	13	10
Saturation fluence J/cm^2	4.8	4.8	0.8	13

Table 3.2: Thermal properties of materials used in high-energy lasers. The data is given for the LG770 Nd:glass from Schott, and Ytterbium doped fibres.

When the laser material is under operation, a heat gradient is building between the pumped area and the areas where heat exchange is done with the outside. From this gradient, thermal stress and non-uniformity of the index of refraction are induced and can influence the quality of the laser beam. In the case of a laser rod uniformly pumped and side cooled, the thermal effect approximates

to a lens with focal distance f:

$$f_{th} = \frac{k_T}{QL}\left(\frac{1}{2}\frac{dn}{dT} + \alpha C_{r,\phi} n_0^3 + \frac{\alpha r_0 (n_0 - 1)}{L}\right)^{-1} \tag{3.10}$$

where k_T is the thermal conductivity of the material, Q the dissipated heat density, and L the length of the rod. Inside the brackets, there are three terms related to the change of index of refraction with the temperature (dn/dT), the stress-induced change in index of refraction (α is the expansion coefficient of the material and C the photo-elastic stress coefficient), and the temperature dependent length change of the rod (thick lens effect). The product QL is the areal dissipated heat density that is determined by the laser material and the amplifier operation conditions, which is closely related to the laser output fluence and repetition rate. k_T and dn/dT depend from the material and are influenced by the operation temperature.

3.2.2 Thermally loaded laser amplifiers of high quality

One of the ideas that motivated my PhD work was the propagation of laser beams in thermally loaded amplifiers [154]. At that time, alternative methods to reduce the thermal lens in titanium-doped amplifiers like cryogenic methods had not been developed yet and thermal lensing was seen as a bottleneck. At a one-kilohertz repetition rate and only considering the dn/dT effect, eq. 3.10 gives a focal length distance of 1 m, when one uses the parameters of titanium-doped sapphire operating at a dissipated areal power density equal to 500 W/cm^2, corresponding to a stored fluence close to the saturation fluence for that repetition rate. When working in such conditions, the beam undergoes a focusing effect for each pass through the amplifier and focuses along its path. A small focus can not only induce damage to the amplifier but self-diffraction is then stronger and the beam can additionally accumulate losses on aperture and the beam amplification and quality can be compromised.

However, this thermal lens effect can be used under some conditions as an imaging element that pass after pass compensates for the natural divergence of the beam, as explained in details in my PhD thesis [155] and in the article attached page 90. As the largest mode volumes throughout the amplifier also enable the highest energy throughput, it is necessary to understand the beam propagation in the thermally-loaded amplifier, for which the effect of the thermal lens on the laser beam is given by the Gaussian beam propagation equations:

$$Z_R Z_R' = f^2 + \sigma\sigma' \tag{3.11}$$

$$\sigma Z_R' = -\sigma' Z_R \tag{3.12}$$

where Z_R is the Rayleigh range of the Gaussian beam and σ the algebraic distance of the beam waist to the focal planes of the imaging lens. Eq. 3.12 implies that the product $\sigma\sigma$' is negative so the product $Z_R Z_R$' is maximized when $\sigma = \sigma' = 0$. The best conditions for the amplifier is then found when the input waist of the beam lies at the distance f from the first pass and the condition $Z_R = f$ ensures a stable mode imaging pass after pass. This imposes some upper limit to the energy that such an amplifier can reach. Indeed, the energy of the beam is then:

$$E = \pi\omega_0^2 F \tag{3.13}$$

$$= f\lambda F \tag{3.14}$$

where ω_0 and F are the beam waist and maximum fluence in the beam, respectively. For laser amplifiers, an output fluence around the saturation fluence of the amplifier material is typically reached, which gives for our application a maximum energy of 6 mJ for a titanium-doped sapphire amplifier operating at 1 kHz. In my experimental work presented in the article page 90, this value is exactly the output energy of the first amplifier that was built on this principle of stable pass-to-pass imaging. We also showed that it is possible to extend this scheme by a factor of 5 up to 30 mJ delivering a 30 W average power amplifier output but this also demonstrated the limit (see fig. 6 of the article).

Instead of using a thermal-lens-driven laser architecture, a better solution relies on wave guides like laser fibres that have been also proposed for high-intensity laser applications [156] and pioneered at IMRA America in Michigan in the last decade of the last century [157]. High-energy fibre lasers have many advantages for applications because of their high electric-to-output power efficiency and excellent thermo-mechanical properties [158]. In addition, direct laser-diode pumping with relatively low brilliance sources in double-cladding fibres enabled lowering the cost per watt of output average power dramatically. As an illustration the 100 W average power required to pump the high average power titanium-doped sapphire amplifiers cost about two orders of magnitude more than the equivalent in laser diode adapted to pumping ytterbium-doped fibres.

However, the maximum energy that a fibre can carry in a single ultrashort pulse is limited by the finite dimension of the mode sustained in the fibre. Recently photonic crystal fibres [159] or so-called "rod fibres" have been proposed as an improvement to the method because they enable mode dimensions above 50 µm. "Rod fibres" are a special type of very-large-mode-area fibre amplifiers that are characterized by a metre-scale length and mode sizes that are comparable to the modes obtained using the thermal lens imaging method described above. Because of the amount of material, the amount of fluence of a single pulse is limited to about 1 J/cm^2, which limits the energy of a photonic crystal fiber to the sub-millijoule level. Of course some optimization can be done but the energy of current photonic crystal fibres is limited to one millijoule [160]. Once the single-pulse energy limit is reached, an optimization aims at increasing the average power of such an amplifier because the limits imposed by the available pump powers and thermo-mechanical properties of rod fibre would allow kilowatt power operation [158]. The limit for high-quality beam operation of high-energy fibre lasers comes from the trade-off that has to be made on the spatial mode selectivity during the evolution from long single-mode fibres to short metre-scale rod fibres. Because a rod fibre has a large core, mode competition cannot be avoided any more, which a careful mode matching into the lowest spatial mode of the fibre amplifier enables to mitigate. However, mode competition is not suppressed and the excitation of higher-order spatial modes can be triggered via thermal effects, which has been reported in the literature as mode instability. This effect is considered to be driving the actual upper repetition rate limit for high-pulse-energy fibre lasers to about 200 kHz.

Another desirable feature of laser fibres is the possibility to coherently add them for enhanced performance and applications in physics in the relativistic regime. This prospect is being actively explored, motivated by the application potential of such an idea [49, 161]. But all-in-all, the laser systems able to work under high thermal load are only able to deliver millijoule-level energies. This comes from the simple condition that the thermal lens should not be significantly smaller than the Rayleigh distance of the laser mode at stake. For higher-energy lasers having beams of many centimetres and energies in the joule range, such a condition is not fulfilled at high repetition rates any more and the average power of such amplifiers is dramatically reduced.

3.2.3 Thermal load reduction strategies

As seen above, the thermal lensing effect can only be tolerated in laser systems that work with small beams. For high-energy, high-power lasers, thermal effects have to be minimized and impose their limit to the achievable repetition rate.

In side-cooled laser amplifiers where eq. 3.10 is valid, the minimization of the thermal lensing effects can be obtained by several mitigation steps aiming at increasing k or decreasing QL to reach a tolerable value for f. In general this limit value, defined as the maximum thermal lensing effect that a system can tolerate, will depend on the possibility to compensate for the thermal lens to the first order and the sensitivity of the beam of third order aberration (see section 3.1.4). Nevertheless it is possible to state as a general rule that a thermal focal length is tolerable when:

$$f_{th} \gg min(Z_R, L_c) \tag{3.15}$$

where Z_R is the Rayleigh distance associated with the laser beam and L_c the length associated with typical dimensions and optical elements in the amplifier. For high-energy laser amplifiers L_c is of the order of a few meters meaning that such lasers tolerate at best thermal focal distance of several tens of meters at most. A very long thermal focal distance is obtained with the following technical solutions:

- crystal vs. bulk. The first rule for high average power operation is the choice of a material that has a high conductivity and high laser-to-heat ratio. In such materials, the temperature gradients are lower and the resulting thermal lens less strong. On that matter, crystal based lasers have a great advantage compared to bulk materials because crystals have typically thermal conductivities one to two orders of magnitude better than that of bulk materials like glass. Unfortunately, crystals come only in modest sizes. A crystal that has excellent thermal properties is sapphire, which I used at a kilohertz repetition rate with 40 W of pumping power. Titanium-doped sapphire can be found in large dimensions (above 10-cm aperture). For the Mercury project [55], where strontium fluorapatite (SFAP) as host crystal for Ytterbium was chosen, the final amplifier crystals were obtained via optical bonding of high-quality single crystals and represented one of the largest technical challenges of that project. Right now, some efforts are made to explore the potential of calcium fluoride (CaF_2) that has a thermal conductivity around 10 W/m/K. Unfortunately ytterbium-doped materials in general and Yb:CaF_2 in particular have a very high saturation fluence (54 J/cm^2) requiring pumping power densities significantly higher than for other materials. As compared to titanium-doped sapphire, under equivalent pumping conditions aiming at working with pump power densities close to saturation, the thermal lensing effect is 200 times stronger in Yb:CaF_2 than in titanium-doped sapphire.

- Cryogenic temperatures. Lower temperatures have a positive effect on the thermal conductivity of materials and their thermo-optical coefficient. This technical aspect has been extensively explored for titanium-doped sapphire. Indeed, its thermal conductivity increases by approx. $\times 300$ between 300 K and 77 K, opening the possibility to run amplifiers at high energies and high-average powers simultaneously. In such a case however, transient effects cannot be neglected any more and the on-shot thermal lens is significantly stronger than eq. 3.10 yields because that equation supposes a time-averaged heat deposition [162]. But nevertheless, the decrease in thermal lens is such that the condition 3.15 is fulfilled even for pumping powers of 100 W (10 J, 10 Hz).

- Amplification with no heat deposition. Laser materials have various properties that make them more or less adapted to high power operation, with titanium-doped sapphire seemingly the most interesting one. However, parametric amplification might be a serious alternative because of the little absorption happening in nonlinear crystals. Optical parametric chirped pulse amplification (OPCPA) [56] enables building short-pulse 100-J-class laser systems [67]. The question is only about the average power that such an amplifier can handle. Table 3.3 gives an insight on the maximum allowed repetition rate when the condition 3.15 imposes a thermal focal length higher than 100 m. The comparison is interesting because titanium-doped sapphire and OPCPA both require nanosecond second-harmonic pump lasers. The absorbed pump energy density supposes an OPCPA working with $1\,\mathrm{J/cm^2}$ and a titanium-doped sapphire amplifier at $0.8\,\mathrm{J/cm^2}$, which are both fluences enabling a correct operation of the amplifier. The result shows that KD*P does not have a significant advantage compared to titanium-doped sapphire. Only crystals with very good properties and low absorption like LBO have an advantage over titanium-doped sapphire. Nevertheless, OPCPAs enable working at high average powers and at the sub-millijoule level, and they offer very promising possibilities when pumped with fibre lasers [163].

Material	Ti:sapphire	LBO	KD*P
absorbed pump energy density ($\mathrm{mJ/cm^2}$)	300	3	6
thermal conductivity (300 K) W/(m.K)	33	3.5	2
thermo-optical coef. at 300 K (x 10^{-6}) 1/K	13	10	-30
maximum repetition rate (Hz)	16	230	22

Table 3.3: Comparison of the thermal properties of Ti:sapphire and OPCPA crystals.

Given the limitations and solutions found for generating short pulses at the joule level and with a high repetition rate, the choice was made to develop an OPCPA as the front end for the OMEGA EP laser around the turn of the century. This is the time I chose and was the motivation for me to join this team. The OPCPA was first developed as a test-bed [164] to validate the energy fluctuation reduction concept proposed in the group [165] and later as stand-alone prototype integrated in the multi-terawatt laser (MTW) [166] and its OPCPA delivered energies in excess of 500 mJ at 5 Hz repetition rate with no signs of thermal lensing. This represents an average power of 2.5 W with beams of dimensions in the centimetre range, i. e. dimensions not compatible with operation under high thermal loading.

3.3 Peer-reviewed articles on the high-average power operation of short-pulse lasers

The articles selected in the following deal with the spatial fidelity of laser amplifiers. High spatial fidelity is concomitant to laser amplification development and has always received some degree of attention. Some development effort has been made to create laser beams that fulfil the requirements of the amplifiers (fill factor, gain compensation) while high spatial fidelity comes as a question in thermally loaded amplifiers or highly non-linear amplifiers like OPA's.

- V. Bagnoud and J. D. Zuegel "Independent phase and amplitude control of a laser beam by use of a single-phase-only spatial light modulator" Opt. Lett. **29** 3 pp. 295-297 (2004)

  This article describes the experimental demonstration of a beam shaping (phase and amplitude) method using spatial light modulators that became available at the turn of the century. At the Omega laser [1], round beams with nearly top-hat profile were made thanks to the interplay of static apodizers and a strong radial gain. While this is of little importance for ICF-relevant nanosecond pulses, the new beamlines of Omega EP included gain sections that were not cylindrically symmetric, exhibiting lower gains at the edge of the amplifiers. This seriously increased the requirements on the beams to be seeded in the amplifiers that had to be spatially pre-compensated for the spatially non uniform amplification gain. The new idea lies in the encoding method that superimposes high spatial frequency modulations for amplitude modulation to low frequency modulation for phase control. After this demonstration work, one found that SLM should be used only in addition to a high-dynamic range spatial modulator because the black levels achievable are not very high. This publication was followed by several of my former group that continued exploring the basic principle as explained in this article.

- V. Bagnoud and F. Salin "Amplifying laser pulses to the terawatt level at a 1-kilohertz repetition rate" Appl. Phys. B **70** [Suppl.] pp. S165-S170 (2000)

  This article summarizes the experimental achievement of my PhD. As it can be seen in fig. 1.4, high average power short pulse titanium-doped sapphire amplifiers were favoured in the mid 90's because the pump lasers offered this possibility. My PhD work has been the implementation on a large scale with 5 pump lasers (BMI S.A., France) of the concept of thermal-lens imaging that has been proposed a few years before by my PhD advisor François Salin. Thermal lens imaging is however not scalable as it works best when the thermal lens is of the order of magnitude of the Rayleigh distance of the beam. Nevertheless this experimental realization has set a record (1 terawatt at 1 kHz) that still holds in 2016.

- V. Bagnoud, I. A. Begishev, M. J. Guardalben, J. Puth, and J. D. Zuegel "5 Hz, >250 mJ optical parametric chirped-pulse amplifier at 1053 nm" Opt. Lett. **30** 14 pp.1843-1845 (2004)

  This article reports on the demonstration of a high average power short pulse laser being the prototype for the OMEGA EP front end. The laser amplifier was based on OPCPA pumped by a specially made pump laser (5 J, 5 Hz, temporally shaped) along the idea that OPCPA has very low thermal loading and that the OPA process does not affect the spatial phase quality. We could verify that even at this unprecedented high amplification level, the spatial phase quality of the beam was unaffected, while a decent uniform spatial amplitude could be achieved. The spatial uniformity is obtained for this system as long as the OPA is run at saturation. The main disadvantage is that the amplitude distortions grow exponentially when the pump modulation exceeds 20%. The prototype has been used without much change as front end for the OMEGA EP laser since 2008.

February 1, 2004 / Vol. 29, No. 3 / OPTICS LETTERS 295

Independent phase and amplitude control of a laser beam by use of a single-phase-only spatial light modulator

Vincent Bagnoud and Jonathan D. Zuegel

Laboratory for Laser Energetics, University of Rochester, 250 East River Road, Rochester, New York 14623

Received August 22, 2003

A phase-only spatial light modulator is used in conjunction with a spatial filter to provide independent control of the phase and amplitude of a laser beam. Continuous amplitude modulation of the beam is achieved with a resolution relevant to beam shaping of high-energy laser beams. Amplitude beam correction in a closed loop is demonstrated. © 2004 Optical Society of America

OCIS codes: 140.3300, 100.5090, 160.3710.

Laser-beam shaping is a rapidly developing field of research driven by both technological improvements of beam-shaping devices and the ever-increasing demands of applications. In high-energy laser chains, efficient beam shaping is successfully achieved in the front end by passive methods such as beam apodization[1] or intracavity mode shaping[2]; however, these static techniques are unable to correct dynamic laser-beam profiles caused by alignment drifts or thermal problems.

Spatial light modulators (SLMs) are versatile devices that can modulate the polarization or the phase of laser beams at high refresh rates. It has been demonstrated that a SLM can be used to compensate for the thermal phase distortion occurring in high-energy glass amplifiers.[3] Similarly, SLMs have been used in high-energy laser applications, such as intracavity beam shaping[4] or focal spot control.[5] In all these applications, only the phase-modulation capability of the SLM was used. However, a corrective device that would address both phase and amplitude simultaneously may be successfully used in high-energy lasers to significantly reduce the alignment procedure time, to improve the amplifier fill factor by injecting a more-adapted beam shape, to reduce the risk of damage in the laser chain by removal of hot spots, and to improve the on-target characteristics of the beam by better control of the phase.

Several techniques have been proposed to produce complex modulation of an electromagnetic field with a SLM for encoding computer-generated holograms.[6,7] In both cases, two neighboring pixels with a single-dimension modulation capability are coupled to provide the two degrees of freedom required for independent phase and amplitude modulation. In our work we use a similar approach, but our requirements differ from those of hologram generation. First, the number of modulation points across the beam does not need to be high because spatial filtering imposes a low-pass limit on the spatial frequencies allowed in the system. Second, a high-efficiency modulation process is required for minimization of passive losses. Lastly, the required amplitude-modulation accuracy should be better than measured shot-to-shot beam fluctuations for the correction to be fully beneficial.

In this Letter we propose a new method to modulate both the phase and amplitude of a laser beam with a single-phase-only SLM that uses a carrier spatial frequency and a spatial filter. As a result, the local intensity in the beam spatial profile is related to the amplitude of the carrier modulation, while its phase is related to the mean phase of the carrier. First, we show the simple relation between the transmitted intensity and the phase-modulation amplitude, and second, we experimentally verify this scheme and use it to demonstrate beam shaping in a closed-loop configuration.

The principle of the modulation is depicted in Fig. 1 for the case of a plane wave. The SLM is used as a phase-only device that applies a one-dimensional phase grating to the electric field. As a consequence, the two-dimensional propagation integral reduces to a one-dimensional one. In such a case, the electric field that is transmitted—or reflected—through the modulator accumulates a phase ϕ given by

$$E' = E_0 \exp[\, j\phi(x)], \tag{1}$$

where E_0 can be complex and ϕ is a periodic square phase modulation, of period Λ, oscillating between the values ϕ_1 and ϕ_2. After propagation through a lens, in an f–f configuration and under the Fraunhofer approximation, the electromagnetic field distribution at the focus of the lens is proportional to the Fourier

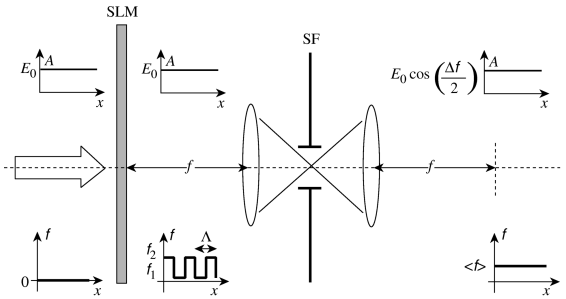

Fig. 1. Independent phase- and amplitude-modulation scheme. The input beam is modulated in phase by the phase-only SLM and then propagates through a spatial filter (SF). The SLM is placed at a focal distance from the SF lens so the electromagnetic field distribution at the SF pinhole is proportional to the Fourier transform of the electromagnetic field distribution at the SLM location.

0146-9592/04/030295-03$15.00/0

296 OPTICS LETTERS / Vol. 29, No. 3 / February 1, 2004

transform of Eq. (1). To calculate the Fourier transform of E', one can consider, for instance, the initial electromagnetic field as a sum of two square waves defined by

$$E_1 = E_0 \sum_n \delta(x - n\Lambda) \otimes \mathrm{rect}_{\Lambda/2}(x)\exp(j\phi_1), \quad (2)$$

$$E_2 = E_0 \sum_n \delta(x - n\Lambda) \otimes \mathrm{rect}_{\Lambda/2}(x - \Lambda/2)\exp(j\phi_2), \quad (3)$$

where δ is the Dirac function and $\otimes$ denotes the convolution product. After some algebra, the electromagnetic field distribution at the focus, given as the sum of the Fourier transforms of E_1 and E_2, can be written as

$$\tilde{E} \propto E_0 \sin c\left(\pi \frac{\Lambda\nu}{2}\right)\cos\left(\frac{\Delta\phi}{2} + \pi \frac{\Lambda\nu}{2}\right) \times \exp\left[j\left(\frac{\phi_1 + \phi_2}{2} - \pi \frac{\Lambda\nu}{2}\right)\right]\sum_n \delta(\nu - n/\Lambda), \quad (4)$$

where n is the spatial frequency and the Dirac comb function represents the diffraction pattern created by the SLM phase grating. Removing the higher-order terms ($|n| > 0$) in this diffraction pattern with a spatial-filter results in an electric field given by Eq. (5), where the amplitude is determined by the phase difference $\Delta\phi$, and the phase is equal to the average of ϕ_1 and ϕ_2:

$$\tilde{E}(0) \propto E_0 \cos\left(\frac{\Delta\phi}{2}\right)\exp\left(j\frac{\phi_1 + \phi_2}{2}\right). \quad (5)$$

This result is still true for finite beams, provided that the amplitude and phase of the initial beam vary slowly with respect to the modulation frequency. If the electromagnetic field spatially varies at higher frequencies, then the imaging system will act as a spatial filter and will modify the spatial distribution of light regardless of the application of a phase modulation on the SLM.

In the experimental setup shown in Fig. 2, the light source is a pulsed, 300-Hz laser, the beam of which is upcollimated so that it overfills the SLM area and is linearly polarized. It is reflected off the SLM and then imaged to an 8-bit CCD camera (Cohu 4910 series) or to a Hartmann–Shack wave-front sensor (Wavefront Sciences CLAS-HP). The camera was used mainly for system alignment and as a diagnostic or whenever high-spatial-resolution beam amplitude measurement was required. The wave-front sensor was used for simultaneous phase and amplitude measurements. We use a nonpixelated, 256-level, phase-only SLM from Hamamatsu (Model X8267) with a 20 mm × 20 mm active area, optically addressed by a 768 × 768 pixel LCD screen. Because of a slight defocus of the imaging system, continuous phase modulation can be achieved on the SLM at the expense of slight reduction of the resolution.

To be relevant to beam shaping in a high-energy laser facility, such as the OMEGA laser at the Laboratory for Laser Energetics, the passband of the beam-shaping spatial filter must be at least as large as the spatial filters in the main laser power amplifier, which are as large as 30 times the diffraction limit. To ensure removal of the SLM carrier spatial frequency, the minimum spatial frequency must then be at least 30 times the fundamental spatial frequency of the beam. Practically, this means that the minimum number of pixels required for that application is 60 across the beam (2 per period). The beam f-number in the spatial filter is 25, which means that the diffraction-limited focal spot is roughly 25 μm and the pinhole should be at least 750 μm in diameter. We used a 1-mm pinhole and a modulation frequency 64 times that of the fundamental beam frequency. In the SLM plane this modulation theory corresponds to a period of 12 pixels. For lower numbers of pixels per period, the finite slope between two nearby pixels degrades the modulation profile. For larger periods, up to 24 pixels, the beam is efficiently modulated by the SLM, but the system becomes more sensitive to the pinhole alignment.

Figure 3 demonstrates a linear amplitude-modulation scheme, as well as high-contrast and arbitrary spatial shaping. In the top part (around the lineout) Eq. (5) is inversed to obtain the phase-modulation amplitude corresponding to a linear amplitude modulation, while the bottom part of the image (below the lineout) shows nearly complete extinction for π-rad modulation and ~100% transmission when

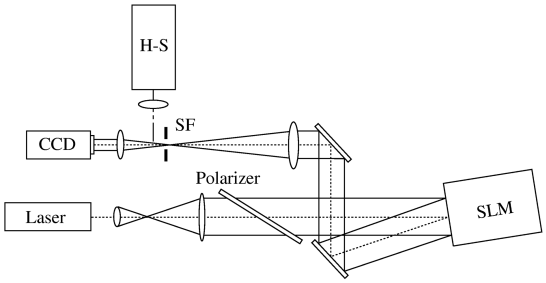

Fig. 2. Experimental setup: SF, spatial-filter pinhole; H-S, Hartmann–Shack wave-front sensor. The SLM is used in reflection and a flip-in mirror is used to measure either the intensity or phase profiles.

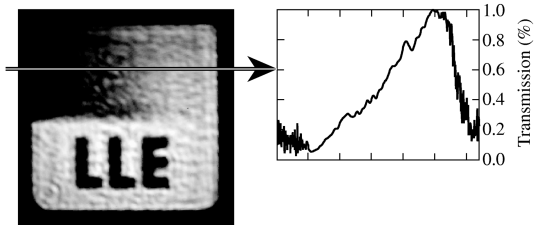

Fig. 3. A modulated beam demonstrates the amplitude control offered by the combined SLM–spatial-filter system. The lineout in the top portion demonstrates the effective transmission function, while the bottom part demonstrates high-contrast modulation with as much as 50:1 extinction ratio.

February 1, 2004 / Vol. 29, No. 3 / OPTICS LETTERS 297

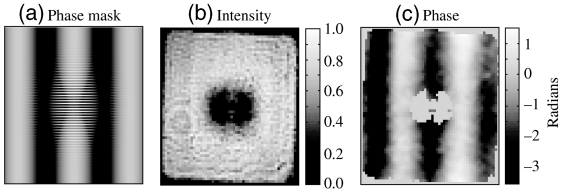

Fig. 4. Independent phase and amplitude modulation is demonstrated. The mask (a) leads to a beam that exhibits simultaneous amplitude (b) and phase (c) modulation.

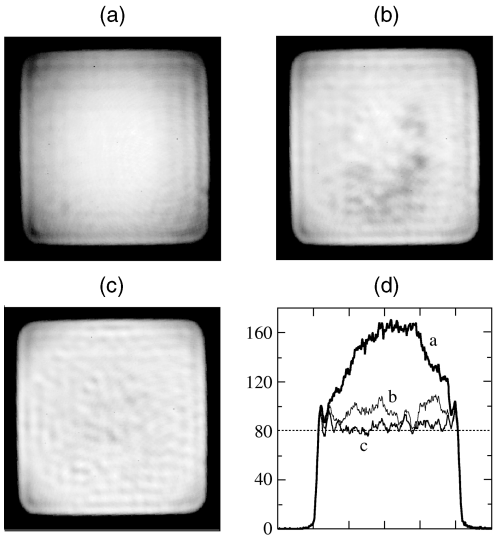

Fig. 5. Dynamic amplitude beam control. The initial beam (a) is shaped into top-hat beams (b) and (c). The lineouts in (d) show the typical error of the intensity goal.

the phase modulation is 0 rad. The low-contrast speckle shown in Fig. 3 limits the achievable extinction ratio that we measured varying from 50:1 to 10:1 across the beam. Note that extinction was achieved while only half of the dynamic range of the SLM was used (128 levels), which leaves at least half of the SLM dynamic range free for phase modulation, in the worst case.

Figure 4 demonstrates simultaneous amplitude and wave-front-shaping performance of this system by summing two one-dimensional patterns with spatial frequencies below and above the cutoff frequency of the spatial filter, as shown by the mask in Fig. 4(a). Figure 4(b) shows the beam amplitude measured with the Hartmann–Shack sensor, while Fig. 4(c) illustrates the measured wave front. Both images display data dropout near the center because the measured intensity falls below the detection threshold of the wave-front sensor. Little phase-to-amplitude coupling is observed, demonstrating that the phase information is conserved through the filter while intensity modulation is achieved.

Figure 5 illustrates the performance of this beam-shaping scheme in an iterative, closed-loop configuration. A single convergence scheme is applied in which less amplitude modulation is applied where not enough transmission is achieved and more where too much is measured. For demonstration purposes, we propose to correct the pixels for which the measured intensity on an 8-bit gray scale is higher than 80 counts. After mapping the SLM to the CCD by use of a fiducial image, the required transmission at each location of the SLM and the corresponding phase-modulation amplitude are calculated. The first step correction result is shown by the image in Fig. 5(b) along with its corresponding lineout, which shows that most of the correction factor has been underestimated since the average intensity is more than 80 counts. Similarly, the correction does not lead to a uniform beam because of the spatially dependent transfer function of the SLM. Nevertheless, the error, defined as the difference between the real intensity and the goal intensity, in a rms sense, for those points initially higher than 80, is reduced from 60% to 16%. Using the image in 5(b), we reduce the error signal by changing the modulation to achieve the goal. The result of a second correction is shown in Fig. 5(c), where the error signal has been reduced to 8.5%, which is dominated by the speckle noise discussed above.

We have shown a dynamic modulation scheme that addresses simultaneously both the phase and the amplitude of a laser beam. By modulating the phase of a laser beam at high spatial frequencies, one can couple the phase-modulation amplitude to the transmission of a spatial filter in a straightforward way. Following that, we have demonstrated that this scheme can be used for beam correction.

This work was supported by the U.S. Department of Energy (DOE) Office of Inertial Confinement Fusion under Cooperative Agreement DE-FC03-92SF19460, the University of Rochester, and the New York State Energy Research and Development Authority. The support of DOE does not constitute an endorsement by DOE of the views expressed in this article. V. Bagnoud's e-mail address is vbag@lle.rochester.edu.

References

1. J. M. Auerbach and V. P. Karpenko, Appl. Opt. **33,** 3179 (1994).
2. V. Bagnoud, J. Luce, L. Videau, and C. Rouyer, Opt. Lett. **27,** 337 (2001).
3. B. Wattellier, J.-C. Chanteloup, J. Fuchs, C. Sauteret, J.-P. Zou, and A. Migius, in *Conference on Lasers and Electro-Optics (CLEO 2001)*, Vol. 56 of OSA Trends in Optics and Photonics Series (Optical Society of America, Washington, D.C., 2001), pp. 70–71.
4. J. Bourderionnet, A. Brignon, J.-P. Huignard, A. Delboulbe, and B. Loiseaux, Opt. Lett. **26,** 1958 (2001).
5. B. Wattellier, C. Sauteret, J.-C. Chanteloup, and A. Migus, Opt. Lett. **27,** 213 (2002).
6. J. A. Davis, K. O. Valadez, and D. M. Cottrell, Appl. Opt. **42,** 2003 (2003).
7. P. Birch, R. Young, D. Budgett, and C. Chatwin, Opt. Lett. **26,** 920 (2001).

Appl. Phys. B 70 [Suppl.], S165–S170 (2000) / Digital Object Identifier (DOI) 10.1007/s003400000320

Applied Physics B
Lasers
and Optics

Amplifying laser pulses to the terawatt level at a 1-kilohertz repetition rate

V. Bagnoud, F. Salin

Centre Lasers Intenses et Applications, Université Bordeaux I, 351 Cours de la libération, 33405 Talence cedex, France
(E-mail: bagnoud@celia.u-bordeaux.fr)

Received: 15 October 1999/Revised version: 10 March 2000/Published online: 24 May 2000 –

Abstract. In this paper, we report on the realization of a 20-fs, 20-mJ laser chain operating at a repetition rate of one kilohertz. We emphasise the control on the pulse temporal and spatial profile, and its amplification at high average powers. This 1-kHz, terawatt laser is well suited for applications in high-field physics when low-intensity signal averaging is needed.

PACS: 42.55.-f; 42.65.Re; 42.60

Chirped pulse amplification [1] is a widely used technique for amplifying ultrashort pulses in bulk media to very high peak powers [2]. This technique has opened a completely new field of research in high intensity physics that appears for intensities about or greater than $10^{18}\,\mathrm{W/cm^2}$. Even with almost-diffraction-limited beams, terawatt peak powers are required to reach such a high level of intensity. These kinds of laser chains are good primary sources for X-ray lasers and ultrafast laser-induced plasma that have proved to be efficient sources of soft to hard X-rays. Ultrashort-duration X-ray sources are of great interest for numerous applications from imaging of biological samples in the water window to probing atomic arrangements for example. Broadband gain medium such as titanium-doped sapphire made it possible to generate and amplify laser pulses in the sub-100 fs domain. This leads to laser chains that only need to deliver several tens of millijoules of energy per pulse to reach the terawatt peak power regime. A low pulse energy makes the laser more versatile and reliable and allows it to fit on a small foot print.

Up to now, multiterawatt laser chains have only been demonstrated at a repetition rate of 10 Hz [3–5], and their average output power is generally in the watt range. Most applications that can be developed out of femtosecond lasers or laser-induced secondary sources will benefit from higher average powers, which means higher repetition rates. Several groups have started to work on high-intensity high-repetition-rate systems [6, 7]. They have reported the use of Ti:sapphire for amplification of sub-30-fs laser pulses to the 0.1-TW level at a 1-kHz repetition rate. Indeed, working with sub-30-fs pulses makes it possible to reach the terawatt level at lower energy. Although this increases the constraint on the spectral phase and amplitude control, it is clearly beneficial in terms of cost. Furthermore, phenomena such as high-order harmonics generation [8] will also benefit from shorter pulses [9, 10]. Eventually, we set the goal for our terawatt system at 20 fs and 20 mJ per pulse, while keeping the 1-kHz repetition rate. First, this paper describes the experimental implementation of our terawatt kilohertz system and then it focuses on more specific issues that had to be solved in order to keep the quality of the pulse good enough to be used in a real high-field physics experiment.

1 Experimental setup of the laser system

Ultrashort seed pulses are produced by a home-made Ti:sapphire fs oscillator that runs at 78 MHz. A 4.5-mm-thin crystal, together with a fused-silica prism pair allow generation of pulses as short as 10 fs, with a 220-nm bandwidth centered at 800 nm. The laser oscillator is pumped by 3.8 W of green light produced by a Nd:YVO_4 Millennia laser (Spectra Physics). The pulses whose energy is about 2 to 3 nJ are then sent to our CPA system.

A schematic of the terawatt amplification chain is described in Fig. 1. The beam is first sent to an aberration-free Öffner-triplet-based stretcher [11] which temporally stretches the laser pulses to several hundreds of ps. The mirrors in the stretcher have a radius of curvature of 1 and 0.5 m and their diameters are 300 and 120 mm, respectively. Such large optics ensure a spectral bandwidth broader than 150 nm. This is necessary to avoid spectral clipping which would introduce wings on sub-20-fs pulses. Great care has been taken in manufacturing these mirrors as the surface qualities are $\lambda/34$, $\lambda/90$, and $\lambda/80$, for the primary, the secondary, and the roof prism mirrors, respectively. The grating in the stretcher has a groove density of 1200 lines per mm and the angle of incidence is 22°.

The pulses are then sent to an amplifier consisting of a regenerative pre-amplifier followed by three multipass amplifiers. Most of the gain in energy is provided by the regenerative pre-amplifier. The seed pulse is sent to an X-shaped laser

S166

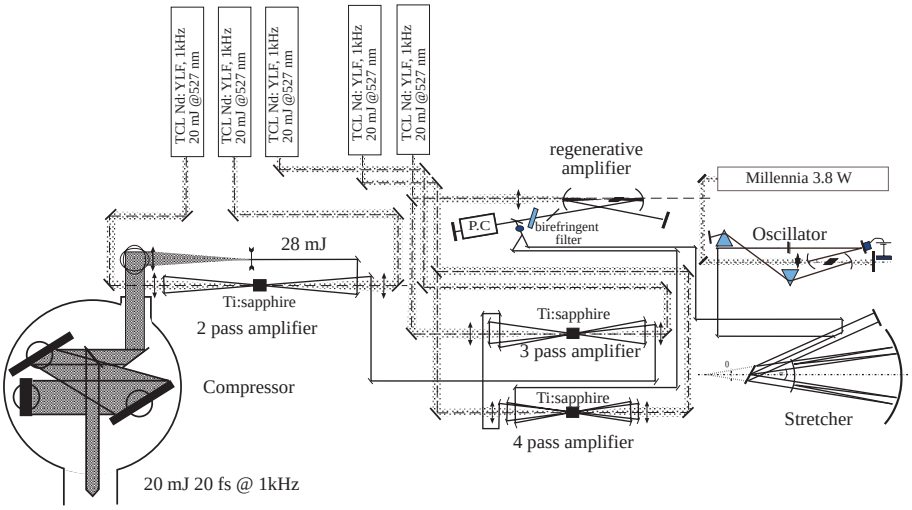

Fig. 1. Experimental setup of the terawatt kilohertz laser

cavity where it undergoes an amplification factor of about 10^6. The 7 mJ pumping energy is focused onto a 10-mm-long Brewster-cut Ti:sapphire crystal providing a small signal gain of about 4 per round trip. One of the benefits of regenerative amplification is to reshape the laser mode to a pure TEM00 cavity mode albeit exhibiting a slight astigmatism. Astigmatism arises from both the astigmatic thermal lens in the pumped area which is dissymetric because of the Brewster angle of the Ti:sapphire crystal and the geometry of the laser cavity. A second feature of regenerative amplification is that the saturation fluence is hardly ever reached. This means that the ASE background sees the same gain as the main pulse, and therefore the initial contrast ratio is kept over the 7 orders of magnitude amplification process. This contrast can be enhanced thanks to mode matching seed beam and cavity mode. Not only does this method efficiently seed the regenerative cavity but the ratio between spontaneous emission and seeded energy is increased. We estimated the ASE to pulse peak power by comparing the build-up time of both signals and we found a value around 10^8. A third feature of the regenerative amplifier is its gain narrowing [12] which is stronger than in a multipass pre-amplifier. Indeed, spectra broader than 30 nm can hardly be expected from usual regenerative cavities. We use a 580-μm-thick birefringent filter [13] to create spectrally dependent losses in the cavity in order to broaden the net gain (by reducing the gain at its maximum, around 800 nm). With this filter, we routinely get spectra that are more than twice broader, corresponding to a theoretical pulse duration between 15 and 20 fs. The last feature of the regenerative amplifier is the output pulse energy. Since thermal aberration in the Ti:sapphire crystal destorts the pulse spatial profile, the energy was limited to 1.5 mJ to keep the beam diffraction limited.

Power amplification is performed in three different stages of multipass amplification. The pumping energy is produced by five, 20-mJ, YLF lasers (Thomson CSF Lasers) running at 1 kHz. The high pump average intensity ($4\,\mathrm{kW/cm^2}$) in the amplifier Ti:sapphire crystals induces a strong thermal load which leads to a thermal focal distance of about 1 m. In order to avoid strong beam distortions, we use the thermal lens imaging technique [14] to successfully relay the beam waist in the amplifier from one folding mirror to the other. As the laser and pumping energy increases, the size of the pumped area in the crystal increases too. As a consequence, the length of the amplifier becomes too long and the laser fluence on the folding mirrors too high. Eventually, pure eigenmode relaying is not experimentally possible in the last amplifier and we adopt a different amplification strategy where the laser beam is collimated between the two passes and undergoes strong focusing before and after the amplifier. In each amplifier, the small signal gain per pass is equal to 3. In the first amplifier, we need 4 passes to extract 30% of the pump energy. This brings the pulse energy to 7 mJ. The eigenmode relaying technique works particularly well and it is very easy to implement although it requires mode matching between the regenerative cavity and the entrance mirror of the amplifier. We use 30 mJ of energy to pump the crystal of the second amplifier and three passes are needed for extraction of 28% of the energy. Mode coupling is performed between the two first multipass amplifiers using a single lens. The crystal of the last multipass amplifier is pumped by two 20-mJ YLF lasers, one on each side. Because, the laser fluence on the folding mirrors would be too high, we use a configuration where the laser beam is focused before its first pass. Then the beam is collimated by the thermal lens and its fluence on the folding mirrors remains below the damage threshold. Because we only need a saturated gain of 2, extraction is easier and the extraction efficiency is 32%. A summary of the above-described amplifier performances is given in Table 1.

Temporal compression of the laser pulses is achieved in a two-grating Treacy-type compressor [15] used in a single-pass configuration. The gratings have a groove density of $1480\,\mathrm{l/mm}$, and they are recorded on a $\phi = 15$ cm BK7 sub-

Table 1. Performances of the three multipass amplifiers used in the laser chain

Amplifier	4-pass	3-pass	2-pass
Pump energy/mJ	20	30	40
Output energy/mJ	7	15	28
Extraction efficiency	30%	28%	32%

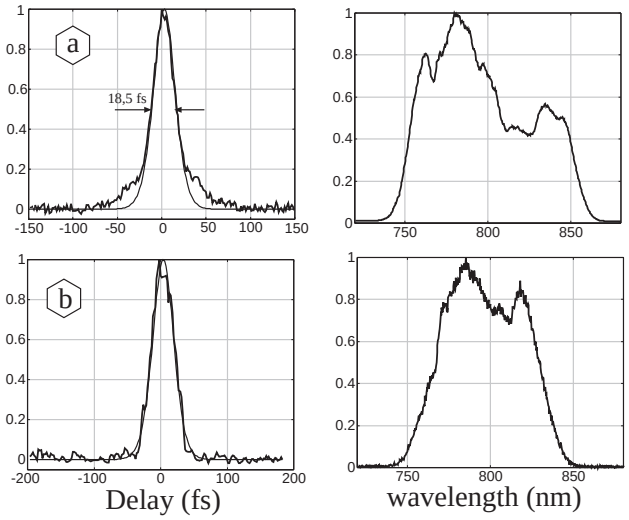

Fig. 2a,b. Intensimetric SHG autocorrelation of the amplified pulses and corresponding spectra. **a** Best results basis. **b** Somehow longer pulse but with a cleaner temporal profile

strate. The angle of incidence on the compressor grating is about 45° and the compressor distance about 38 cm. The beam diameter is 3 cm in diameter so the average intensity on the grating remains below 3 W/cm^2. Due to the very high output peak power, compression is performed in vacuum. The use of gratings with different groove densities in the stretcher and in the compressor ensures spectral phase matching between the stretcher and material on one hand and the compressor on the other hand [16]. The compressor throughput is about 70%, leading to compressed pulse energies as high as 20 mJ. Duration measurements of the laser pulses have been performed using a SHG intensimetric autocorrelation. We obtained pulse durations as low as 18.5 fs assuming a $sech^2$ temporal profile. The autocorrelation, together with the pulse spectrum are presented in Fig. 2. This autocorrelation was performed using a 10-μm-thick type-I BBO crystal. Routinely, it is possible to get pulses exhibiting no wings at the expense of slightly longer durations. The second autocorrelation trace in Fig. 2b shows a slightly longer pulse but without pedestal. In this measurement, the non-linear medium was a plate of poled fused silica [17].

2 Amplification of sub-20-fs pulses: issues and solutions

Although propects in interaction with ultrashort pulses are very promising, amplifying sub-20-fs pulses is also meaningful from a point of view of the average power: the shorter the pulse, the lower energy per pulse to obtain 1 terawatt. Since the final pulse duration is ultimately limited by the pulse bandwidth, the foremost condition in amplifying ultrashort pulses is to keep the width of the laser spectrum. This means that the gain needs to be spectrally constant, over a band broader than the pulse spectrum, in order to linearly amplify all the laser pulse frequencies. This is not generally true, and only amplification of 40-fs and longer pulses is possible in Ti:sapphire. Yet, shorter pulses undergo the effects of gain narrowing which must be cancelled to amplify sub-30-fs pulses.

Since this phenomenon is only due to the spectral gain, one only needs to overcome spectral gain narrowing in the pre-amplifier, where this effect is the most important. Different approaches have been proposed to this problem. First it is possible to spatially decouple the different wavelengths and shape the pump beam profile to flatten the spectral gain [18]. A second method would use multilayer dielectric mirors with a reflectivity that matches the spectral gain in the cavity so that the net gain would remain spectrally constant over a broader spectral range. Another method, is called regenerative pulse shaping, where spectrally dependent losses are introduced in the pre-amplifier, has been more exhaustively studied [4]. Spectral losses can mainly be obtained from interference (Fabry–Perot filter) and polarization effects (Lyot filter). Even if amplification of ultrashort pulses has been done using Fabry–Perot filters, the use of a birefringent filter is much simpler and less sensitive to thermal and mechanical drifts. The birefringent filter is made by a birefringent plate located between two polarizers. The transmission of such a filter depends sinusoïdaly on the laser frequency. The filter parameters (orientation and thickness) can be chosen so that the losses introduced by the filter matches at best the spectral gain of the cavity. In such a case, the net gain in a pre-amplifier including the filter can be flattened. Figure 3 plots three different spectra measured at the output of the amplifier. The natural gain bandwidth of Ti:sapphire leads to the dotted line spectrum that correspond to a theoretical Fourier-transform-limited pulse duration of 33.5 fs. The two other spectra were obtained from a regenerative amplifier including a birefringent filter. The corresponding theoretical pulse durations, calculated as the Fourier trasform of the corresponding spectrum, are 19.8 fs and 17 fs for the solid-line and dashed-line spectrum, respectively. Note that such a filter can also be used to tune the laser central wavelength from 700 to 900 nm while keeping a relatively short pulse duration of about 100 fs. Interference filters can lead to somehow better results in terms of pulse duration [19]. However, the use of an étalon is more sensitive to drift than the birefringent filter, and its alignment is more complicated. Both systems allow us to amplify sub-

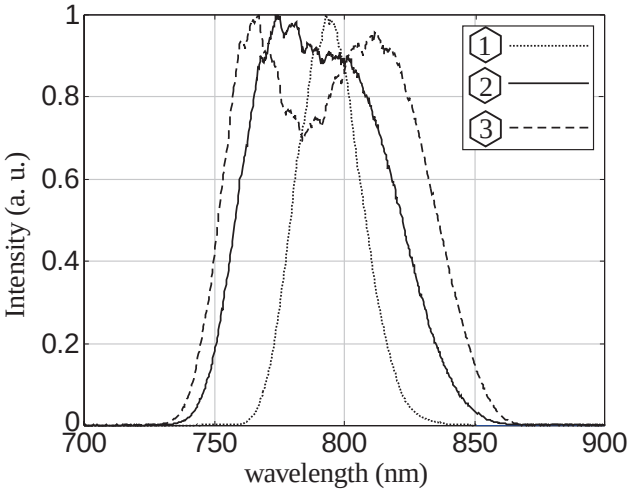

Fig. 3. Experimental spectra measured at the output of a regenerative amplifier. The *dotted line* (1) spectrum is a typical spectrum compared to two other spectra (2 and 3) obtained by use of a 475-μm-thick birefringent filter

20-fs pulses and it appears that the ultimate limitations in ultra-broadband amplification arise now from the coating's spectral bandwidth.

The second concern to be taken into account in amplifying ultrashort pulses is the spectral dephasing of the CPA laser chain. The condition for good compression implies that the dephasing accumulated after propagation through the stretcher, the amplifier and eventually the compressor should be as close as possible from a linear function of the frequency.

In a typical laser chain including a regenerative amplifier, there is about 1 to 2 m of material that introduces a strong group velocity dispersion (GVD). Therefore, it is relatively difficult to compensate for the phase mismatch between the stretcher and the material on one hand, and a compressor with only two degrees of liberty (angle and distance) on the other hand. In such a case, we calculated that the use of mixed grating [20] (the stretcher and compressor gratings groove densities are different) together with global optimization [16] could lead to a system where the total dephasing remains within 0.1 radian from the expected ideal value over a range of 100 nm.

However, spectral phase measurement at the output of a laser chain using SPIDER [21] for instance often shows a pulse spectral phase which is different from that expected from the simulations. Surface defects on the stretcher optics are mainly responsible for this unpredicted residual phase. In our case, we use a Öffner-triplet-based stretcher [11], which utilizes a 30-cm-wide primary mirror and a 12-cm secondary mirror. Even though the surface quality of our optics is very good, the $\lambda/34$ primary mirror in our stretcher was found to introduce a dephasing, as shown on Fig. 4, and we have shown [22] that the optical element with the lowest quality will dominate this phenomenon.

A comparison between this experimental phase and the calculated theoretical phase presented in dotted line on the Fig. 5 shows that the dephasing due to the non-perfect surface quality of the stretcher mirrors is larger than the dephasing calculated from the mismatch between the compressor and amplifier dispersion. This means that the dephasing at the output of the laser chain will be driven by optical defects on the stretcher optics. As a consequence, much care should be taken to minimize this by use of the best quality optics. During the definition of the amplification scheme, one must balance theoretical dephasing, which can be small as seen in Fig. 5, and

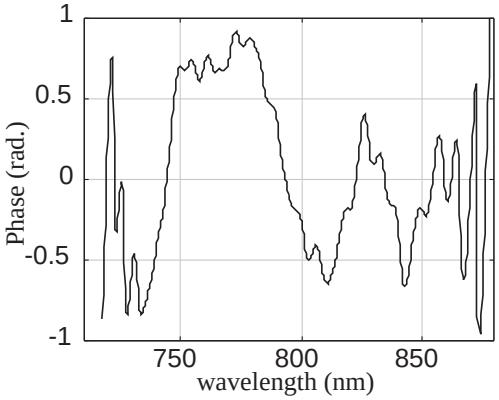

Fig. 4. Experimental dephasing introduced by the stretcher

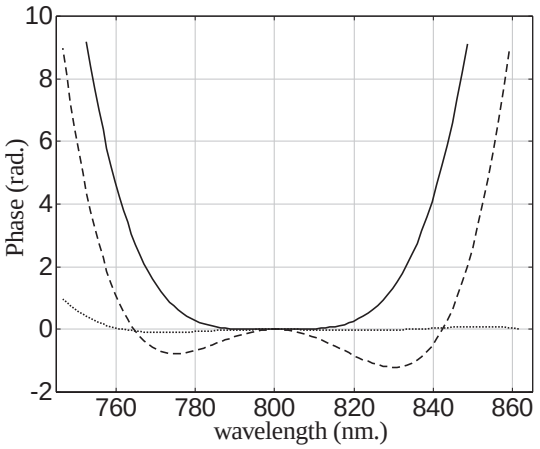

Fig. 5. Theoretical dephasing in a CPA chain including 0.5-m KDP, 0.5-m sapphire, 0.4-m BK7, and a 1200-gr/mm grating in the stretcher. The *solid line* is the dephasing from a 1200-gr/mm grating compressor setting following $\phi^{(2)}$ and $\phi^{(3)}$ cancellation. The *dashed line* gives a numerical optimization of the above system following global optimization. The *dotted line* is the dephasing obtained after global optimization of a 1500-gr/mm grating compressor

appropriate optics that can be manufactured easily, mainly flat and spherical mirrors.

To conclude, control of the amplification of sub-20-fs pulses must take both spectrum amplitude and phase into account. It is interesting to note that the amplified pulse spectrum will benefit from an ultrashort oscillator (sub-10-fs) and large-bandwidth coatings. We are now able to design very large-bandwidth CPA systems with a residual phase almost flat, and we can decrease the effect of gain narrowing in the amplifiers to such a limit that the coating bandwidth and the stretcher mirror quality are now the most limiting factors.

3 High average power amplification

In the recent years, above-0.1-TW peak-power lasers were achieved at a 1-kHz repetition rate [6, 7]. In their papers, the authors state the difficulty of coping with thermal effects occurring in the Ti:sapphire crystals of the amplifiers. At such a high repetition rate, the thermal lens is not negligible and its effects are deleterious. Assuming a radial symmetry and uniform pumping, the thermal lens focal distance is given by (1), where k, ν, $\partial n/\partial T$, and J_{sat} are respectively the thermal conductivity, the quantum ratio of the thermally dissipated energy to the total absorbed energy, the thermal index gradient and the saturation fluence of the material. In Ti:sapphire, at room temperature and at a 1-kHz repetition rate, for a small signal gain of about 3, the thermal lens focal distance is about 1 m, whatever the pumped area size and pumping energy are.

$$f_{\text{therm}} = 2k\nu \frac{1}{R\frac{\partial n}{\partial T} J_{\text{sat}} \log(G_0)} \,. \tag{1}$$

Nitrogen cooling improves the crystal thermal properties and in the 100 K regime, the thermal lens focal length is 20 times longer than at room temperature. Therefore its effect is nearly negligible. However the use of cryogenic techniques is not rewarding as it contributes to making the laser operation

more difficult. On the contrary, the technique of thermal lens imaging [14] allows one to operate the laser system at room temperature.

The thermal lens imaging technique introduces a coupling between geometric parameters, and the realization of the amplifier should be done as follows: first, one must determine the radius of the pumped area according to the expected gain. In our case, the pumping energies are 20 mJ, 30 mJ, and 40 mJ for successive amplifiers. This gives radii of 0.5 mm, 0.6 mm, and 0.7 mm, respectively for a gain of about 3 per pass. Efficient energy extraction and minimum beam distortion will be achieved if the laser beam waist is about this radius size. So, given the radius of the laser beam on the crystal and the thermal focal length (determined by the gain), one calculates the amplifier arm length that is necessary for stable imaging from one pass to the other. A simulation of the amplifier length is presented in Fig. 6, as a function of the diameter of the pumped area on the crystal. A first information is that the length of the amplifier does not depend too much on the pumping power. As a consequence, thermal lens imaging is poorly affected by variation of the pumping power. Another information is the amplifier length itself. For lower pumping powers, the solution is very compact, whereas at higher pumping powers the amplifier length increases too much. So, this method can not be extended to very high average powers without some modification from the original setup.

Yet, at moderate pumping powers, once set, the system is very stable and does not show much sensitivity to pumping power variations. Another important issue is the coupling between these amplifiers. They demand mode matching and much care should be taken to image the beam waist with the proper diameter from one amplifier to the other. Moreover, the thermal lens together with the localized gain region act like a spatial filter that cleans the laser beam from one pass to the other. As a result the far-field image of the beam profile is very good, as seen on Fig. 7. This filtering can even correct the small astigmatism which currently occurs in the regenerative pre-amplifier.

Nevertheless, this methods meets its limits when one tries to use it above 30 mJ pump energies as the amplifier arm length increases above 2 m and the laser fluence on the folding mirror reaches the material damage threshold. For this reason we adopt a different scheme in the final amplifier: as shown on Fig. 8, the beam is focused prior to entering the amplifier, and the thermal lens collimates the laser beam between its two passes. Of course, no optical element can be located about the beam focus, before and after the multipass amplifier. Using this technique amplification of ultrashort pulses can be extended to higher average powers at 1 kHz. The length of the amplifier does not increase when the pumping power increases: the only parameter to vary will be the radius of the pumped area in order to keep both the gain and the thermal lens constant. Therefore the beam waist radius before the entrance of the amplifier is modified.

In summary we have found that the thermal lens imaging technique is very stable and that the pumping power has little effect on the beam spatial profile. Moreover it tends to force the laser mode into the amplifier mode by self ampli-

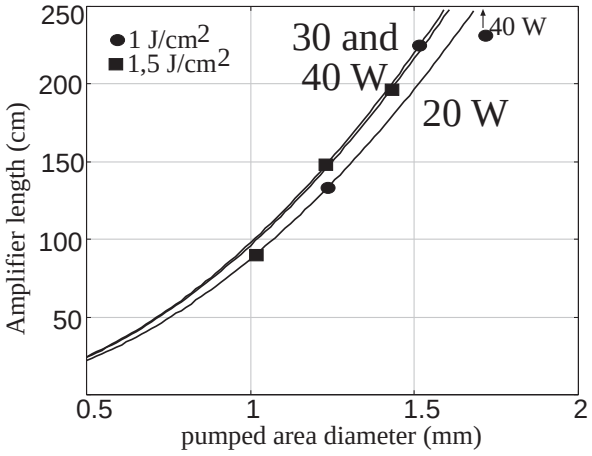

Fig. 6. Simulation of a multipass amplifier length as a function of the pumped area diameter. For two pumping fluences, the operation points are spotted

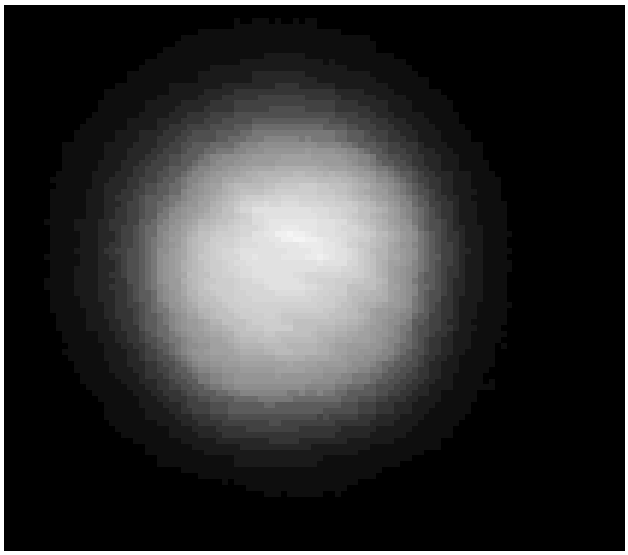

Fig. 7. Far-field measurement of the beam spot

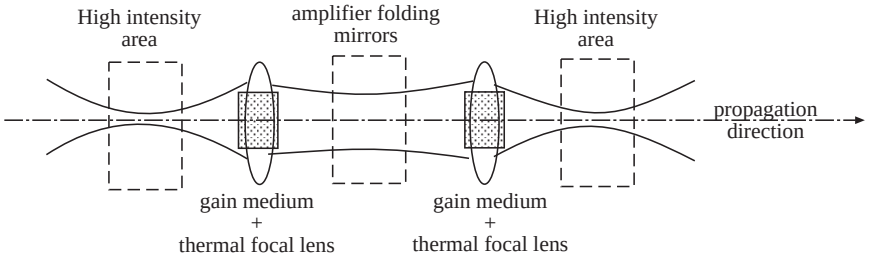

Fig. 8. Unfolded schematic of a high-energy, high-average-power, two-pass amplifier

tude and phase cleaning from one pass to the other. However, for higher pumping powers pure eigenmode imaging is not possible and we have presented an alternative to keep the amplifier a reasonable size.

4 Conclusion

We have adopted recent developments in laser physics such as global optimization, regenerative pulse shaping with a birefringent filter, and thermal lens imaging to sucessfully realize a laser chain that delivers terawatt pulses at a 1-kHz repetition rate. We would like to emphasise on the 20% extraction efficiency of this laser, which, together with 100 W pumping power, demonstrates the higest average power ultrafast laser chain developed to date. Applications that have been done using this source are high-order harmonic generation in hollow-core fibers and soft to hard X-ray generation from clusters. In the future, development of laser chains with pulse duration in the 10-fs regime would make this kind of system more compact and a powerful tool as a primary source for attosecond physics.

References

1. P. Maine, D. Strickland, P. Bado, M. Pessot, G. Mourou: IEEE J. Quantum Electron. **QE-24**, 398 (1988)
2. M.D. Perry, D. Pennington, B.C. Stuart, G. Tietbothl, J.A. Britten, C. Brown, S. Herman, B. Golick, M. Kartz, J. Miller, H.T. Powell, M. Vergino, V. Yanovsky: Opt. Lett. **24**, 160 (1999)
3. A. Antonetti, F. Blasco, J.P. Chambaret, G. Chériaux, G. Darpentigny, C. Le Blanc, P. Rousseau, S. Ranc, G. Rey, F. Salin: Appl. Phys. B **65**, 197 (1997)
4. C.P.J. Barty, T. Guo, C. Le Blanc, F. Raksi, C. Rose-Petruck, J. Squier, K.R. Wilson, V.V. Yakolev, K. Yamakawa: Opt. Lett. **21**, 668 (1996)
5. K. Yamakawa, M. Aoyoma, S. Matsuoka, H. Takuma, D.N. Fittinghoff, C.P.J. Barty: IEEE J. Sel. Top. Quantum Electron. **4**, 385 (1998)
6. S. Backus, C.G. Durfee III, G. Mourou, H. Kapteyn, M. Murnane: Opt. Lett. **22**, 1256 (1997)
7. Y. Nabekawa, Y. Kuramoto, T. Togashi, T. Sekikawa, S. Watanabe: Opt. Lett. **23**, 1384 (1998)
8. A. L'Huillier, P. Balcou: Phys. Rev. Lett. **70**, 774 (1993)
9. I.P. Christov, J. Zhou, J. Peatross, A. Rundquist, M.M. Murnane, H.C. Kapteyn: Phys. Rev. Lett. **77**, 1743 (1996)
10. C. Spielmann, N.H. Burnett, S. Sartania, R. Koppitsch, M. Schnürer, C. Kan, M. Lenzner, P. Wobrauschek, F. Krausz: Science **278**, 661 (1997)
11. G. Chériaux, P. Rousseau, F. Salin, J.P. Chambaret, B. Walker, L.F. Dimauro: Opt. Lett. **21**, 414 (1996)
12. A.E. Siegmann: *Lasers* (University Science Books. Mill Valley 1986) p. 281
13. C.P.J. Barty, T. Guo, C. Le Blanc, G. Korn, C. Rose-Petruck, F. Raksi, J. Squier, K.R. Wilson, V.V. Yakolev, K. Yamakawa: In CLEO-CTuR2 (1996)
14. F. Salin, C. Le Blanc, J. Squier, C.P.J. Barty: Opt. Lett. **23**, 718 (1998)
15. E.B. Treacy: IEEE J. Quantum Electron. **QE-5**, 454 (1969)
16. V. Bagnoud, F. Salin: IEEE J. Sel. Top. Quantum Electron. **4**, 445 (1998)
17. R.A. Myers, N. Mukherjee, S.R.J. Brueck: Opt. Lett. **16**, 1732 (1991)
18. J. Faure, J. Itatani, S. Biswal, G. Chériaux, L.R. Bruner, G.C. Templeton, G. Mourou: Opt. Commun. **159**, 68 (1999)
19. C.G. Durfee III, S. Backus, M. Murnane, H. Kapteyn: IEEE J. Sel. Top. Quantum Electron. **4**, 395 (1998)
20. J. Squier, C.P.J. Barty, F. Salin, C. Le Blanc, S. Kane: Appl. Opt. **37**, 1638 (1998)
21. C. Iaconis, I. Wamsley: Opt. Lett. **23**, 792 (1998)
22. V. Bagnoud, F. Salin: J. Opt. Soc. Am. B 16, No 1 (1999)

July 15, 2005 / Vol. 30, No. 14 / OPTICS LETTERS 1843

5 Hz, >250 mJ optical parametric chirped-pulse amplifier at 1053 nm

Vincent Bagnoud, Ildar A. Begishev, Mark J. Guardalben, Jason Puth, and Jonathan D. Zuegel

Laboratory for Laser Energetics, University of Rochester, 250 East River Road, Rochester, New York 14623

Received December 8, 2004

A 250 mJ, 5 Hz repetition rate optical parametric chirped-pulse amplifier with near-Fourier-transform-limited, 430 fs pulses and a beam that can be focused to near the diffraction limit is demonstrated. A pump laser with engineered spatial and temporal profiles allows an overall pump-to-signal conversion efficiency of 34% to be achieved. © 2005 Optical Society of America

OCIS codes: 140.7090, 190.4970, 140.3280.

Optical parametric chirped-pulse amplification[1,2] (OPCPA) can amplify ultrafast laser pulses because of its broadband gain without many of the disadvantages of regenerative amplification.[3] OPCPA offers high-contrast seeding of petawatt laser systems,[4] scalability to high energies,[5] and amplification of ultrabroadband pulses.[6] OPCPA systems typically utilize bulk nonlinear materials, such as lithium triborate (LBO), β-barium borate (BBO), and potassium dihydrogen phosphate (KDP), but quasi-phase-matched OPCPA has also been demonstrated for low-energy application.[7]

Maximizing the pulse energy from a broadband OPCPA front end to be injected into a high-energy Nd:glass laser system reduces the total gain narrowing in the system and yields the shortest available transform-limited compressed pulses. Moderate repetition rates with high energies are desirable for a variety of applications including system alignment, particularly the large-area grating compressor at the end of the amplifier chain. A high-average-power OPCPA system drives the pump laser's power requirements and naturally benefits from a high OPCPA pump-to-signal conversion efficiency. For example, the highest conversion efficiency demonstrated with commercial pump lasers is about 6%,[3] which requires a pump power almost 20 times that of the desired OPCPA output power.

Recently, we predicted and experimentally demonstrated[8] that the pump-to-signal OPCPA conversion efficiency can be greatly improved by carefully tailoring the pump laser's spatial and temporal profiles. In that work, pump-laser depletion greater than 60% was achieved in a single-stage OPCPA by use of a top hat, in space and time, pump laser. This same approach was applied in the proposed design of a high-energy, two-stage OPCPA system[9] to realize improved OPCPA output energy stability and beam quality. In this Letter an OPCPA system that uses this design demonstrates more than 1 W of average power at 5 Hz with pulses compressible to 1.07 times the Fourier transform limit and a beam that focuses to near the diffraction limit. To achieve this goal, we developed a pump laser well matched to efficient pumping of OPCPA systems.[10] With wave-front-corrected, 25.4 mm diameter Nd:YLF rods, the pump laser's power amplifier delivers nearly 9 W at a 527 nm wavelength and a 5 Hz repetition rate with a high beam spatial quality.

The experimental setup is shown in Fig. 1. Ultrashort seed pulses generated in a mode-locked Nd:glass oscillator (Time-Bandwidth Products GLX200) are synchronized to a master clock that also sets the timing of the pump laser. The 6 nm bandwidth (FWHM) seed pulses are stretched in an Öffner triplet pulse stretcher to 2.4 ns (FWHM)[11] to minimize B-integral accumulation during amplification in subsequent stages of a multikilojoule, Nd:glass laser system. Stretching optical pulses by a factor of up to $\sim 10^4$ while preserving the spectral phase requires high-quality stretcher optics,[12] so the surface quality of the primary and secondary mirrors used was $\lambda/35$ (peak to valley).

A pump laser[10] delivers 2.5 ns pulses at 5 Hz and a 527 nm wavelength. The 20th-order, super-Gaussian temporal and spatial profiles are critical to the efficient operation of the two-stage optical parametric amplification system,[8,9] while the 15 ps (rms) temporal jitter between the pump and the seed lasers yields exceptional wavelength stability of the amplified OPCPA signal.

High OPCPA pump-to-signal conversion efficiency and output energy stability are simultaneously achieved with a single pump laser in the two-stage

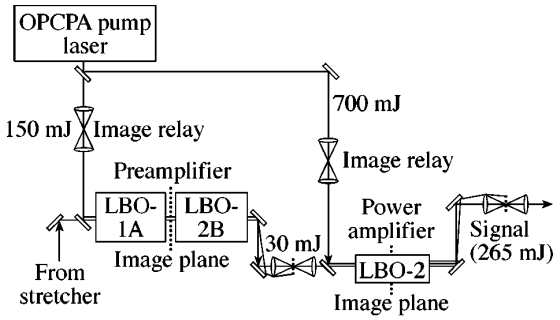

Fig. 1. Experimental setup. The preamplifier optical parametric amplifier stage uses two critically phased-matched LBO crystals in a walk-off-compensated arrangement. The power-amplifier optical parametric amplifier stage produces energies up to 265 mJ.

0146-9592/05/141843-3/$15.00

1844 OPTICS LETTERS / Vol. 30, No. 14 / July 15, 2005

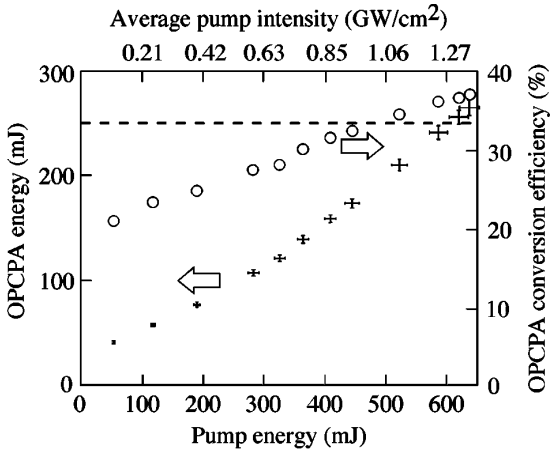

Fig. 2. OPCPA output energy as a function of the pump energy delivered to the power amplifier.

OPCPA by using LBO crystals, as well as by optimizing the pump laser's stability. A two-crystal preamplifier stage provides high gain, while a single-crystal power amplifier yields high energy-extraction efficiency. Operating the preamplifier stage with some OPCPA reconversion and the power amplifier in saturation balances the effect of pump-energy variations, while maximizing energy extraction.[9]

LBO provides broad angular acceptance and low pump-to-signal walk-off compared to other bulk nonlinear crystals, such as BBO and KDP, commonly used in degenerate OPCPA systems at 1053 nm. The broad angular acceptance of LBO reduces the OPCPA system sensitivity to pump-laser wave-front errors, which can lead to reduced efficiency and undesirable beam modulation. Minimizing pump-to-signal walk-off also improves overall efficiency and beam quality, especially in a preamplifier that utilizes long crystals and small beams.

The preamplifier stage uses two 5 mm $\times$ 5 mm $\times$ 29.75 mm critically phased-matched LBO crystals in a walk-off-compensated arrangement operating at a nominal pump intensity of 1 GW/cm^2. The 2.5 mm (FWHM) circular pump beam is matched to the Gaussian width of the seed beam from the stretcher. A slight noncollinear angle (8 mrad external) between the pump and the seed beams in the phase-matching direction prevents parasitic self-doubling of the intense amplified signal and reduces pump–signal walk-off effects.[13] This angular separation also simplifies separating the amplified signal beam from the residual pump and idler beams. Seed pulses are amplified from 600 pJ to 30 mJ, corresponding to a net gain of 5×10^7 with a conversion efficiency exceeding 24%. Driving the OPCPA preamplifier slightly into the reconversion regime optimizes the two-stage system's efficiency, as well as the energy stability.[9]

The preamplifier output signal beam is image relayed with a magnification of 2.15$\times$ to the OPCPA power-amplification stage. The total measured transmission between the preamplifier and the power amplifier is greater than 90%. As in Fig. 2, pump-pulse energies up to 640 mJ are delivered to a 10 mm $\times$ 10 mm $\times$ 11 mm LBO power-amplifier crystal, resulting in 265 mJ signal pulses. At maximum pump power, over 1.2 GW/cm^2 pump intensities allow 37% pump-to-signal net conversion efficiency to be reached with no saturation effect observed. The system's average power equals 1.3 W, which is, to our knowledge, the highest average power ever reported for an OPCPA system, limited only by the available pump power. The total system efficiency, including preamplifier and power amplifier, is 34% with an energy stability of 1% (rms) over 100 shots.

The amplified signal beam's near-field profile shown in Fig. 3(a) was measured with an 8 bit CCD camera (Cohu 1200 series). Heavy saturation in the OPCPA system reshapes the initially Gaussian spatial profile of the seed beam to match the super-Gaussian pump-laser profile. The preamplifier output spatial profile is modulated, due to a sensitivity of the beam to the pump spatial phase, via a narrow angular acceptance in this stage. In the power amplifier, this sensitivity is reduced because a shorter crystal yields a broader angular acceptance; therefore, the range of intensities across the beam is narrowed to a peak-to-mean value lower than 50%.

The amplified signal beam's far-field distribution, shown in Fig. 3(b), was recorded at the focus of a 1 m focal length lens by an 8 bit CCD camera with a 100-shot average to further increase the detection resolu-

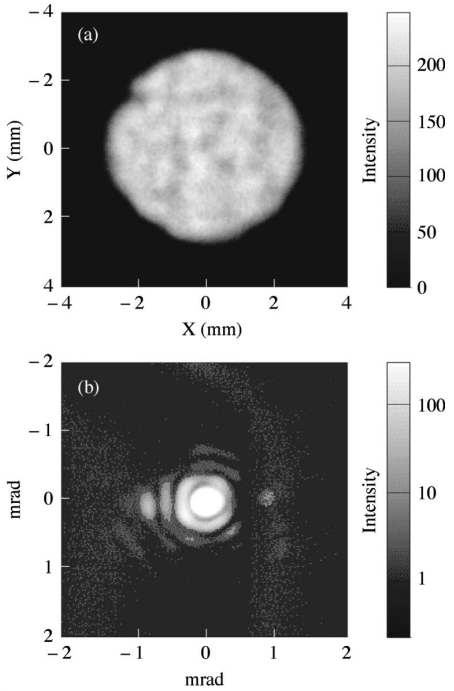

Fig. 3. (a) Near-field image of the OPCPA output beam showing a near-flattop energy density distribution. (b) Far-field image of the OPCPA output energy distribution at the focus of a 1 m focal distance lens showing the excellent focusing properties of the OPCPA system.

July 15, 2005 / Vol. 30, No. 14 / OPTICS LETTERS 1845

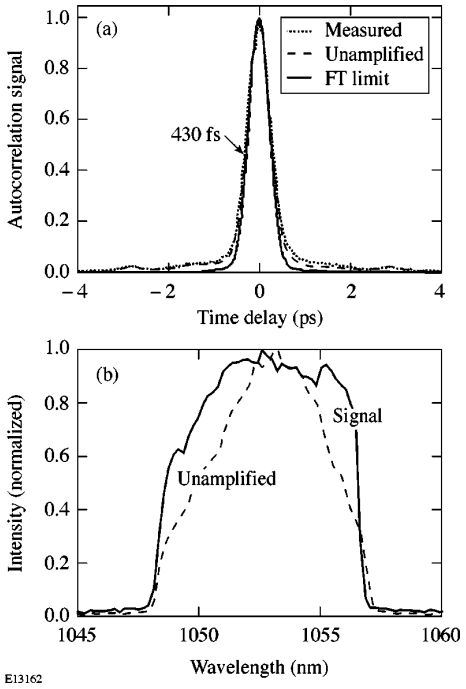

Fig. 4. (a) Second-order autocorrelation trace of the compressed OPCPA system output compared to the transform-limited performance. FT, Fourier transform. (b) Uncompressed OPCPA output spectrum illustrates the heavy saturation produced in the two-stage scheme.

tion to ~11 bits. The measured far-field profile shows a FWHM that equals 1.10 ± 0.02 and 1.05 ± 0.02 times the theoretical limit-based propagation of the near-field profile in Fig. 2(a). This qualitatively indicates that the signal beam focuses close to the diffraction limit.

Figure 4(a) shows an autocorrelation trace of the output pulses after compression in a folded, double-pass compressor. The autocorrelation trace is shown along with a simulated autocorrelation function calculated for a transform-limited pulse based on the OPCPA system's output spectrum. Both autocorrelation traces overlap well with only a 7% mismatch between the FWHM widths. A pedestal observed in autocorrelation traces measured for both amplified and unamplified pulses that match over more than 3 orders of magnitude is attributed to spectral phase errors in both the stretcher and compressor that often arise in chirped-pulse amplification systems with large stretching and compression ratios.

In conclusion, we have demonstrated an OPCPA system suitable for the injection of a multikilojoule, short-pulse laser with good performance. The OPCPA output simultaneously shows high conversion efficiency and energy stability, as well as excellent pulse compressibility and focusability. Our current plan includes improving the signal-beam modulation by an increased control over the pump-phase-to-signal-amplitude coupling in the preamplifier.

This work was supported by the U.S. Department of Energy (DOE) Office of Inertial Confinement Fusion under Cooperative Agreement DE-FC52-92SF19460, the University of Rochester, and the New York State Energy Research and Development Authority. The support of DOE does not constitute an endorsement by DOE of the views expressed in this article. V. Bagnoud's e-mail address is vbag@lle.rochester.edu.

References

1. A. Dubietis, G. Jonusauskas, and A. Piskarskas, Opt. Commun. **88**, 437 (1992).
2. I. N. Ross, P. Matousek, M. Towrie, A. J. Langley, and J. L. Collier, Opt. Commun. **144**, 125 (1997).
3. I. Jovanovic, B. J. Comaskey, C. A. Ebbers, R. A. Bonner, D. M. Pennington, and E. C. Morse, Appl. Opt. **41**, 2923 (2002).
4. Y. Kitagawa, H. Fujita, R. Kodama, H. Yoshida, S. Matsuo, T. Jitsuno, T. Kawasaki, H. Kitamura, T. Kanabe, S. Sakabe, K. Shigemori, N. Miyanaga, and Y. Izawa, IEEE J. Quantum Electron. **40**, 281 (2004).
5. J. L. Collier, I. N. Ross, L. Cardoso, O. Chekhlov, M. Notley, C. Hernandez-Gomez, P. Matousek, C. N. Danson, D. Neely, and S. Hancock, in *Inertial Fusion Sciences and Applications 2003*, B. A. Hammel, D. D. Meyerhofer, J. Meyer-ter-Vehn, and H. Azechi, eds. (American Nuclear Society, 2004), p. 603.
6. C. P. Hauri, P. Schlup, G. Arisholm, J. Biegert, and U. Keller, Opt. Lett. **29**, 1369 (2004).
7. I. Jovanovic, J. R. Schmidt, and C. A. Ebbers, Appl. Phys. Lett. **83**, 4125 (2003).
8. L. J. Waxer, V. Bagnoud, I. A. Begishev, M. J. Guardalben, J. Puth, and J. D. Zuegel, Opt. Lett. **28**, 1245 (2003).
9. M. J. Guardalben, J. Keegan, L. J. Waxer, V. Bagnoud, I. A. Begishev, J. Puth, and J. D. Zuegel, Opt. Express **11**, 2511 (2003).
10. V. Bagnoud, M. J. Guardalben, J. Puth, J. D. Zuegel, T. Mooney, and P. Dumas, Appl. Opt. **44**, 282 (2005).
11. G. Cheriaux, P. Rousseau, F. Salin, J. P. Chambaret, B. Walker, and L. F. Dimauro, Opt. Lett. **21**, 414 (1996).
12. V. Bagnoud and F. Salin, J. Opt. Soc. Am. B **16**, 188 (1999).
13. I. A. Begishev, V. Bagnoud, M. J. Guardalben, J. Puth, L. J. Waxer, and J. D. Zuegel, in *Advanced Solid-State Photonics*, Vol. 94 of OSA Trends in Optics and Photonics Series (Optical Society of America, 2004), p. 32.

Chapter 4

Conclusion and Outlook

This manuscript gives a concise and fair overview on my contribution to the field of high-energy high-intensity lasers which I undertook alongside the delivery of three important laser systems still in operation nowadays, that are the Aurore, front end prototype for OMEGA-EP and PHELIX laser facilities in France, the USA and Germany respectively. In comparison to other fields of technical development where proof of principle experiments followed by publications are a self-consistent process, the operation of these facilities and their further development also requires bringing the new ideas to a much higher level of technical readiness level, where new developments face real-world operation and robustness must be traded off ultimate performance.

In addition to the collection of articles found in chapters 2 and 3, the manuscript includes some complementary unpublished work related to the analysis of the temporal contrast problematic and in particular the proposal to develop a stretcher with a large beam-to-stretch ratio that could significantly improve the temporal contrast of the pulse and which I will try to demonstrate experimentally in the upcoming years. For beam control, the quantitative comparison of the LG mode sensibility to aberration in view of the Marechal criteria for standard aberration is a calculation which is probably worth publishing, because many theoretical article show the advantages of creating such beams but are not aware of the technical difficulty to implement such a beam profile at a high-intensity laser facility.

For the last part devoted to laser cooling, I omitted to cover an alternative technique relying on longitudinal laser cooling. There has been a growing community working on such ideas for the past twenty years, starting from pioneering work done on the cooling of amplifiers for the Mercury project, to a more widespread effort done with some impressive results obtained on active mirrors for high average power. But unfortunately, the active mirror technique is not scalable to high energies above the joule level because of transverse lasing limitations. As an alternative, the active cooling of laser slabs either by liquids or gases is being proposed and explored in various places with positive results but also underlining the great technical challenges of such a scheme. Recently, the university of Darmstadt has also started its own program, motivated by the need to support the development of high-energy high-average-power lasers for applications at the FAIR facilities. Such a development is probably very challenging but it has a huge potential as one of the key technological aspect for the next generation of high-intensity lasers. Regardless of the pulse amplification scheme used, from the more standard direct amplification in kilojoule glass amplifiers and the pumping of large titanium-doped sapphire crystals, to more innovative schemes based on non-linear amplification in parametric or Raman amplifiers, the need of cooling of high-energy

kilojoule amplifiers is a necessary development that key players in the field must master.

In the coming years, high-energy high-intensity lasers will be applied to a wider field of research as they will be more and more coupled to other drivers and diagnostics tools. The example of such a strategy can be found today with the Hibef program at the XFEL coupling high-energy lasers to the high-performance x-ray diagnostic of the FEL, or the ELI-NP coupling the high-intensity 10-PW beamlines to a gamma source. Closer to Darmstadt, the plasma physics community also aims at developing a world-wide unique experimental combination of petawatt lasers and high-intensity ion beams, for which a strong expertise in mid-to-large scale facility will be necessary.

Bibliography

[1] J. H. Kelly *et al.*, "OMEGA EP: High-energy petawatt capability for the omega laser facility," Journal de Physique IV (Proceedings) **133**, 75–80 (2006).

[2] V. Bagnoud *et al.*, "Commissioning and early experiments of the phelix facility," Applied Physics B **100**, 137–150 (2010).

[3] D. Strickland and G. Mourou, "Compression of amplified chirped optical pulses," Opt. Commun. **55**, 447–449 (1985).

[4] P. F. Moulton, "Spectroscopic and laser characteristics of Ti:Al_2O_3," J. Opt. Soc. Am. B **3**, 125–133 (1986).

[5] F. G. Patterson, R. Gonzales, and M. D. Perry, "Compact 10-TW, 800-fs Nd:glass laser," Opt. Lett. **16**, 1107–1109 (1991).

[6] K. Yamakawa *et al.*, "100-TW sub-20-fs Ti:sapphire laser system operating at a 10-Hz repetition rate," Opt. Lett. **23**, 1468–1470 (1998).

[7] M. D. Perry *et al.*, "Petawatt laser pulses," Opt. Lett. **24**, 160–162 (1999).

[8] M. Aoyama *et al.*, "0.85-PW, 33-fs Ti:sapphire laser," Opt. Lett. **28**, 1594–1596 (2003).

[9] C. Danson *et al.*, "Petawatt class lasers worldwide," High Power Laser Science and Engineering **3**, e3 (2015).

[10] T. Tajima and J. Dawson, "Laser electron accelerator," Phys. Rev. Lett. **43**, 267 (1979).

[11] J. Faure *et al.*, "A laser–plasma accelerator producing monoenergetic electron beams," Nature **431**, 541–544 (2004).

[12] S. Mangles *et al.*, "Monoenergetic beams of relativistic electrons from intense laser–plasma interactions," Nature **431**, 535–538 (2004).

[13] C. Geddes *et al.*, "High-quality electron beams from a laser wakefield accelerator using plasma-channel guiding," Nature **431**, 538–541 (2004).

[14] A. Pukhov and J. Meyer-ter Vehn, "Laser wake field acceleration: the highly non-linear broken-wave regime," Appl. Phys. B - Lasers O. **74**, 355–361 (2002).

[15] A. Modena *et al.*, "Electron acceleration in plasmas by laser pulse," Nature **337**, 806–807 (1995).

[16] W. P. Leemans *et al.*, "GeV electron beams from a centimetre-scale accelerator," Nat. Phys. **2**, 696–699 (2006).

[17] W. P. Leemans *et al.*, "Multi-GeV electron beams from capillary-discharge-guided subpetawatt laser pulses in the self-trapping regime," Phys. Rev. Lett. **113**, 245002 (2014).

[18] W. P. Leemans *et al.*, "Bella laser and operations," in "Proc. PAC," (2013).

[19] S. Karsch *et al.*, "GeV-scale electron acceleration in a gas-filled capillary discharge waveguide," New J. Phys. **9**, 415 (2007).

[20] H. T. Kim *et al.*, "Enhancement of electron energy to the multi-GeV regime by a dual-stage laser-wakefield accelerator pumped by petawatt laser pulses," Phys. Rev. Lett. **111**, 165002 (2013).

[21] X. Wang *et al.*, "Quasi-monoenergetic laser-plasma acceleration of electrons to 2 GeV," Nat. Commun. **4** (2013).

[22] M. Geissler, J. Schreiber, and J. Meyer-ter Vehn, "Bubble acceleration of electrons with few-cycle laser pulses," New J. Phys. **8**, 186 (2006).

[23] M. Lobet *et al.*, "Toward quantum electrodynamics experiments on forthcoming high-power laser facilities," in "42$^{\text{nd}}$ EPS Conference on Plasma Physics," (2015).

[24] W. I. Linlor, "Ion energies produced by laser giant pulse," Appl. Phys. Letters **3** (1963).

[25] R. A. Snavely *et al.*, "Intense high-energy proton beams from petawatt-laser irradiation of solids," Phys. Rev. Lett. **85**, 2945 (2000).

[26] S. Bulanov *et al.*, "Oncological hadrontherapy with laser ion accelerators," Physics Letters A **299**, 240–247 (2002).

[27] M. Roth *et al.*, "Fast ignition by intense laser-accelerated proton beams," Phys. Rev. Lett. **86**, 436 (2001).

[28] P. Patel *et al.*, "Isochoric heating of solid-density matter with an ultrafast proton beam," Phys. Rev. Lett. **91**, 125004 (2003).

[29] M. Roth *et al.*, "Bright laser-driven neutron source based on the relativistic transparency of solids," Phys. Rev. Lett. **110**, 044802 (2013).

[30] C. M. Brenner *et al.*, "High energy conversion efficiency in laser-proton acceleration by controlling laser-energy deposition onto thin foil targets," Appl. Phys. Lett. **104**, 081123 (2014).

[31] S. Wilks *et al.*, "Energetic proton generation in ultra-intense laser–solid interactions," Physics of Plasmas (1994-present) **8**, 542–549 (2001).

[32] T. E. Cowan *et al.*, "Ultralow emittance, multi-MeV proton beams from a laser virtual-cathode plasma accelerator," Phys. Rev. Lett. **92**, 204801 (2004).

[33] M. Roth *et al.*, "The generation of high-quality, intense ion beams by ultra-intense lasers," Plas. Phys. Contr. Fus. **44**, B99 (2002).

[34] H. Daido, M. Nishiuchi, and A. S. Pirozhkov, "Review of laser-driven ion sources and their applications," Reports on Progress in Physics **75**, 056401 (2012).

[35] F. Wagner *et al.*, "Towards 100 MeV maximum energy for laser-accelerated proton beams," Bulletin of the American Physical Society **60** (2015).

[36] V. Khoroshkov and E. Minakova, "Proton beams in radiotherapy," European journal of physics **19**, 523 (1998).

[37] A. P. L. Robinson *et al.*, "Radiation pressure acceleration of thin foils with circularly polarized laser pulses," New J. Phys. **10**, 013021 (2008).

[38] I. J. Kim *et al.*, "Transition of proton energy scaling using an ultrathin target irradiated by linearly polarized femtosecond laser pulses," Phys. Rev. Lett. **111**, 165003 (2013).

[39] L. Yin *et al.*, "GeV laser ion acceleration from ultrathin targets: The laser break-out afterburner," Laser Part. Beams **24**, 291–298 (2006).

[40] D. Jung *et al.*, "Laser-driven 1 GeV carbon ions from preheated diamond targets in the break-out afterburner regime," Physics of Plasmas (1994-present) **20**, 083103 (2013).

[41] M. M. Murnane *et al.*, "Ultrafast X-ray pulses from laser-produced plasmas," Science **251**, 531–536 (1991).

[42] V. Malka *et al.*, "Principles and applications of compact laser–plasma accelerators," Nat. Phys. **4**, 447–453 (2008).

[43] A. Rousse *et al.*, "Production of a keV X-ray beam from synchrotron radiation in relativistic laser-plasma interaction," Phys. Rev. Lett. **93**, 135005 (2004).

[44] E. Gerstner, "Laser physics: Extreme light," Nature **446**, 16–18 (2007).

[45] D. D. Meyerhofer *et al.*, "OMEGA EP OPAL: A path to a 100-PW laser system," in "APS Meeting Abstracts," , vol. 1 (2014), vol. 1, p. 5006.

[46] A. V. Bashinov *et al.*, "New horizons for extreme light physics with mega-science project XCELS," The European Physical Journal Special Topics **223**, 1105–1112 (2014).

[47] H. Azechi *et al.*, "Present status of the FIREX programme for the demonstration of ignition and burn," Plasma Phys. Contr. F. **48**, B267 (2006).

[48] R. Baier and P. Breitenlohner, "The vacuum refraction index in the presence of external fields," Il Nuovo Cimento B (1965-1970) **47**, 117–120 (1967).

[49] G. Mourou *et al.*, "The future is fibre accelerators," Nat. Phot. **7**, 258–261 (2013).

[50] L. Hargrove, R. Fork, and M. Pollack, "Locking of He–Ne laser modes induced by synchronous intracavity modulation," Appl. Phys. Lett. **5**, 4–5 (1964).

[51] D. J. Jones *et al.*, "Carrier-envelope phase control of femtosecond mode-locked lasers and direct optical frequency synthesis," Science **288**, 635–639 (2000).

[52] A. Braun *et al.*, "Characterization of short-pulse oscillators by means of a high-dynamic-range autocorrelation measurement," Opt. Lett. **20**, 1889–1891 (1995).

[53] P. F. Curley *et al.*, "High dynamic range autocorrelation studies of a femtosecond Ti:sapphire oscillator and its relevance to the optimisation of chirped pulse amplification systems," Opt. Commun. **120**, 71–77 (1995).

[54] B. Reagan *et al.*, "Development of high energy diode-pumped thick-disk Yb:YAG chirped-pulse-amplification lasers," IEEE J. Quantum Elect. **48**, 827–835 (2012).

[55] A. Bayramian *et al.*, "The mercury project: A high average power, gas-cooled laser for inertial fusion energy development," Fusion Science and Technology **52**, 383–387 (2007).

[56] A. Dubietis, G. Jonušauskas, and A. Piskarskas, "Powerful femtosecond pulse generation by chirped and stretched pulse parametric amplification in BBO crystal," Opt. Commun. **88**, 437–440 (1992).

[57] J. Rothhardt *et al.*, "High average and peak power few-cycle laser pulses delivered by fiber pumped OPCPA system," Opt. Express **18**, 12719–12726 (2010).

[58] A. Klenke *et al.*, "530 W, 1.3 mJ, four-channel coherently combined femtosecond fiber chirped-pulse amplification system," Opt. Lett. **38**, 2283–2285 (2013).

[59] I. Jung *et al.*, "Self-starting 6.5-fs pulses from a Ti:sapphire laser," Opt. Lett. **22**, 1009–1011 (1997).

[60] U. Morgner *et al.*, "Sub-two-cycle pulses from a kerr-lens mode-locked Ti:sapphire laser," Opt. Lett. **24**, 411–413 (1999).

[61] C. Barty *et al.*, "Regenerative pulse shaping and amplification of ultrabroadband optical pulses," Opt. Lett. **21**, 219–221 (1996).

[62] A. M. Weiner, "Femtosecond pulse shaping using spatial light modulators," Review of scientific instruments **71**, 1929–1960 (2000).

[63] T. Oksenhendler *et al.*, "Intracavity acousto-optic programmable gain control for ultra-wideband regenerative amplifiers," Appl. Phys. B - Lasers O. **83**, 491–494 (2006).

[64] E. W. Gaul *et al.*, "Demonstration of a 1.1 petawatt laser based on a hybrid optical parametric chirped pulse amplification/mixed Nd:glass amplifier," Appl. Optics **49**, 1676–1681 (2010).

[65] V. Bagnoud *et al.*, "5 Hz, >250 mJ optical parametric chirped-pulse amplifier at 1053 nm," Opt. Lett. **30**, 1843–1845 (2005).

[66] H. Kiriyama *et al.*, "High temporal and spatial quality petawatt-class Ti:sapphire chirped-pulse amplification laser system," Opt. Lett. **35**, 1497–1499 (2010).

[67] V. Lozhkarev *et al.*, "Compact 0.56 petawatt laser system based on optical parametric chirped pulse amplification in KD^*P crystals," Laser Physics Letters **4**, 421 (2007).

[68] A. Jullien *et al.*, "Highly efficient temporal cleaner for femtosecond pulses based on cross-polarized wave generation in a dual crystal scheme," Appl. Phys. B - Lasers O. **84**, 409–414 (2006).

[69] T. J. Kessler *et al.*, "Demonstration of coherent addition of multiple gratings for high-energy chirped-pulse-amplified lasers," Opt. Lett. **29**, 635–637 (2004).

[70] J. Bromage *et al.*, "A focal-spot diagnostic for on-shot characterization of high-energy petawatt lasers," Opt. Express **16**, 16561–16572 (2008).

[71] T. J. Yu *et al.*, "Generation of high-contrast, 30 fs, 1.5 PW laser pulses from chirped-pulse amplification Ti:sapphire laser," Opt. Express **20**, 10807–10815 (2012).

[72] J. W. Hardy, "Adaptive optics: a progress review," in "San Diego,'91, San Diego, CA," (International Society for Optics and Photonics, 1991), pp. 2–17.

[73] J.-C. Chanteloup *et al.*, "Single-shot wave-front measurements of high-intensity ultrashort laser pulses with a three-wave interferometer," Opt. Lett. **23**, 621–623 (1998).

[74] R. Assmann *et al.*, "Proton-driven plasma wakefield acceleration: a path to the future of high-energy particle physics," Plas. Phys. Contr. Fus. **56**, 084013 (2014).

[75] I. Blumenfeld *et al.*, "Energy doubling of 42 GeV electrons in a metre-scale plasma wakefield accelerator," Nature **445**, 741–744 (2007).

[76] J. Itatani *et al.*, "Suppression of the amplified spontaneous emission in chirped-pulse-amplification lasers by clean high-energy seed-pulse injection," Opt. Commun. **148**, 70–74 (1998).

[77] N. Didenko *et al.*, "Contrast degradation in a chirped–pulse amplifier due to generation of prepulses by postpulses," Opt. Express **16**, 3178–3190 (2008).

[78] V. Bagnoud *et al.*, "A technique for measuring B–integral in chirped-pulse amplifiers," in "Conference on Lasers and Electro-Optics," (Optical Society of America, 2009), p. CFG4.

[79] S. Kane and J. Squier, "Fourth-order-dispersion limitations of aberration-free chirped-pulse amplification systems," J. Opt. Soc. Am. B **14**, 1237–1244 (1997).

[80] C. Dorrer *et al.*, "Single-shot real-time characterization of chirped-pulse amplification systems by spectral phase interferometry for direct electric-field reconstruction," Opt. Lett. **24**, 1644–1646 (1999).

[81] D. J. Kane and R. Trebino, "Single-shot measurement of the intensity and phase of an arbitrary ultrashort pulse by using frequency-resolved optical gating," Opt. Lett. **18**, 823–825 (1993).

[82] T. Oksenhendler *et al.*, "Self-referenced spectral interferometry," Appl. Phys. B - Lasers O. **99**, 7–12 (2010).

[83] F. Verluise *et al.*, "Amplitude and phase control of ultrashort pulses by use of an acousto-optic programmable dispersive filter: pulse compression and shaping," Opt. Lett. **25**, 575–577 (2000).

[84] S. Eliezer, *The interaction of high-power lasers with plasmas* (CRC Press, 2002).

[85] B. C. Stuart *et al.*, "Laser-induced damage in dielectrics with nanosecond to subpicosecond pulses," Phys. Rev. Lett. **74**, 2248 (1995).

[86] L. M. Cabalin and J. J. Laserna, "Experimental determination of laser induced breakdown thresholds of metals under nanosecond Q-switched laser operation," Spectrochimica Acta Part B: Atomic Spectroscopy **53**, 723–730 (1998).

[87] C. Carr, H. B. Radousky, and S. G. Demos, "Wavelength dependence of laser-induced damage: determining the damage initiation mechanisms," Phys. Rev. Lett. **91**, 127402 (2003).

[88] P. B. Corkum *et al.*, "Thermal response of metals to ultrashort-pulse laser excitation," Phys. Rev. Lett. **61**, 2886 (1988).

[89] L. DeShazer, B. Newnam, and K. Leung, "Role of coating defects in laser-induced damage to dielectric thin films," Appl. Phys. Lett. **23**, 607–609 (1973).

[90] U. Samir, K. Wright, and N. Stone, "The expansion of a plasma into a vacuum: Basic phenomena and processes and applications to space plasma physics," Reviews of Geophysics **21**, 1631–1646 (1983).

[91] R. Bleach and D. Nagel, "Plasma x-ray emission produced by ruby lasers at 10^{12} W/cm^2," J. Appl. Phys. **49**, 3832–3841 (1978).

[92] F. Young *et al.*, "Laser-produced-plasma energy transport through plastic films," Appl. Phys. Lett. **30**, 45–47 (1977).

[93] http://physics.nist.gov/PhysRefData/ASD/ionEnergy.html. The ionization energies for gold can be found from the NIST database - Accessed: 01/12/2015.

[94] J. MacFarlane, I. Golovkin, and P. Woodruff, "HELIOS-CR–A 1-D radiation-magnetohydrodynamics code with inline atomic kinetics modeling," Journal of Quantitative Spectroscopy and Radiative Transfer **99**, 381–397 (2006).

[95] M. Basko, J. Maruhn, and A. Tauschwitz, "Development of a 2D radiation-hydrodynamics code RALEF for laser plasma simulations," GSI Report **1**, 410 (2010).

[96] J. M. Dawson, "Particle simulation of plasmas," Reviews of modern physics **55**, 403 (1983).

[97] D. Tskhakaya, "The particle-in-cell method," in "Computational Many-Particle Physics," (Springer, 2008), pp. 161–189.

[98] R. A. Fonseca *et al.*, "Osiris: A three-dimensional, fully relativistic particle in cell code for modeling plasma based accelerators," in "Computational Science-ICCS 2002," (Springer, 2002), pp. 342–351.

[99] A. Pukhov, "Three-dimensional electromagnetic relativistic particle-in-cell code VLPL (Virtual Laser Plasma Lab)," Journal of Plasma Physics **61**, 425–433 (1999).

[100] T. D. Arber *et al.*, "Contemporary particle-in-cell approach to laser-plasma modelling," Plas. Phys. Contr. Fus. **57**, 1–26 (2015).

[101] J. Liljo *et al.*, "One-dimensional electromagnetic relativistic pic-hydrodynamic hybrid simulation code h-vlpl (hybrid virtual laser plasma lab)," Computer Physics Communications **179**, 371–379 (2008).

[102] V. V. Ivanov, A. Maksimchuk, and G. Mourou, "Amplified spontaneous emission in a Ti:sapphire regenerative amplifier," Appl. Optics **42**, 7231–7234 (2003).

[103] H. Haus and J. Mullen, "Quantum noise in linear amplifiers," Physical Review **128**, 2407 (1962).

[104] I. Jovanovic *et al.*, "Optical parametric chirped-pulse amplifier as an alternative to Ti:sapphire regenerative amplifiers," Appl. Optics **41**, 2923–2929 (2002).

[105] V. Bagnoud and F. Salin, "Global optimization of pulse compression in chirped pulse amplification," IEEE J. Sel. Top. Quant. **4**, 445–448 (1998).

[106] V. Bagnoud and F. Salin, "Influence of optical quality on chirped-pulse amplification: characterization of a 150-nm-bandwidth stretcher," J. Opt. Soc. Am. B **16**, 188–193 (1999).

[107] C. Dorrer *et al.*, "Optical parametric chirped-pulse-amplification contrast enhancement by regenerative pump spectral filtering," Opt. Lett. **32**, 2378–2380 (2007).

[108] A. Antonetti *et al.*, "A laser system producing 5×10^{19} W/cm^2 at 10 Hz," Appl. Phys. B - Lasers O. **65**, 197–204 (1997).

[109] K.-H. Hong *et al.*, "Generation and measurement of $> 10^8$ intensity contrast ratio in a relativistic kHz chirped-pulse amplified laser," Appl. Phys. B - Lasers O. **81**, 447–457 (2005).

[110] N. Forget *et al.*, "Pump-noise transfer in optical parametric chirped-pulse amplification," Opt. Lett. **30**, 2921–2923 (2005).

[111] C. Dorrer and J. Bromage, "Impact of high-frequency spectral phase modulation on the temporal profile of short optical pulses," Opt. Express **16**, 3058–3068 (2008).

[112] J. Ma *et al.*, "Spatiotemporal noise characterization for chirped-pulse amplification systems," Nat. Commun. **6** (2015).

[113] C. Hooker *et al.*, "Improving coherent contrast of petawatt laser pulses," Opt. Express **19**, 2193–2203 (2011).

[114] G. Cheriaux *et al.*, "Aberration-free stretcher design for ultrashort-pulse amplification," Opt. Lett. **21**, 414–416 (1996).

[115] A. Fernandez *et al.*, "Chirped-pulse oscillators: a route to high-power femtosecond pulses without external amplification," Opt. Lett. **29**, 1366–1368 (2004).

[116] M. Nantel *et al.*, "Temporal contrast in Ti:sapphire lasers, characterization and control," IEEE J. Sel. Top. Quant. **4**, 449–458 (1998).

[117] M. P. Kalashnikov *et al.*, "Double chirped-pulse-amplification laser: a way to clean pulses temporally," Opt. Lett. **30**, 923–925 (2005).

[118] A. Jullien *et al.*, "10^{-10} temporal contrast for femtosecond ultraintense lasers by cross-polarized wave generation," Opt. Lett. **30**, 920–922 (2005).

[119] C. Dorrer *et al.*, "High-contrast optical-parametric amplifier as a front end of high-power laser systems," Opt. Lett. **32**, 2143–2145 (2007).

[120] P. S. Banks *et al.*, "Novel all-reflective stretcher for chirped-pulse amplification of ultrashort pulses," IEEE J. Quantum Elect. **36**, 268–274 (2000).

[121] H. C. Kapteyn *et al.*, "Prepulse energy suppression for high-energy ultrashort pulses using self-induced plasma shuttering," Opt. Lett. **16**, 490–492 (1991).

[122] G. G. Scott *et al.*, "Optimization of plasma mirror reflectivity and optical quality using double laser pulses," New J. Phys. **17**, 033027 (2015).

[123] N. Hopps *et al.*, "Overview of laser systems for the orion facility at the AWE," Appl. Optics **52**, 3597–3607 (2013).

[124] J. A. Glaze, W. W. Simmons, and W. F. Hagen, "Status of large neodymium glass lasers," in "1976 SPIE/SPSE Technical Symposium East," (International Society for Optics and Photonics, 1976), pp. 7–14.

[125] "Section 1 laser systems report," LLE Review **2**, 1–4 (1979).

[126] J. M. Auerbach and V. P. Karpenko, "Serrated-aperture apodizers for high-energy laser systems," Appl. Optics **33**, 3179–3183 (1994).

[127] N. Blanchot *et al.*, "Experimental demonstration of a synthetic aperture compression scheme for multi-petawatt high-energy lasers," Opt. Express **18**, 10088–10097 (2010).

[128] C. Dorrer and J. D. Zuegel, "Design and analysis of binary beam shapers using error diffusion," J. Opt. Soc. Am. B **24**, 1268–1275 (2007).

[129] C. Dorrer, "High-damage-threshold beam shaping using binary phase plates," Opt. Lett. **34**, 2330–2332 (2009).

[130] V. Kermene *et al.*, "Flattening of the spatial laser beam profile with low losses and minimal beam divergence," Opt. Lett. **17**, 859–861 (1992).

[131] J. R. Leger, D. Chen, and Z. Wang, "Diffractive optical element for mode shaping of a Nd:YAG laser," Opt. Lett. **19**, 108–110 (1994).

[132] R. Mercier *et al.*, "Ion beam manufacturing of a graded-phase mirror for the generation of square top hat laser beams," in "Optical Systems Design," (International Society for Optics and Photonics, 2008), pp. 71020E–71020E.

[133] V. Bagnoud *et al.*, "Diode-pumped regenerative amplifier delivering 100-mJ single-mode laser pulses," Opt. Lett. **26**, 337–339 (2001).

[134] X. Ribeyre *et al.*, "Nd:glass diode-pumped regenerative amplifier, multimillijoule short-pulse chirped-pulse-amplifier laser," Opt. Lett. **28**, 1374–1376 (2003).

[135] J. Bourderionnet *et al.*, "Spatial mode control of a diode-pumped Nd:YAG laser by an intracavity liquid-crystal light valve," Opt. Lett. **26**, 1958–1960 (2001).

[136] J. P. Kirk and A. L. Jones, "Phase-only complex-valued spatial filter," J. Opt. Soc. Am. **61**, 1023–1028 (1971).

[137] D. Mendlovic *et al.*, "Encoding technique for design of zero-order (on-axis) fraunhofer computer-generated holograms," **36**, 8427–8434 (1997).

[138] S.-W. Bahk *et al.*, "A high-resolution, adaptive beam-shaping system for high-power lasers," Opt. Express **18**, 9151–9163 (2010).

[139] H. W. Babcock, "The possibility of compensating astronomical seeing," Publications of the Astronomical Society of the Pacific pp. 229–236 (1953).

[140] F. Rigaut *et al.*, "Adaptive optics on a 3.6-m telescope-results and performance," Astronomy and Astrophysics **250**, 280–290 (1991).

[141] A. W. Angelbeck *et al.*, "Active laser mirror system," (1978). US Patent 4,091,274.

[142] A. V. Kudryashov and V. I. Shmalhausen, "Semipassive bimorph flexible mirrors for atmospheric adaptive optics applications," Optical Engineering **35**, 3064–3073 (1996).

[143] R. A. Zacharias *et al.*, "National Ignition Facility (NIF) wavefront control system," in "Third International Conference on Solid State Lasers for Application to Inertial Confinement Fusion," (International Society for Optics and Photonics, 1999), pp. 678–692.

[144] J.-P. Zou *et al.*, "Optimization of the dynamic wavefront control of a pulsed kilojoule/nanosecond-petawatt laser facility," Appl. Optics **47**, 704–710 (2008).

[145] S. Fourmaux *et al.*, "Laser beam wavefront correction for ultra high intensities with the 200 TW laser system at the advanced laser light source," Opt. Express **16**, 11987–11994 (2008).

[146] B. Wattellier *et al.*, "High-power short-pulse laser repetition rate improvement by adaptive wave front correction," Review of scientific instruments **75**, 5186–5192 (2004).

[147] Y. Kato *et al.*, "Random phasing of high-power lasers for uniform target acceleration and plasma-instability suppression," Phys. Rev. Lett. **53**, 1057 (1984).

[148] S. Skupsky *et al.*, "Improved laser-beam uniformity using the angular dispersion of frequency-modulated light," J. Appl. Phys. **66**, 3456–3462 (1989).

[149] A. P. L. Robinson *et al.*, "Radiation pressure acceleration of thin foils with circularly polarized laser pulses," New J. Phys. **10**, 013021 (2008).

[150] J. Mendonça and J. Vieira, "Donut wakefields generated by intense laser pulses with orbital angular momentum," Physics of Plasmas (1994-present) **21**, 033107 (2014).

[151] M. Born and E. Wolf, *Principles of optics: electromagnetic theory of propagation, interference and diffraction of light* (Cambridge university press, 1999), p. 531.

[152] A. E. Siegman, *Lasers* (University Science Books, 1986), pp. 656–662.

[153] C. Brabetz *et al.*, "Laser-driven ion acceleration with hollow laser beams," Physics of Plasmas (1994-present) **22**, 013105 (2015).

[154] F. Salin *et al.*, "Thermal eigenmode amplifiers for diffraction-limited amplification of ultrashort pulses," Opt. Lett. **23**, 718–720 (1998).

[155] V. Bagnoud, "Etude et réalisation d'une chaîne laser femtoseconde kilohertz térawatt. Etude de l'accord de phase spectrale: amplification de puissance en présence de charge thermique," Ph.D. thesis, Université Bordeaux (1999).

[156] M. L. Stock and G. A. Mourou, "Chirped pulse amplification in an erbium-doped fiber oscillator/erbium-doped fiber amplifier system," Opt. Commun. **106**, 249–252 (1994).

[157] M. Fermann, A. Galvanauskas, and D. Harter, "All-fiber source of 100-nJ subpicosecond pulses," Appl. Phys. Lett. **64**, 1315–1317 (1994).

[158] D. C. Brown and H. J. Hoffman, "Thermal, stress, and thermo-optic effects in high average power double-clad silica fiber lasers," IEEE J. Quantum Elect. **37**, 207–217 (2001).

[159] J. C. Knight, "Photonic crystal fibres," Nature **424**, 847–851 (2003).

[160] F. Röser *et al.*, "Millijoule pulse energy high repetition rate femtosecond fiber chirped-pulse amplification system," Opt. Lett. **32**, 3495–3497 (2007).

[161] C. Labaune *et al.*, "On the feasibility of a fiber-based inertial fusion laser driver," Opt. Commun. **281**, 4075–4080 (2008).

[162] T. A. Planchon *et al.*, "Measurement of pump-induced transient lensing in a cryogenically-cooled high average power Ti:sapphire amplifier," Opt. Express **16**, 18557–18564 (2008).

[163] J. Rothhardt *et al.*, "Octave–spanning OPCPA system delivering CEP–stable few–cycle pulses and 22 W of average power at 1 MHz repetition rate," Opt. Express **20**, 10870–10878 (2012).

[164] L. Waxer *et al.*, "High-conversion-efficiency optical parametric chirped-pulse amplification system using spatiotemporally shaped pump pulses," Optics letters **28**, 1245–1247 (2003).

[165] M. Guardalben *et al.*, "Design of a highly stable, high-conversion-efficiency, optical parametric chirped-pulse amplification system with good beam quality," Optics express **11**, 2511–2524 (2003).

[166] V. Bagnoud *et al.*, "A multiterawatt laser using a high-contrast, optical parametric chirped-pulse preamplifier," in "Conference on Lasers and Electro-Optics," (Optical Society of America, 2005), p. JFA1.